The Pennsylvania State University

The Graduate School

DYNAMICS OF FLUIDIC DEVICES

WITH APPLICATIONS TO ROTOR PITCH LINKS

A Dissertation in

Mechanical Engineering

by

Lloyd H. Scarborough, III

Submitted in Partial Fulfillment

of the Requirements

for the Degree of

Doctor of Philosophy

May 2014

The dissertation of Lloyd H. Scarborough, III was reviewed and approved[*]
by the following:

Christopher D. Rahn
Professor of Mechanical Engineering
Dissertation Co-Advisor, Co-Chair of Committee

Edward C. Smith
Professor of Aerospace Engineering
Dissertation Co-Advisor, Co-Chair of Committee

Kevin L. Koudela
Graduate Faculty Member, Engineering Science and Mechanics

Martin W. Trethewey
Professor of Mechanical Engineering

Karen A. Thole
Professor of Mechanical Engineering
Head of the Department of Mechanical and Nuclear Engineering

[*]Signatures are on file in the Graduate School.

Abstract

Coupling a Fluidic Flexible Matrix Composite (F^2MC) to an air-pressurized fluid port produces a fundamentally new class of tunable vibration isolator. This fluidlastic device provides significant vibration reduction at an isolation frequency that can be tuned over a broad frequency range. The material properties and geometry of the F^2MC element, as well as the port inertance, determine the isolation frequency. A unique feature of this device is that the port inertance depends on pressure so the isolation frequency can be adjusted by changing the air pressure. For constant port inertance, the isolation frequency is largely independent of the isolated mass so the device is robust to changes in load. A nonlinear model is developed to predict isolator length and port inertance. The model is linearized and the frequency response calculated. Experiments agree with theory, demonstrating a tunable isolation range from 9 Hz to 36 Hz and transmitted force reductions of up to 60 dB at the isolation frequency.

Replacing rigid pitch links on rotorcraft with coupled fluidic devices has the potential to reduce the aerodynamic blade loads transmitted through the pitch links to the swashplate. Analytical models of two fluidic devices coupled with three different fluidic circuits are derived. These passive fluidlastic systems are tuned, by varying the fluid inertances and capacitances of each fluidic circuit, to reduce the transmitted pitch-link loads. The different circuit designs result in transmitted pitch link loads reduction at up to three main rotor harmonics. The simulation results show loads reduction at the targeted out-of-phase and in-phase harmonics of up to 88% and 93%, respectively. Experimental validation of two of the fluidic circuits demonstrates loads reduction of up to 89% at the out-of-phase isolation frequencies and up to 81% at the in-phase isolation frequencies.

Replacing rigid pitch links on rotorcraft with fluidic pitch links changes the blade torsional impedance. At low frequency, the pitch link must have high impedance to pass through the pilot's collective and cyclic commands to control the aircraft. At higher frequencies, however, the pitch-link impedance can be tuned to change the blade pitching

response to higher harmonic loads. Active blade control to produce higher harmonic pitch motions has been shown to reduce hub loads and increase rotor efficiency. This work investigates whether fluidic pitch links can passively provide these benefits. An analytical model of a fluidic pitch link is derived and incorporated into a rotor aeroelastic simulation for a rotor similar to that of the UH-60. Eighty-one simulations with varied fluidic pitch link parameters demonstrate that their impedance can be tailored to reduce rotor power and all six hub forces and moments. While no impedance was found that simultaneously reduced all components, the results include cases with reductions in the lateral 4/rev hub force of up to 91% and 4/rev hub pitching moment of up to 67%, and main rotor power of up to 5%.

Table of Contents

List of Figures

List of Tables

List of Symbols

a	Fluid track cross-sectional area, m^2
a_i	Transfer function denominator coefficient, $i = 1,\ 2,...$
a_1	Fluid port cross-sectional area, m^2
A	Cross-sectional area of a single fiber or piston area, m^2
A_R	Fluid port wetted area, m^2
b_i	Transfer function numerator coefficient, $i = 1,\ 2,...$
c_d	Elastomer damping, $\text{N} \cdot \text{s/m}$
c_o	Baseline damping, $\text{N} \cdot \text{s/m}$
C_a	Accumulator capacitance, m^3/Pa
C_i	Linearization constant, $i = 1,\ 2,\ 3;\ C_1$ [N/m], C_2 [m^2], C_3 [m^2]
C_p	Pitch-link capacitance, m^3/Pa
C_T	Thrust coefficient
d	Circuit-component inner diameter, m
D	Piston diameter, m
E	Young's modulus, MPa
f_i	Isolation frequency, Hz; or input force from blade, $i = 1,\ 2$, N
f_{t_i}	Transmitted force to hub, $i = 1,\ 2$, N
F	Input force, N
F_t	F^2MC tube transmitted force to ground, N
h	Fluid height, cm
H	Frequency response function
I	Inertance, kg/m^4
I_θ	Blade pitch inertia, $\text{kg} \cdot \text{m}^2$
j	Imaginary unit
k_d	Elastomer stiffness, kN/m
k_o	Baseline stiffness, kN/m
l_{ph}	Pitch-horn length, m
L	Length, m

m	Number of fibers; piston mass, kg; or blade pitch inertia equivalent, kg
m_b	Blade mass (per unit length), kg/m
M	Mass suspended from F^2MC tube, kg
M_θ	Blade-root pitching moment, $N \cdot m$
N_b	Number of blades
p	Pitch-link gage pressure, kPa
p_a	Accumulator gage pressure, kPa
p_{atm}	Atmospheric pressure, kPa
p_m	Tee gage pressure, kPa
p_1	F^2MC tube or Pitch Link 1 gage pressure, kPa
p_2	F^2MC vibration isolator accumulator or Pitch Link 2 gage pressure, kPa
Q	Flow rate, m^3/s
r	Resistance to flow (per unit length), $Pa \cdot s/m^3/m$
R	Blade radius, m
R_f	Total resistance to flow, $Pa \cdot s/m^3$
R_i	F^2MC tube inner radius, m
R_o	F^2MC tube outer radius, m
s	Laplace domain variable, rad/s
t	Diaphragm or wall thickness, m; or time, s
T	Fiber tension, N
u	Strain energy per unit volume, N/m^2
U	Strain energy, $N \cdot m$
V	Material volume or fluid-volume displacement, m^3
V_{tube}	F^2MC tube volume, m^3
W	Work, $N \cdot m$
x	Piston displacement, m
x_{o_i}	Blade-pitch-inertia-equivalent displacement, $i = 1, 2$, m
α	Unstrained fiber wind angle, degrees
β	Instantaneous fiber wind angle, degrees
ε_x	F^2MC tube axial strain
θ	Blade elastic twist, degrees
θ_r	Blade-root elastic twist, degrees
λ	Principal stretch
μ	Advance ratio
ν	Poisson's ratio
ρ	Fluid density, kg/m^3
σ	Solidity
σ_x	F^2MC tube hoop stress
σ_y	F^2MC tube axial stress

σ_z F^{2}MC tube through-thickness stress

ω Angular frequency of excitation, rad/s

ω_z Transfer function zero frequency, rad/s

ψ Azimuth angle, degrees

Ω Rotor frequency, rad/s

$(\ )_{eq}$ Equilibrium value

$(\ )_o$ Unstrained F^{2}MC tube parameter or static value

$(\ )_r$ Variable pertaining to F^{2}MC tube rubber liner

$(\ )_s$ Variable pertaining to F^{2}MC tube fibers

$(\ )_v$ Vertical track parameter

$\dot{(\ )}$ Time derivative

$\bar{(\ )}$ Small-change variable

Acknowledgments

Many people have encouraged and guided me throughout my graduate studies. First thanks go to my advisors, Dr. Christopher Rahn and Dr. Edward Smith, for their technical guidance, faithfulness, and perseverance. I also thank Dr. Jianhua Zhang for his help with the rotor aeroelastic simulation. Fellow students Jonas Corl, Conor Marr, and Amir Lotfi-Gaskarimahalle provided many helpful thoughts and ideas in addition to friendships. Machinists Philip Irwin, Carson Baird, and William Genet aided in the manufacturing of parts for experiments. Secretaries Jennifer Houser, Debbie Mottin, and Diana Lyons eased the bureaucratic burden – thank you!

Thank you to Dr. Lane Miller of LORD Corporation and Dr. Edward Liszka of the Applied Research Laboratory (ARL) at The Pennsylvania State University for their faithful financial support. Both Dr. Mark Jolly at LORD and Dr. Kevin Koudela at ARL gave helpful insights on projects' directions.

To my father and late mother, thank you for the constant care and encouragement. To my brother Clinton and sister-in-law Theresa, thank you for all the food and fellowship. To Oakwood Presbyterian Church, thank you for the spiritual nourishment and many friendships. To Jesus, thank you for everything; glorify Yourself through this work!

Chapter 1

Introduction

Rotating machinery often produces unsatisfactory levels of vibration at one or more frequencies. While a simple elastomer is not always sufficient for isolating these vibrations, fluidlastic technology enables the design of vibration isolators that outperform elastomers. Fluidic vibration isolators are typically optimized for a single frequency, which limits their effectiveness in applications where the excitation consists of either multiple frequencies or a single frequency that changes over time.

The goal of this work is to expand the performance and potential applications of fluidic vibration isolators. Mathematical models are developed, and analysis tools (Maple and Matlab®) are used to determine the frequency responses of the new devices. Benchtop experiments are conducted to verify predictions. A fluidic vibration isolator using a composite tube as the pumping mechanism is presented. The behavior of coupled fluidic devices, and their potential as pitch links on helicopters, is investigated. Replacing the rigid pitch links on helicopters with fluidic pitch links to reduce vibratory hub loads and required rotor power is also analyzed.

1.1 Vibration Isolation

Two main methods exist for passively reducing unwanted vibration in mechanical systems: vibration absorbers and vibration isolators. A vibration absorber uses a secondary system attached to the primary device to reduce vibration. A vibration isolator is a device inserted between the source of vibration and the primary device to reduce vibration transmission [1].

Vibration control devices may be passive, active, or semi-active. Passive vibration isolators and absorbers are pre-configured structural elements that do not require external power [2, 3]. In active vibration control, an actuator applies a force directly to the mechanical system. A microprocessor collects data from sensors located at critical positions throughout the system and sends an appropriate command to the actuator(s) [4]. Semi-active control reduces vibration by tuning system parameters, and thus, it requires less power than active control [5]. Combining passive and active control in a hybrid approach has also been demonstrated [6].

Passive and active vibration control have practical limitations. The nature of passive vibration control devices confines their effectiveness to a band (or bands) of frequencies. If any of the system parameters change or the excitation frequency changes, the driving frequency will no longer match the passive device's tuned frequency. Active vibration control devices can act over a much broader range of frequencies than passive ones, but they often require large amounts of power and can introduce system instabilities [1].

Semi-active vibration control provides some of the benefits of both passive and active vibration control. Semi-active control involves varying the properties of adjustable system elements (such as variable-rate springs, variable-rate dampers, and piezoelectric devices) to minimize transmitted vibrations. The goal of a semi-active approach is to achieve similar performance to active vibration control while consuming signifi-

cantly less power [1]. Fluidic Flexible Matrix Composites (F^2MC) studied by Lotfi-Gaskarimahalle *et al.* [7] are semi-active devices that can change stiffness through the opening and closing of a valve. The work of Hiemenz *et al.* [8] on magnetorheological (MR) dampers and that of Han *et al.* [9] on electrorheological dampers are examples of variable damping devices. Davis and Lesieutre [10], and Clark [11], use piezoelectric devices to achieve semi-active vibration control.

Tuned isolators significantly reduce transmitted vibration over a narrow band of frequencies. An early example of a tuned vibration isolator is the Dynamic Antiresonant Vibration Isolator (DAVI) [12]. This device uses the inertial force from a cantilevered mass to cancel vibration at a target frequency. Halwes' Liquid Inertia Vibration Eliminator (LIVE®) device [13] replaces the cantilevered mass of the DAVI system with liquid that accelerates through a port to produce the canceling inertial force. Smith and Redinger [14] analyze LIVE® vibration isolator technology on Bell's Model 427 helicopter. LORD Corporation's Fluidlastic technology also uses fluid inertance [15].

Researchers have devised various ways of tuning or expanding the narrow frequency range of isolation in fluidlastic devices. Jones and Downing [16] vary the length of the inertia track using a rotatable cylinder. Smith and Stamps [17] use a telescoping port, and Hodgson and Duclos [18] control the length of the port with an electric motor. du Plooy *et al.* [19] modify a LIVE® device to allow adjustable reservoir pressure. Adjusting the air pressure of the fluid reservoir varies the stiffness and isolation frequency of the device. Smith *et al.* [20] integrate smart piezoelectric actuators into a LIVE® device (P-LIVE), increasing its tunability.

The fluidic composite tunable vibration isolator introduced in this document consists of an F^2MC device connected to a fluid reservoir. An F^2MC device consists of a rubber tube, two families of fibers wound at $\pm\alpha$ with respect to the tube's longitudinal axis (See Fig. 1.1.), and a working fluid. Philen *et al.* [21] show that Flexible Matrix

Composite (FMC) tubes can elongate or contract in response to internal pressure. Tubes with fiber angles greater than $54°$ extend due to pressurization, while smaller fiber angles result in contractor tubes (*e.g.*, McKibben actuators) [22, 23, 24]. Liu and Rahn [25] develop a nonlinear static model that predicts this elongation and contraction. Shan *et al.* [26] study the nonlinear-elastic axisymmetric deformation of FMC tubes using large deformation theory. These models [25, 26] account for the end-fitting effects that models with infinitely-long tube assumptions neglect. Philen *et al.* [27] develop a variable stiffness adaptive structure using F^2MC tubes with valve control. They use shell theory to derive the effective elastic modulus of the tube for open (soft) and closed (stiff) valves. Shan *et al.* [28] add the effect of wall compliance by using a 3-D elasticity model of the laminate. By tailoring material properties such as the Young's modulus of the fibers and resin and the fiber angle, one can generate F^2MC structures that outperform currently available variable stiffness materials, including shape memory polymers and lead zirconate titanate (PZT) materials. Lotfi-Gaskarimahalle *et al.* [29] show that F^2MC tubes may serve as tuned vibration absorbers.

Chapter 2 models, designs, and experimentally tests F^2MC tubes as tunable vibration isolators. Based on [29, 30], the model of an F^2MC tube coupled to a pressurized reservoir is derived. The model is linearized to produce a second-order model that predicts the resonance and antiresonance (isolation) frequencies. The theoretical frequency response is compared with experimental testing results.

1.2   Coupled Fluidic Pitch Links

The helicopter pilot's collective and cyclic inputs change the orientation of the swashplate to control the thrust vector of the main rotor. The pitch link provides a stiff connection between the swashplate and the blade root, as shown in Fig. 1.2, to control the pitch
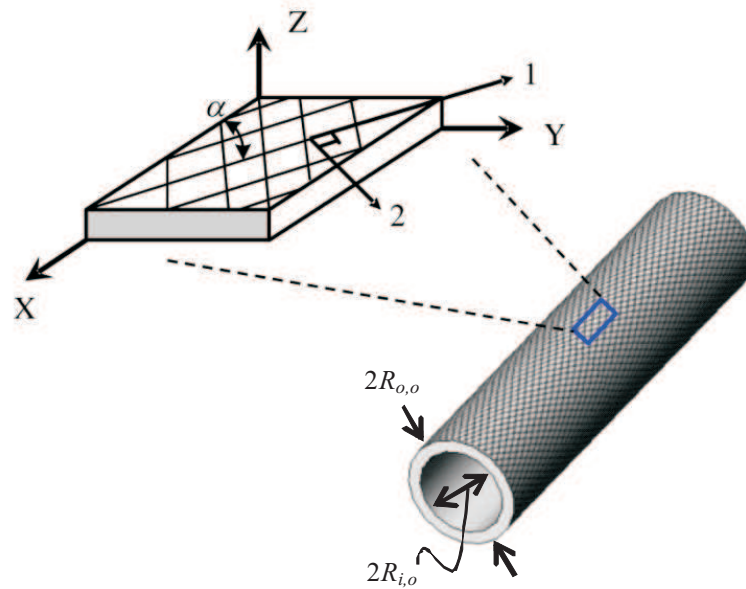
Figure 1.1. Schematic of an F^{2}MC tube, illustrating the two families of fibers wound at $\pm\alpha$ angles with respect to the longitudinal axis.

of the blade about the azimuth. The aerodynamic loads on helicopter rotor blades cause significant unsteady forces that are transmitted through the pitch links to the swashplate. Pitch-link loads increase with rotor power, often limiting the operational flight envelope of helicopters [31, 32], justifying the need for loads reduction in new or retrofitted rotorcraft with larger engines for higher altitude flight, increased aircraft speed, and heavier payloads. Higher harmonic control and a high control system stiffness also increase pitch-link loads [33, 34].

For an ideal rotor operating at a constant rotor speed in steady flight, excitation loads are harmonic and occur at integer multiples of the constant main rotor speed (1/rev, 2/rev, *etc.*). The 1/rev pitch-link load is usually the largest, and the amplitudes of the higher harmonic pitch-link loads generally decrease with increasing harmonic number. The pitch-link loads change with flight condition. For example, in high-speed forward flight, the higher harmonic pitch-link loads can increase significantly [36, 37]. These
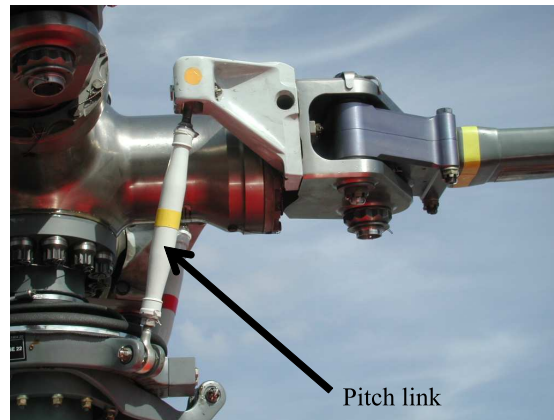
Pitch link

Figure 1.2. Helicopter pitch link [35].

higher harmonic loads fatigue the swashplate and actuators [38], potentially causing premature failure.

Very few researchers have investigated techniques to reduce pitch-link loads by limiting or preventing the aerodynamic conditions leading to high blade pitching moments. Gabel and Tarzanin [39] suggest lowering the torsional natural frequency of the blades to reduce high pitch-link loads resulting from stall flutter. Adams [40] replaces the stiff pitch links of a CH-54B with spring-damper assemblies and demonstrates up to a 50% reduction in stall-induced pitch-link loads in subsequent flight tests. Voskuijl *et al.* [41] implement an H_∞ controller that reduces pitch-link loads by optimizing the collective pitch input to prevent stall.

In applications where tonal, rather than broad-band, excitations are dominant, passive fluidic devices may have potential for vibration and loads control. Fluidic devices modify the stiffness and damping in addition to increasing the *apparent* mass of a system without adding much *actual* mass, through the use of the mass-like property, inertance. Fluid in a section of small tubing can have a high inertance, despite having little actual mass. Fluidic devices also provide more flexible packaging options than a tuned isolator with a cantilevered mass. The fluid track replaces the cantilever and

may be routed as desired. Han *et al.* [42] propose replacing the stiff pitch links on rotorcraft with fluidlastic isolators. The geometry of the tuning port (or fluid track) of the fluidlastic isolator dictates the isolation frequency. These fluidic pitch links can only target a single higher harmonic pitch-link load. Accordingly, Han *et al.* [43] also propose connecting fluidic pitch links such that they share the same fluid track. This coupling of fluidic pitch links improves simultaneous reduction of multiple higher harmonic pitch-link loads in addition to ensuring equal blade torsional responses if the system were to leak. Kurczewski *et al.* [44] model and experimentally verify coupled fluidic pitch links for loads reduction at an odd harmonic of the rotor frequency.

A coupled fluidic pitch link system has the potential to attenuate vibratory loads such that the blade pitch control components (*e.g.* the swashplate and its actuators) can achieve longer fatigue life, increase flight safety, and be designed with reduced mass. The use of load-controlling pitch links may also provide increased maximum forward velocity, payload, and altitude, which are currently limited by high loads due to retreating blade stall. Although coupled fluidic pitch links offer many potential benefits, they also increase the complexity, cost, and weight of the pitch control system. Furthermore, a coupled fluidic pitch link system has more failure modes than traditional stiff pitch links.

Chapter 3 builds on [44] by investigating the loads-reduction capability of coupled fluidic pitch link systems on rotors with an even number of blades through modeling, frequency-domain analysis, and experimental validation. The coupling fluid track of [44] is replaced by three different fluidic circuits. Each circuit consists of the simplest combination of fluid paths and accumulators that reduces the pitch-link loads at the desired harmonics. The fluidic circuit can be designed to simultaneously target out-of-phase and in-phase pitch-link loads. Theoretical predictions are presented for a heli-

copter similar to the UH-60 with coupled fluidic pitch links. Two benchtop experiments validate the theoretical predictions.

1.3   Impedance Tailored Fluidic Pitch Links

Controlling the higher harmonic pitching motion of rotor blades can increase rotor performance and reduce noise and vibration. Higher harmonic pitching motion may be imparted by the swashplate, replacing the pitch links with actuators, or elastically twisting the blade via an outboard flap. Shaw [45] uses the swashplate to superimpose higher harmonics on the collective and cyclic inputs – an approach known as Higher Harmonic Control (HHC). McHugh and Shaw [46] validate the effectiveness of HHC for vibration reduction with a wind-tunnel test. Wood *et al.* [47] demonstrate vibration reduction using HHC in a flight test on a U.S. Army helicopter.

Active, semi-active, and passive pitch-link systems have been developed by previous researchers. In a full-scale wind-tunnel test, Jacklin *et al.* [48] use active Individual Blade Control (IBC) to demonstrate up to a 7% reduction in total power in high-speed forward flight. They also show significant, simultaneous vibration and noise reduction. Yeo *et al.* [49] show the existence of an optimal 2/rev input (amplitude and phase) for maximum power reduction, in a recent full-scale wind-tunnel test. Optimizing only for a reduction in required power, however, can cause higher vibration levels [50]. Anusonti-Inthra and Gandhi [51] reduce vibratory hub loads in forward flight by cyclically varying the flap, lag, and torsion stiffness of the blade root region at harmonics of the rotor rotation speed. They observe that these semi-active changes in the torsion stiffness significantly increase the pitch-link loads. Nitzsche *et al.* [52] implement a semi-active axial switching control device to reduce vibrations transmitted to the hub.

Milgram *et al.* [53] replace the rigid pitch link with a spring/damper element to passively reduce vibratory hub loads.

Millott and Friedmann [54] achieve vibration reduction similar to conventional IBC using an active trailing edge flap (TEF). The TEF requires a fraction of the power needed for conventional IBC. Zhang *et al.* [55] show that the trailing edge flap control effort may be reduced by a hybrid optimization of both blade structure and flap controller design. Recently, Bae and Gandhi [56] predict increases in rotor performance at high speeds and/or gross weights by using spanwise-segmented aerodynamic effectors.

In applications where tonal, rather than broad-band, excitations are dominant, passive fluidic devices may have potential for vibration and loads control. Passive solutions are relatively low cost and simple because they do not require power/control signals in the rotating frame and use materials and components that have already flown on countless rotorcraft. Han *et al.* [42] propose replacing the rigid pitch links on rotorcraft with fluidlastic isolators to reduce pitch-link loads.

Although fluidic pitch links offer potential benefits, they also increase the complexity, cost, and weight of the pitch control system. Furthermore, a fluidic pitch link system has more failure modes than traditional stiff pitch links. If the fluidic pitch links are coupled in a ring, similar to the coupling of spring-damper assemblies in [40], all of the pitch links lose fluid if one develops a leak. This fluidic coupling ensures that the pitch responses of the blades are identical.

By tailoring the impedance of a fluidic pitch link, the pitching motion of the blade, θ, in response to the natural aerodynamic loads, M_θ, may approach the pitch trajectory achieved with the active control approaches outlined above. The impedance of a mechanical system relates an applied force to the resulting velocity of the system. Jolly and Margolis [57] present a framework for describing a mechanical system in terms of

an impedance matrix. If the eigenvalues of the impedance matrix are positive, then the impedance can be realized by a passive mechanical system.

In Chapter 4, the objectives are to reduce vibratory hub loads and improve rotor performance for a given flight condition by replacing the rigid pitch links with tuned passive fluidic pitch links. The fluidic pitch link parameters determine the amplitude and phase of the pitch response of the blade. We model a fluidic pitch link and modify the rotor aeroelastic simulation used in [58] to observe how fluidic pitch links affect the vibratory hub loads and rotor performance. The rotor aeroelastic simulation [58] includes rotor blade flexibility, but is not as complex as Computational Fluid Dynamics/Computational Structural Dynamics (CFD/CSD) [59] analyses. Theoretical predictions are presented for a helicopter rotor similar to the UH-60 with fluidic pitch links.

1.4   Contributions

Coupling a Fluidic Flexible Matrix Composite (F^2MC) to an air-pressurized fluid port produces a fundamentally new class of tunable vibration isolator. This fluidlastic device provides significant vibration reduction at an isolation frequency that can be tuned over a broad frequency range. A unique feature of this device is that the port inertance depends on pressure so the isolation frequency can be adjusted by changing the air pressure. Experiments agree with theory, demonstrating a tunable isolation range from 9 Hz to 36 Hz and transmitted force reductions of up to 60 dB at the isolation frequency.

Replacing rigid pitch links on rotorcraft with coupled fluidic devices has the potential to reduce the aerodynamic blade loads transmitted through the pitch links. Analytical models of two fluidic devices coupled with three different fluidic circuits are derived. The simulation results show loads reduction at the targeted out-of-phase and in-phase

harmonics of up to 88% and 93%, respectively. Two benchtop experiments validate the theoretical predictions.

Replacing rigid pitch links on rotorcraft with fluidic pitch links also changes the blade torsional impedance. An in-house rotor aeroelastic simulation is modified to include a fluidic pitch link model and is then used to conduct a parametric study. The parametric study results include cases with reductions in the lateral 4/rev hub force of up to 91% and 4/rev hub pitching moment of up to 67%, and reductions in main rotor power of up to 5%.

Chapter 2

Fluidic Composite Tunable Vibration Isolators

2.1 F^2MC Static Modeling

Figure 2.1 shows a schematic diagram of a fluidic composite tunable isolator. A mass M is attached to one end of a fluid-filled F^2MC tube. The mass is excited by a disturbance force $F(t)$ and responds with displacement $x(t)$. The F^2MC tube is connected to a fluid port and then a pressurized accumulator. As the mass vibrates, the volume of the F^2MC tube changes, and fluid pressure $p_1(t)$ is developed inside the tube. This forces fluid through the fluid port at a flow rate $Q(t)$. The objective of the isolator is to reduce the transmitted force $F_t(t)$ to the base.

The fluidic composite tunable vibration isolator is analogous to the DAVI device as shown in Fig. 2.1. The inertance of the fluid in the fluid port corresponds to m_f, and the ratio of the F^2MC tube diameter to the fluid port diameter corresponds to the ratio of b to a. The axial stiffness of the F^2MC tube corresponds to K, and the fluid port's resistance to flow appears as C in the DAVI analogy. The system model is developed

in two parts. First, the nonlinear relationship between the inputs (applied load $F(t)$ and pressure $p_1(t)$) and the output F²MC displacement $x(t)$ is developed from a static analysis. This relationship is then linearized and incorporated into a dynamic model that predicts the force transmissibility frequency response.
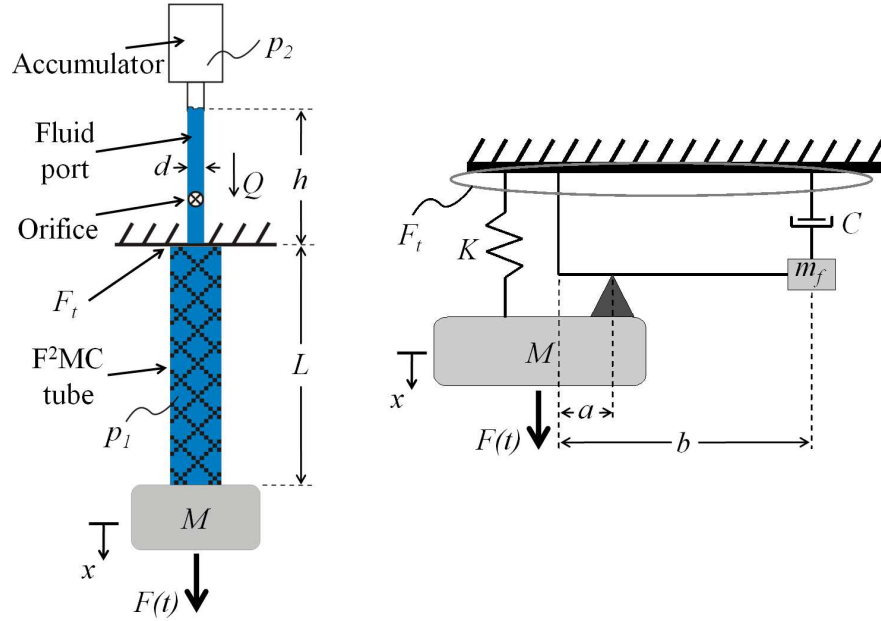
Figure 2.1. Schematic (left) and mechanical equivalent (right) of the fluidic composite isolator.

The static model assumes that the rubber is incompressible and that the fibers are inextensible relative to the extension of the entire tube. It also neglects any effects caused by clamping the F²MC tube to fittings at either end.

The model equations are derived using the principle of virtual work,

$$\delta U = \delta W, \tag{2.1}$$

where U is the total strain energy and W is the work done by external forces.

2.1.1 Strain Energy

The strain energy stored in the F^{2}MC tube

$$U = U_r + U_s, \tag{2.2}$$

where U_r and U_s are the strain energy stored in the rubber tube and the fibers, respectively.

The strain energy of the rubber tube is given by

$$U_r = u_r V_r, \tag{2.3}$$

where u_r and V_r are the strain energy per unit volume and volume of the rubber tube, respectively. From Gaussian network theory [60],

$$u_r = \frac{E_r}{6}(\lambda_1^2 + \lambda_2^2 + \lambda_3^2 - 3), \tag{2.4}$$

where E_r is the Young's modulus of the rubber, λ_1 to λ_3 are the principal stretches,

$$\lambda_1 = \frac{L}{L_o}, \tag{2.5}$$

and incompressibility of the rubber implies

$$\lambda_3 = \frac{1}{\lambda_1 \lambda_2}. \tag{2.6}$$

The instantaneous length and unstrained length of the F^{2}MC tube are L and L_o, respectively. The unstrained length is measured at zero internal pressure and axial load. For inextensible fibers [25],

$$\lambda_1^2 \cos^2 \alpha + \lambda_2^2 \sin^2 \alpha = 1. \tag{2.7}$$

Substitution of Eqs. (2.4), (2.6), and (2.7) into Eq. (2.3) produces the strain energy of the rubber tube as a function of λ_1.

The strain energy stored in the fibers

$$U_s = \frac{mT^2 L_s}{2E_s A_s},$$ (2.8)

where m is the number of fibers, T is the tension in the fibers, and L_s, E_s, and A_s are the length, Young's modulus, and cross-sectional area of the fibers, respectively. Hooke's Law in the x direction,

$$\varepsilon_x = \frac{1}{E_r}[\sigma_x - v(\sigma_y + \sigma_z)],$$ (2.9)

forms the basis for determining the tension in the fibers, where σ_x, σ_y, and σ_z are the Cartesian components of the stress, v is the Poisson's ratio of the rubber, and the strain in the x direction

$$\varepsilon_x = \lambda_1 - 1.$$ (2.10)

Force balances in the hoop and longitudinal directions of the F^{2}MC tube lead to

$$\sigma_x = \frac{\pi p_1 R_i^2 + F - mT \cos\beta}{\pi(R_o^2 - R_i^2)}$$ (2.11)

and

$$\sigma_y = \frac{1}{t}\left[p_1 R_i - \frac{mT \tan\alpha \sin\beta}{2\pi\lambda_1 R_{o,o}}\right],$$ (2.12)

where t, R_i, and R_o are the wall thickness, inner radius, and outer radius of the rubber tube, respectively. The initial, unstrained tube outer diameter is $R_{o,o}$. The wind angle of the fibers, β, is related to the unstrained wind angle, α, by

$$\cos\beta = \lambda_1 \cos\alpha$$ (2.13)

using the inextensibility assumption [25]. Substituting Eqs. (2.10)-(2.12) into Eq. (2.9), neglecting the through-thickness stress, and solving for the tension yields

$$T = \frac{E_r(\lambda_1 - 1) + \frac{\nu p_1 R_i}{t} - \frac{\pi p_1 R_i^2 + F}{\pi(R_o^2 - R_i^2)}}{\frac{m}{\pi}\left[\frac{\nu \tan \alpha \sin \beta}{2t\lambda_1 R_{o,o}} - \frac{\cos \beta}{R_o^2 - R_i^2}\right]}. \tag{2.14}$$

From the incompressible rubber assumption,

$$t = \frac{R_{o,o}^2 - R_{i,o}^2}{\lambda_1(R_o + R_i)}, \tag{2.15}$$

or,

$$t = \frac{R_{o,o} - R_{i,o}}{\lambda_1 \lambda_2}, \tag{2.16}$$

where $R_{i,o}$ is the unstrained inner radius of the tube. Finally, the inner and outer radii of the rubber tube may be written as

$$R_i = \frac{1}{2}\left[\lambda_2(R_{i,o} + R_{o,o}) - t\right], \tag{2.17}$$

and

$$R_o = R_i + t. \tag{2.18}$$

Substituting Eq. (2.7) and Eqs. (2.13)-(2.18) into Eq. (2.8) produces the fiber strain energy as a function of λ_1.

2.1.2 Work

The work done on the F^{2}MC tube

$$W = W_{p_1} + W_F, \tag{2.19}$$

where W_{p_1} and W_F are the work done by the applied pressure and axial load, respectively. The work done by the applied pressure

$$W_{p_1} = p_1(V_{tube} - V_{tube,o}), \tag{2.20}$$

where $V_{tube,o}$ is the unstrained volume of the F^{2}MC tube and

$$V_{tube} = \pi R_i^2 \lambda_1 L_o. \tag{2.21}$$

The work done by the axial load

$$W_F = F(\lambda_1 - 1)L_o. \tag{2.22}$$

Substitution of Eqs. (2.7), (2.16)-(2.18), and (2.21) into Eqs. (2.20) and (2.22) produces the work as a function of λ_1.

Finally, substituting the expressions for strain energy and work into Eq. (2.1) results in an expression that can be solved numerically for λ_1 for a given pressure and axial load.

2.2   Static Model Validation

The static model is validated by varying both the pressure and axial load of an F^{2}MC tube and measuring its length. Table 2.1 shows the model parameters used for the experimental setup. Figure 2.2 shows good agreement between model predictions (lines) and experimental measurements (symbols). Four pressures are shown with static loads varying from 0 to 160 N. As the pressure increases, the tube shortens due to its initial wind angle of 18.5°, which is less than 54°, causing the tube to contract under pressurization. Relative to 210 kPa pressurization (solid line), the tube pressurized to 410 kPa (dash-dotted line) is more than 1 cm shorter. Axial loads, on the other hand, increase

Table 2.1. Experimental parameter values.

	Description	Parameter	Value
	Unstrained fiber angle	α	18.5°
	Cross-sectional area of single fiber	A_s	3.1e-8 m^2
	Young's modulus of rubber	E_r	1.03 MPa
	Young's modulus of fibers	E_s	2.96e3 MPa
F^{2}MC	Unstrained tube length	L_o	0.138 m
	Number of fibers	m	80 strands
	Unstrained inner radius of tube	$R_{i,o}$	0.0038 m
	Unstrained outer radius of tube	$R_{o,o}$	0.0056 m
	Poisson's ratio of rubber	ν	0.5
Fluid Circuit Components	Diameter of fluid port	d	0.0097 m
	Density of fluid	ρ	993 $\frac{\text{kg}}{\text{m}^3}$
	Flow resistance	R_f	4.2e6 $\frac{\text{Pa·s}}{\text{m}^3}$

the length of the tube. Adding weight of 160 N increases the length by over 2 cm, bringing the tube under 210 kPa pressurization almost back to its original length. For each pressurization, five length measurements are shown for different axial loads. The experimental data matches very closely with the theoretical predictions.

The static model also predicts the fluid (in this case, water) height, h, for a given fluid port diameter, d. Figure 2.3 shows that the experimentally predicted height of water in the tube (line) matches the experimental measurements (circles) for an applied load of 116 N. The curve is not smooth due to changes in the port diameter due to fittings.
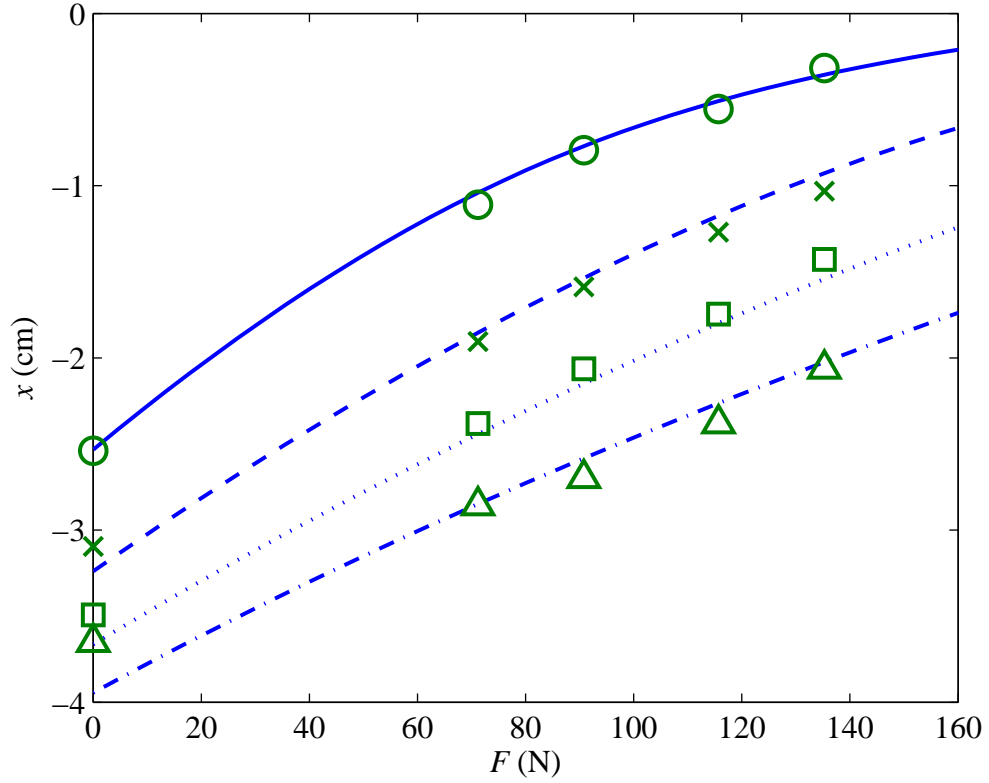
Figure 2.2. Theoretical and experimental change in tube length versus static load at four pressures: 210 kPa (solid line and O), 280 kPa (dashed line and X), 340 kPa (dotted line and □), and 410 kPa (dash-dotted line and △).

2.3 F²MC Isolator Dynamic Modeling

To predict the dynamic behavior of the F²MC-fluidic circuit system, the static model is linearized about an operating point. Summing the forces on the mass, M, yields

$$M\ddot{\bar{x}} + C_1\bar{x} + C_2\bar{p}_1 = \bar{F}(t). \tag{2.23}$$

Here, C_1 and C_2 are constants resulting from the linearization of F²MC tube force and an overbar denotes small-change variables. For an incompressible fluid and linear damping,
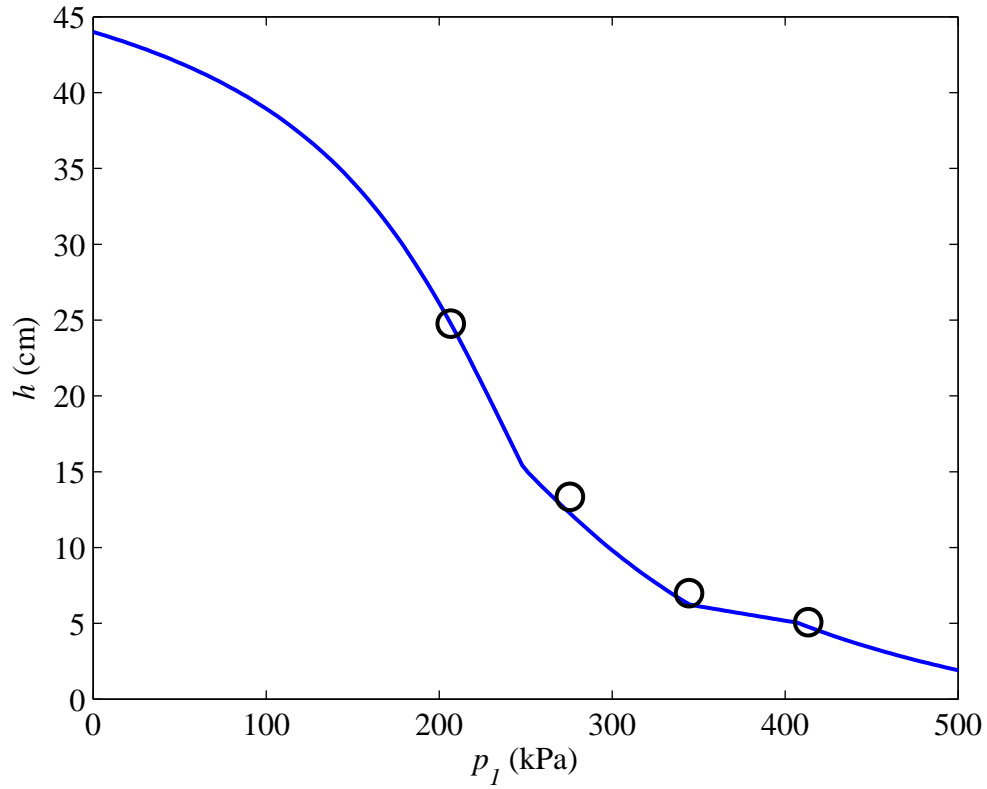
Figure 2.3. Theoretical and experimental port fluid level versus pressure ($F = 116$ N).

the governing equation for flow in the fluid port is

$$\bar{p}_2 - \bar{p}_1 = I\dot{\bar{Q}} + R_f\bar{Q}, \tag{2.24}$$

where R_f is the flow resistance. The dynamics of the accumulator are

$$\dot{\bar{p}}_2 = -\frac{1}{C_a}\bar{Q}, \tag{2.25}$$

where C_a, the capacitance of the accumulator, is the volume of the accumulator divided by the absolute pressure of the accumulator. The fluid inertance

$$I = \frac{\rho h}{a_1}, \tag{2.26}$$

where ρ and a_1 are fluid density and cross-sectional area of the fluid port, respectively. Additionally, the flow, Q, is related to the volume of the F^{2}MC tube by

$$Q = \frac{dV_{tube}}{dt}. \tag{2.27}$$

Finally, the change in the F^{2}MC tube volume may be linearized such that

$$\bar{V}_{tube} = -C_3\bar{x}, \tag{2.28}$$

where C_3 is the linearization constant. Combining Eqs. (2.27) and (2.28) gives

$$\bar{Q} = -C_3\dot{\bar{x}}. \tag{2.29}$$

Summing the forces at the supported end of the F^{2}MC tube yields the force transmitted to the base.

$$\bar{F}_t = C_1\bar{x} + (C_2 - a_1)\bar{p}_1 - R_f A_R \bar{Q}, \tag{2.30}$$

where $A_R = \pi dh$ is the wetted area of the fluid port. Substituting Eqs. (2.23)-(2.26) and (2.29) into Eq. (2.30) and taking the Laplace transform of the resulting expression yields the isolator transfer function from input force to transmitted force,

$$\frac{\bar{F}_t(s)}{\bar{F}(s)} = H = \frac{(C_2 - a_1)Is^2 + (A_R + C_2 - a_1)R_f s + (C_2 - a_1)\frac{1}{C_a} + \frac{C_1}{C_3}}{\left[\frac{M}{C_3} + C_2I\right]s^2 + C_2R_f s + \frac{C_2}{C_a} + \frac{C_1}{C_3}}. \tag{2.31}$$

The transfer function (2.31) has two complex poles and two complex zeros. The poles correspond to the primary mass resonance. The zeros provide the desired antiresonance and isolation. This isolation frequency is not explicitly dependent on the primary mass.

2.4 Dynamic Model Validation

The experimental setup illustrated in Fig. 2.4 is used to validate the dynamic model and demonstrate vibration isolation. The F^{2}MC tube suspends the mass platform from the frame. The upper end of the tube is connected to the fluid port. The F^{2}MC tube consists of a rubber tube and polyethylene terephthalate (PET) fibers. A Ling LMT-100 shaker excites the system. Force transducers from PCB Piezotronics, Inc. measure the input and transmitted forces (Models 208C02 and 208C01, respectively). A National Instruments' LabVIEW system generates a chirp signal for the shaker input and calculates the frequency response function based on the resulting force transducer signals.
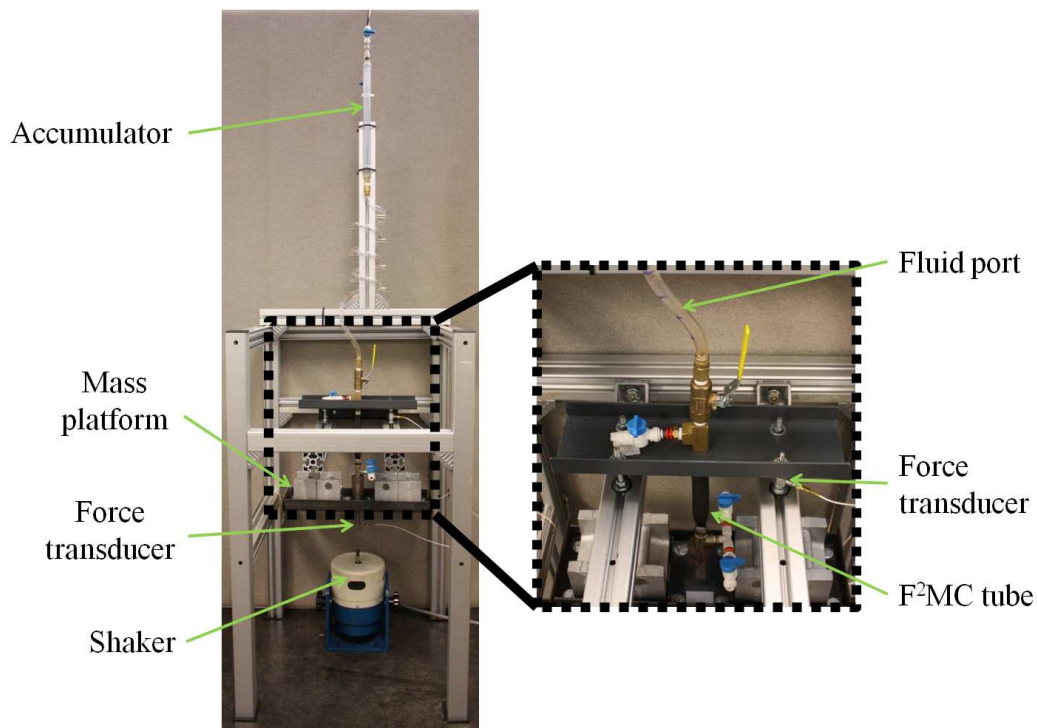
Figure 2.4. Experimental setup.

Figure 2.5 shows the experimentally measured and theoretically predicted frequency responses of the force transmission transfer function at four different system pressures.

(See Appendix A for the Matlab® code.) The resonant peaks and isolation valleys are clearly visible in the responses. The theory and experiment match closely, indicating the fidelity of the system model and validity of the underlying assumptions. The theory overpredicts the amplitude of the first peak because the model neglects the material damping in the F^{2}MC tube. A second, higher frequency peak in the experimental frequency responses is not predicted by the model. This peak may be due to the unmodeled compliance of the F^{2}MC tube, but it is more likely due to the unmodeled motion of the flexible fluid port. As the fluid height (and thus, mass) in the port decreases, the associated peak shifts to a higher frequency.
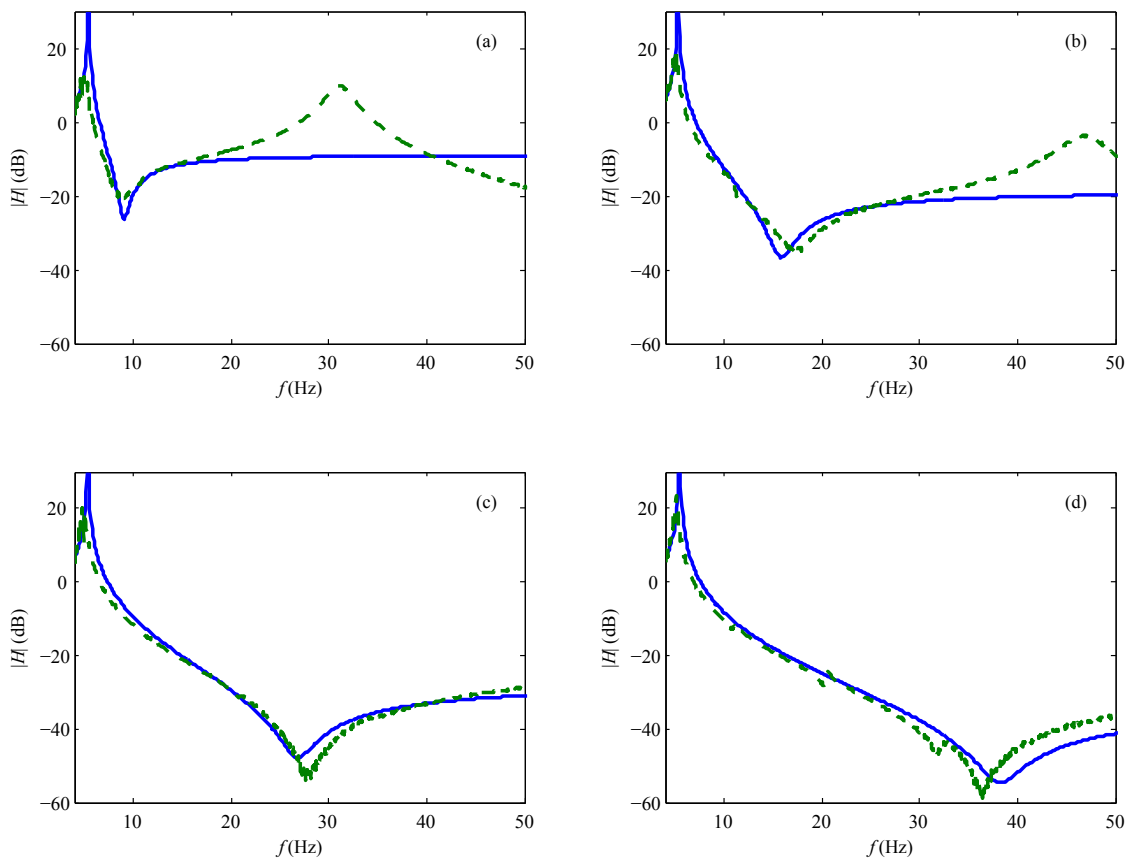
Figure 2.5. Theoretical (solid lines) and experimental (dashed lines) frequency responses for a constant system fluid volume of 30 cm^3 and static load of 116 N at four equilibrium pressures: (a) 210 kPa, (b) 280 kPa, (c) 340 kPa, and (d) 410 kPa.

Figure 2.5 also shows that the isolation frequency f_i can be tuned by changing the applied pressure in the accumulator. Increasing the accumulator pressure causes the F^2MC tube volume to increase, lowering the fluid in the port and the associated inertance. Thus, f_i increases with increasing pressure. The responses in Fig. 2.5 show an isolation range that is tunable from 9 Hz to 36 Hz. The isolator is 90% efficient at 210 kPa (reducing the transmitted force by 20 dB) and 99.9% efficient at 410 kPa (reducing the transmitted force by 60 dB) when the driving frequency matches the isolation frequency. Optimal force transmission reduction requires low fluid damping. Thus, the fluid port should not have constrictions or an exceedingly small diameter, and the fluid should be as inviscid as possible.

Figure 2.6 plots the theoretically predicted relationship between applied pressure and isolation frequency and the four experimental data points from Fig. 2.5. Figure 2.7 shows the isolation frequency as a function of fluid level at four different system pressures. In these curves, the system pressure is maintained constant while the fluid height is varied. The higher the fluid height, the higher the inertance, and the lower the isolation frequency. The four experimental data points from Fig. 2.5 lie close to the theoretically predicted curves. In practice, the volume of fluid would be constant during operation but the pressure could be changed. Thus, the fluid height is a system design parameter while the applied pressure is a tuning parameter that could be varied during operation to minimize the transmitted load.

Figure 2.8 shows that the isolator is relatively independent of the isolated mass, M, if the system pressure is adjusted such that h remains constant. The responses are not identical because the stiffness of the F^2MC tube depends on the wind angle which changes with system pressure and axial load.
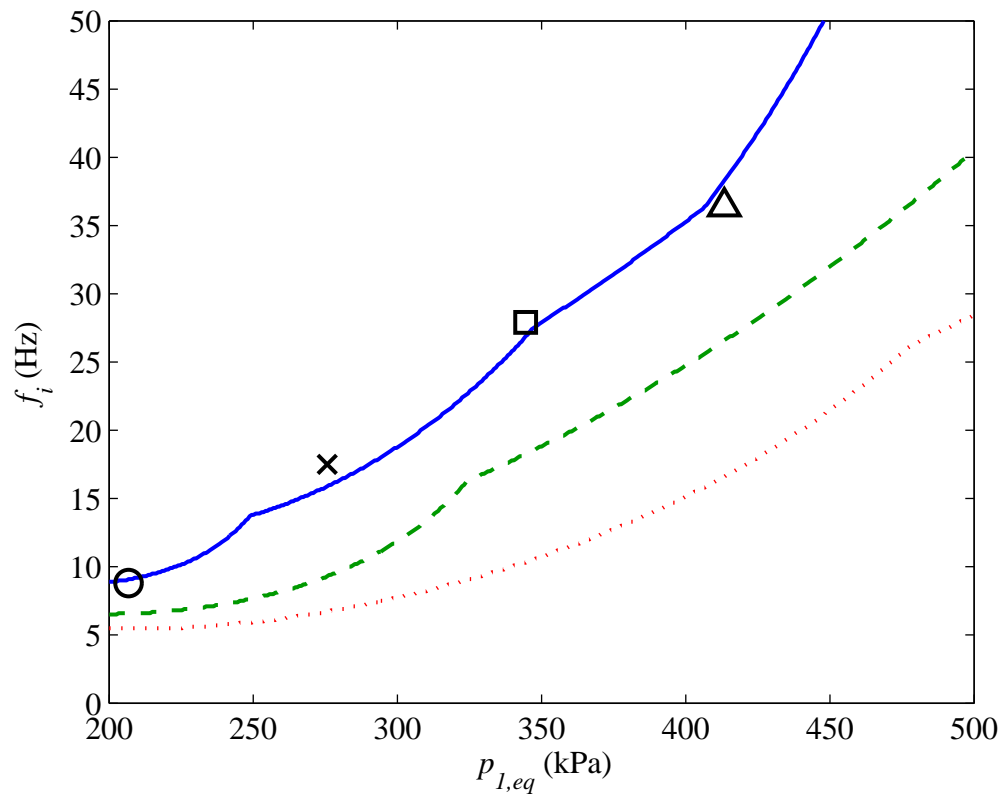
Figure 2.6. Theoretical and experimental isolation frequency versus equilibrium pressure for three fluid volumes and 116 N static load: 30 cm^3 (solid line and symbols), 36 cm^3 (dashed line), and 42 cm^3 (dotted line).
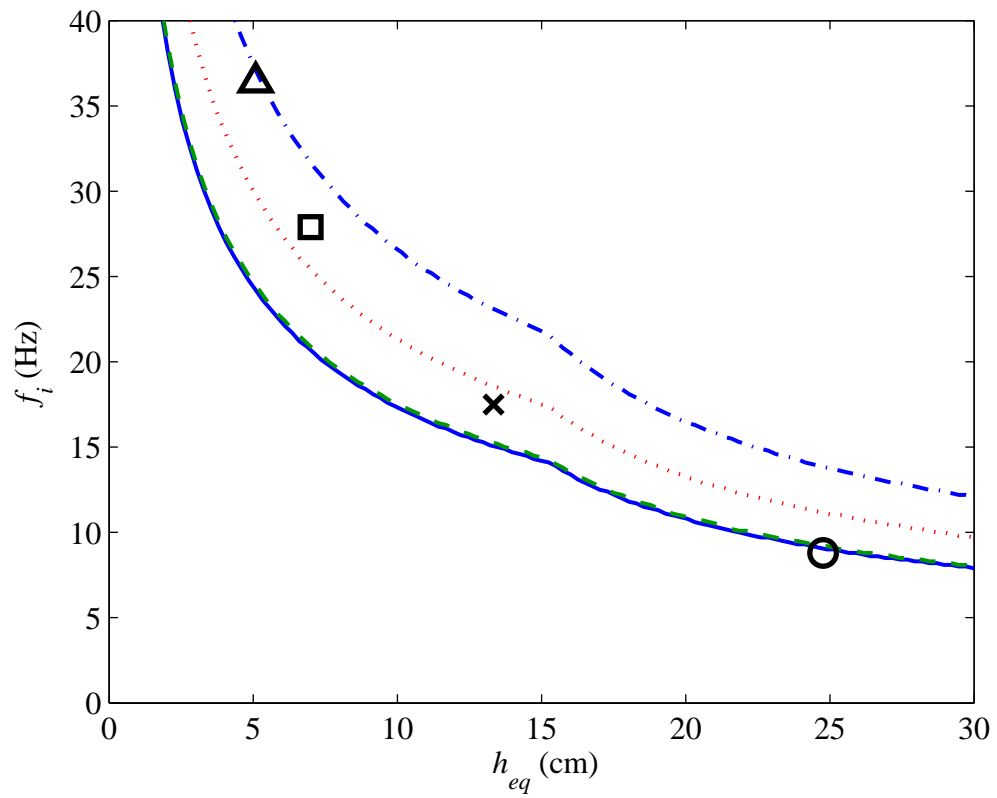
Figure 2.7. Theoretical and experimental isolation frequency versus equilibrium port fluid level at four equilibrium pressures and 116 N static load: 210 kPa (solid line and O), 280 kPa (dashed line and X), 340 kPa (dotted line and □), and 410 kPa (dash-dotted line and △).
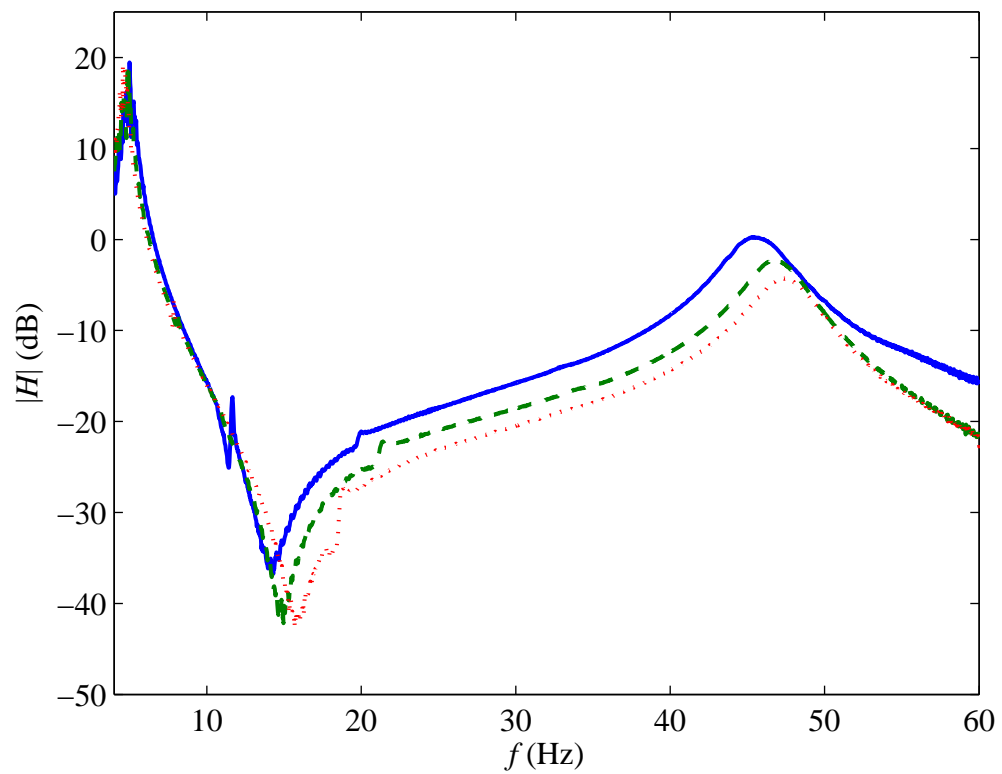
Figure 2.8. Experimental demonstration of the insensitivity of the isolation frequency to static load for constant inertance (h_{eq} = 13 cm): F_{eq} = 96 N and $p_{1,eq}$ = 250 kPa (solid line), F_{eq} = 116 N and $p_{1,eq}$ = 280 kPa (dashed line), and F_{eq} = 136 N and $p_{1,eq}$ = 300 kPa (dotted line).

Coupled Pitch Links for Multi-Harmonic Isolation Using Fluidic Circuits

3.1 Analytical Model

In this chapter, we study two pitch links on opposite sides of the helicopter rotor that are coupled by a fluidic circuit, as shown in Fig. 3.1. The model applies to rotors with an even number of blades. Furthermore, the purpose of the model is to demonstrate how a circuit coupling two fluidic pitch links may be tailored to simultaneously reduce multiple harmonic pitch-link loads. The model does not include several practical considerations that should be included in an expanded analysis prior to installation. These practical considerations include centrifugal-force effects, support and mounting of the fluidic

circuit to withstand the vibratory environment, and changes in the behavior of the system with altitude and orientation.

The blade pitch inertia, I_θ, is represented by an equivalent mass, m. For a given distance between the pitch link and the blade pitch axis, l_{ph},

$$m = \frac{I_\theta}{l_{ph}^2}. \tag{3.1}$$

The loading on each blade is

$$f(t) = f_o + f_{1c}\cos\left(\Omega t\right) + f_{1s}\sin\left(\Omega t\right) + f_{2c}\cos\left(2\Omega t\right) + f_{2s}\sin\left(2\Omega t\right)$$
$$+ f_{3c}\cos\left(3\Omega t\right) + f_{3s}\sin\left(3\Omega t\right) + \cdots. \tag{3.2}$$

Identical blades in steady-state flight results in harmonic blade loading that causes the two pitch links to see the same magnitude and in-phase forcing for even harmonics and 180-degree out-of-phase forcing for odd harmonics. Three different fluidic circuits are studied to demonstrate the correlation between circuit configuration and loads reduction at odd and even harmonics. Each of the three circuits is the simplest configuration that results in loads reduction for the desired combination of odd and even harmonics.

3.1.1 Fluidic Circuit I

The first fluidic circuit (See Fig. 3.1.) has two pitch links that are coupled by a horizontal fluid-filled tube of diameter d and length $2L$, which gives loads reduction at an odd harmonic [44]. The fluid in the horizontal tube has density ρ and lumped inertance $2I$, where

$$I = \frac{4\rho L}{\pi d^2}. \tag{3.3}$$

We assume the resistance to fluid flow in the horizontal tube, $2R_f$, is constant and that the fluid is incompressible. Unlike the fluidic circuit in [44], however, a vertical tube of
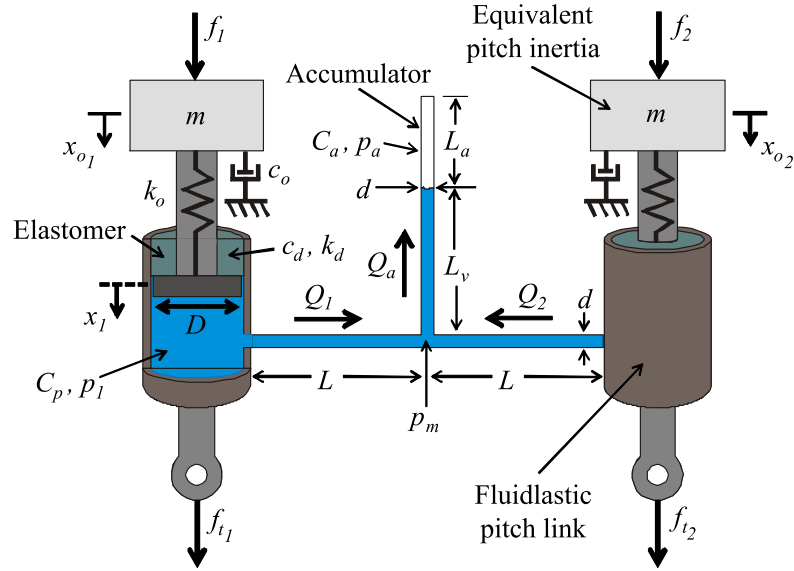
Figure 3.1. Schematic of Fluidic Circuit I.

diameter d rises from a tee at the center of the horizontal tube. The fluid in the vertical

tube has lumped inertance I_v and resistance R_v. An air-over-fluid accumulator at the top

of the tube has length L_a and capacitance C_a and permits fluid flow for in-phase forcing,

allowing for loads reduction at an even harmonic in addition to the aforementioned odd

harmonic. We assume that the pressure and volume fluctuations of the accumulator

during operation are relatively small, so the accumulator capacitance is approximately

constant. From [61], the capacitance of the accumulator is the ratio of the volume of the

accumulator to the absolute pressure of the accumulator; *i.e.*,

$$C_a = \frac{\pi d^2 L_a}{4\left(p_{a_o} + p_{atm}\right)}, \tag{3.4}$$

where p_{a_o} and p_{atm} are the system pre-pressure and the atmospheric pressure, respec-

tively. The system is pre-pressurized to prevent cavitation. Each pitch link has ca-

pacitance C_p and a piston of diameter D that is sealed and elastically restrained by an elastomer with damping c_d and stiffness k_d. The mass, connected to the piston with a spring of stiffness k_o and to the ground by a damper with damping value c_o, moves with displacement $x_o(t)$ in response to $f(t)$. The mass models the blade pitch inertia and the stiffness models the control system stiffness and blade torsion stiffness. The blade loading and aerodynamic damping are modeled by the forcing and damping, respectively. To obtain a linear model, we assume the damping, c_o, is constant. $x_o(t)$ is assumed to be proportional to the pitch motion of the blade root. The piston moves with displacement $x(t)$ and the pressure, $p(t)$, generated in the pitch link induces in-compressible fluid flow $Q(t)$. In-phase forcing induces fluid flow $Q_a(t)$ in the vertical tube. A summary of assumptions is as follows: rigid swashplate, small blade-root pitch angles, negligible joint friction, harmonic pitch-link loads, lumped parameters model the fluid, inviscid fluid flow inside the pitch link, incompressible fluid, constant flow resistance and damping, and constant accumulator capacitance over the range of operating pressures and volume changes.

Summing the forces on each mass gives

$$m\ddot{x}_{o_i} + c_o\dot{x}_{o_i} + k_o x_{o_i} - k_o x_i = f_i(t), \quad i = 1,\ 2, \tag{3.5}$$

where all parameters and variables are defined in the list of symbols. Summing the forces on each piston yields

$$c_d\dot{x}_i + (k_d + k_o)x_i - k_o x_{o_i} = -Ap_i, \quad i = 1,\ 2, \tag{3.6}$$

where $A = \frac{\pi}{4}D^2$. The mechanical-fluidic coupling equation is

$$Q_i = A\dot{x}_i - C_p\dot{p}_i, \quad i = 1, 2. \tag{3.7}$$

The equation for the fluid flow through each half of the horizontal tube is

$$p_i - p_m = I\dot{Q}_i + R_f Q_i, \quad i = 1, 2. \tag{3.8}$$

Similarly, for the fluid flow through the vertical tubing

$$p_m - p_a = I_v\dot{Q}_a + R_v Q_a. \tag{3.9}$$

Fluid flow into and out of the accumulator dictates the change in accumulator pressure

$$\dot{p}_a = \frac{1}{C_a}Q_a. \tag{3.10}$$

Conservation of flow at the tee gives

$$Q_1 + Q_2 = Q_a. \tag{3.11}$$

The transmitted force for each pitch link is

$$f_{t_i} = c_d\dot{x}_i + k_d x_i + Ap_i, \quad i = 1, 2. \tag{3.12}$$

For out-of-phase (OP) forcing, $f_2 = -f_1$. Pitch-link capacitance is due to compliance in the pitch-link housing and is negligible. To simplify the complexity of the following transfer functions, we also neglect the elastomer damping, which is small relative to the aerodynamic and fluid damping. Taking the Laplace transform of Eqs. (3.5)-

(3.12), the resulting system of thirteen equations is solved symbolically for X_{o_i}, X_i, P_i, Q_i, P_m, Q_a, P_a, and F_{t_i} ($i = 1,\ 2$). The transfer function from the input force to the transmitted force is

$$H(s) = \frac{F_{t_1}(s)}{F_1(s)} = \frac{F_{t_2}(s)}{F_2(s)} = \frac{b_1 s^2 + b_2 s + b_3}{a_1 s^4 + a_2 s^3 + a_3 s^2 + a_4 s + a_5},$$ (3.13)

where the coefficients, a_i and b_i, are as defined in Appendix B. Neglecting damping, letting $s = j\omega$, and solving for the zero of the transfer function gives

$$\omega_{z_{OP}} = \sqrt{\frac{k_d}{A^2 I}}.$$ (3.14)

Following a similar procedure for in-phase (IP) forcing, $f_2 = f_1$, yields a transfer function of the same form as Eq. (3.13). (See Appendix B for the coefficients.) The corresponding zero is

$$\omega_{z_{IP}} = \sqrt{\frac{2A^2 + C_a k_d}{A^2 C_a (I + 2I_v)}}.$$ (3.15)

As will be shown, out-of-phase and in-phase excitation forces at the corresponding zero frequencies above can be significantly attenuated, thus relieving some of the strain on the swashplate and its actuators.

A design procedure to reduce transmitted forces at one out-of-phase harmonic and one in-phase harmonic may be deduced from Eqs. (3.14) and (3.15). First, select an elastomer stiffness that provides sufficient 1/rev load transmission and an acceptable torsional natural frequency. Second, choose the proper combination of piston area and horizontal tube inertance to tune the zero of the out-of-phase forcing transfer function

to the desired odd harmonic of the rotor frequency. The diameter of the swashplate determines the minimum fluid track length. Selecting a fluid track diameter and fluid allows one to calculate the horizontal tube inertance. The required piston area may now be calculated from Eq. (3.14). If the calculated piston area is too large, the fluid track length may be increased, or the fluid track diameter may be reduced. The fluid track diameter must not be too small, however, or the flow resistance will be too large. Finally, choose the inertance of the vertical tube and the capacitance of the accumulator to tune the zero of the in-phase forcing transfer function to the desired even harmonic.

Simulations using m, k_o, and Ω values representative of the equivalent blade pitch inertia, effective torsional stiffness, and main rotor rotational frequency of a UH-60, respectively, demonstrate the effectiveness of this design procedure. Table 3.1 lists the parameters used in the simulations. The piston diameter is 5 cm, the fluid track diameter is 0.7 cm, and the horizontal fluid track length is 146 cm. The lengths of the vertical fluid track and accumulator are 13 cm and 4 cm, respectively. Figure 3.2 shows the frequency response $|H(j\omega)|$ from Eq. (3.13) for out-of-phase (top) and in-phase (bottom) forcing. The out-of-phase frequency response is used to assess the out-of-phase frequencies, which are highlighted by the gray bars. The in-phase transfer function is used to assess the in-phase frequencies (again, highlighted by the gray bars). The device in Fig. 3.1 is tuned to isolate the 3/rev and 4/rev rotor harmonics (frequencies highlighted by the dark-gray bars in Fig. 3.2). The baseline system has no fluid and a stiff pitch link so it simply consists of the mass, m, suspended by the stiffness, k_o, with an assumed c_o

equal to 10% of critical. The baseline frequency response shows a peak near 4.5/rev but no zeros. The out-of-phase transfer function includes the fluid and pitch-link stiffness, introducing a second peak and a zero. Figure 3.2(a) shows peaks near 2/rev and 6/rev and a zero at the desired 3/rev frequency. As shown in Table 3.2, the 3/rev and 5/rev loads are reduced by 76% and 50%, respectively. The 1/rev loads are approximately the same. Figure 3.2(b) shows a zero at 4/rev and peaks near 3/rev and 6/rev. The targeted 4/rev load decreases by 87% but the 2/rev and 6/rev loads increase.

3.1.2 Fluidic Circuit II

The fluidic circuit shown in Fig. 3.3 is similar to the one in Fig. 3.1, but it facilitates targeted loads reduction at two *even* harmonics and one *odd* harmonic because it has two vertical fluid tracks, each of which terminates in an accumulator. To achieve the desired fluid heights, water is added to both vertical tracks, and both accumulators are pre-pressurized. The accumulator pre-pressures are then further adjusted until the desired fluid levels are obtained. For this device, Eqs. (3.9)-(3.11) become, respectively,

$$p_m - p_{a_i} = I_{v_i} \dot{Q}_{a_i} + R_{v_i} Q_{a_i}, \quad i = 1,\ 2, \tag{3.16}$$

$$\dot{p}_{a_i} = \frac{1}{C_{a_i}} Q_{a_i}, \quad i = 1,\ 2, \tag{3.17}$$

$$Q_1 + Q_2 = Q_{a_1} + Q_{a_2}. \tag{3.18}$$

The other system equations are the same as for the previous device. The force transfer function for the out-of-phase forcing case is the same as Eq. (3.13) with $a_1, ..., a_5,\ b_1, ..., b_3$
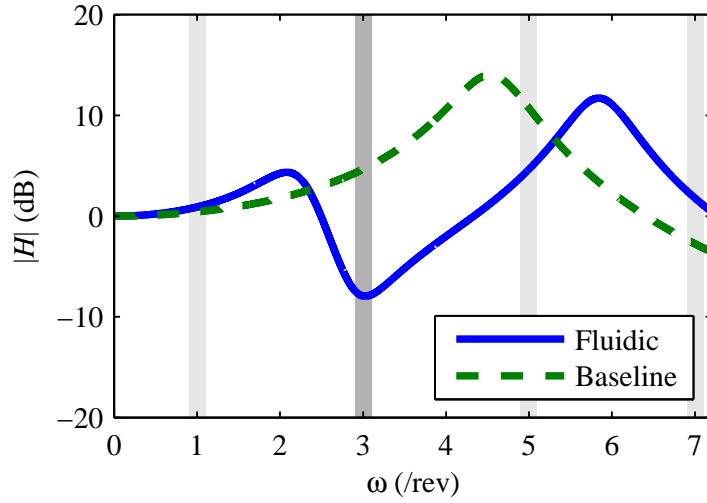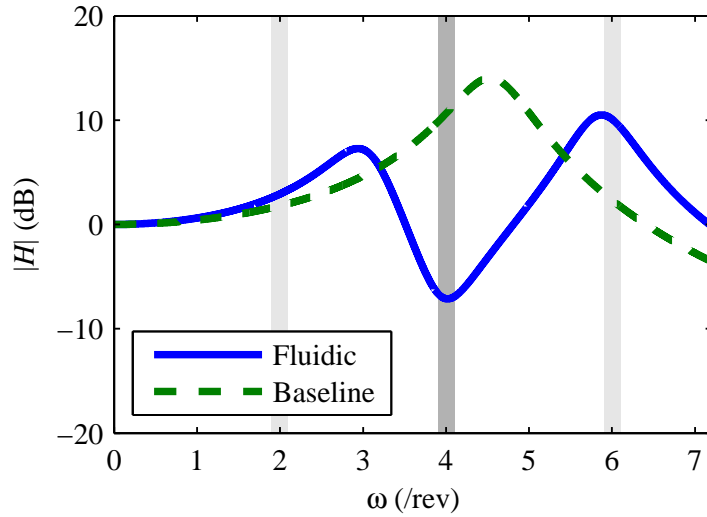
Figure 3.2. Full-scale representative system frequency response of two coupled fluidic pitch links with a single vertical fluid track. (See Fig. 3.1.)

defined in Appendix B. For in-phase forcing, the transfer function is

$$H(s) = \frac{b_1 s^4 + b_2 s^3 + b_3 s^2 + b_4 s + b_5}{a_1 s^6 + a_2 s^5 + a_3 s^4 + a_4 s^3 + a_5 s^2 + a_6 s + a_7}, \tag{3.19}$$

where the coefficients, a_i and b_i, are defined in Appendix B. This transfer function has two zeros and three poles. The design parameters are shown in Table 3.1. The piston diameter, the fluid track diameter, and the horizontal fluid track length are the same as Fluidic Circuit I. The two vertical fluid track lengths are 34 cm and 4 cm, and the corresponding accumulator lengths are 63 cm and 8 cm, respectively. Following the design procedure stated above, but now choosing C_{a_1}, C_{a_2}, I, I_{v_1}, and I_{v_2} as given in Table 3.1 to isolate 2/rev, 3/rev, and 4/rev harmonic loads, produces the response shown in Fig. 3.4. The out-of-phase transfer function has two well-spaced poles, and one zero (at the targeted 3/rev frequency). As shown in Table 3.2, the 3/rev response is reduced by 76% from the baseline value with little impact on the 1/rev loads. The in-phase transfer function has three poles, and two zeros (at the targeted 2/rev and 4/rev frequencies). The 2/rev and 4/rev harmonics are reduced by 19% and 86% from the baseline value, respectively. The 6/rev harmonic, however, increases by 161% from the baseline value.

3.1.3 Fluidic Circuit III

The two in-line accumulators in the fluidic circuit shown in Fig. 3.5 are sections of soft tubing. The volume of each section of soft tubing increases for a net flow into the accumulator and decreases for a net flow out of the accumulator. This device is similar to the one in [44], but the accumulators provide additional degrees of freedom for out-of-phase and in-phase forcing resulting in loads reduction at two *odd* harmonics and one
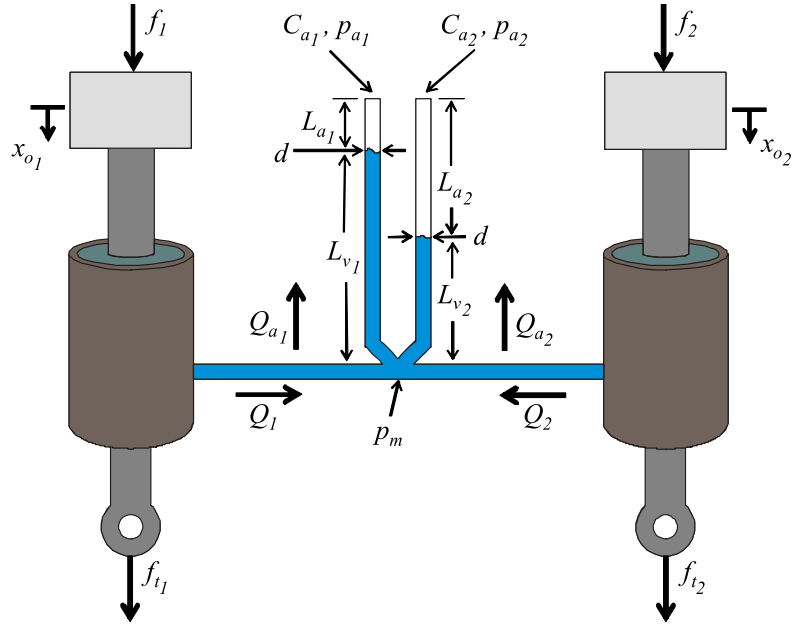
Figure 3.3. Schematic of Fluidic Circuit II.

even harmonic. The lumped-parameter fluidic circuit equations for this device are

$$p_i - p_{a_i} = I\dot{Q}_i + R_f Q_i, \ \ i = 1, \ 2 \tag{3.20}$$

and

$$p_{a_1} - p_{a_2} = I_3\dot{Q}_3 + R_3 Q_3. \tag{3.21}$$

The pressure change in the first accumulator

$$\dot{p}_{a_1} = \frac{1}{C_a}(Q_1 - Q_3), \tag{3.22}$$

and the pressure change in the second accumulator

$$\dot{p}_{a_2} = \frac{1}{C_a}(Q_2 + Q_3). \tag{3.23}$$
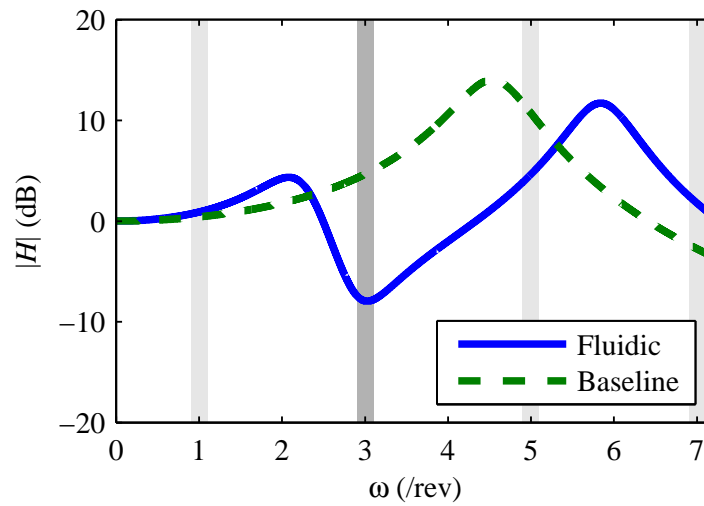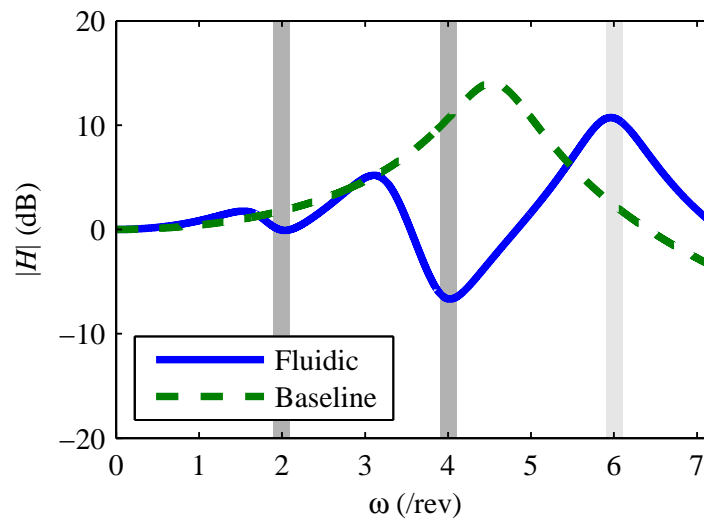
Figure 3.4. Full-scale representative system frequency response of two coupled fluidic pitch links with two vertical fluid tracks. (See Fig. 3.3.)

Since these accumulators are filled with water, Eq. (3.4) does not apply. The capacitance

of these accumulators is a function of material properties, tube geometry, and system

pre-pressure. The force transfer function for this configuration with out-of-phase forcing

is of the same form as Eq. (3.19) (two real zeros), and the transfer function for in-

phase forcing is of the same form as Eq. (3.13) (one real zero) (coefficients defined in Appendix B). Choosing C_a, I, and I_3 as given in Table 3.1 to isolate the 3/rev, 4/rev, and 5/rev harmonic loads produces the response shown in Fig. 3.6. As shown in Table 3.2, the 3/rev and 5/rev harmonics are reduced by 71% and 88%, respectively, with little impact on the 1/rev loads. The 7/rev loads, however, are amplified. The in-phase forcing shows a 93% reduction at the targeted 4/rev harmonic with amplification at the 2/rev and 6/rev harmonics.

The fluid motion may be described in terms of modes. For out-of-phase forcing, there are two modes (and two zeros in the out-of-phase frequency response). The first mode consists of *all* of the fluid moving as a slug back and forth between the two *pitch links*. This mode primarily affects the zero at 3/rev. The second mode consists of the slug of fluid in the *center fluid track* oscillating between the two *accumulators*. This mode primarily affects the zero at 5/rev. For in-phase forcing, there is a single mode (and one zero in the in-phase frequency response) – the fluid flows out of each pitch link simultaneously and into each accumulator. The fluid in the center fluid track remains stationary.

3.1.4 Summary of Analytic Study

A summary of the responses at the rotor harmonics of the three different systems is shown in Fig. 3.7. Fluidic Circuit II provides the best 2/rev loads reduction. All three fluidic circuits significantly reduce the 3/rev pitch-link loads. Fluidic Circuit III gives

Table 3.1. Simulation parameters for full-scale representative system.

	Description	Parameter	Value
Rotor System	Elastomer damping	c_d	$0 \, \frac{\text{N·s}}{\text{m}}$
	Baseline damping	c_o	$870 \, \frac{\text{N·s}}{\text{m}}$
	Pitch-link capacitance	C_p	$0 \, \frac{\text{m}^3}{\text{Pa}}$
	Fluidic circuit pipe diameter	d	0.007 m
	Piston diameter	D	0.05 m
	Elastomer stiffness	k_d	$460 \, \frac{\text{kN}}{\text{m}}$
	Baseline stiffness	k_o	$540 \, \frac{\text{kN}}{\text{m}}$
	Equivalent pitch inertia	m	35 kg
	System pre-pressure (gage)	p_{a_o}	35 kPa
	Flow resistance per length	r	$5.0\text{e}8 \, \frac{\text{Pa·s}}{\text{m}^3}/\text{m}$
	Fluid (water) density	ρ	$1000 \, \frac{\text{kg}}{\text{m}^3}$
	Rotor rotation rate	Ω	$27 \, \frac{\text{rad}}{\text{s}}$
Fluidic Circuit I	Accumulator capacitance	C_a	$1.13\text{e-}11 \, \frac{\text{m}^3}{\text{Pa}}$
	Horizontal fluid track half-inertance	I	$1.90\text{e}7 \, \frac{\text{kg}}{\text{m}^4}$
	Vertical fluid track inertance	I_v	$3.38\text{e}6 \, \frac{\text{kg}}{\text{m}^4}$
	Horizontal fluid track half-length	L	0.73 m
	Accumulator length	L_a	0.04 m
	Vertical fluid track length	L_v	0.13 m
Fluidic Circuit II	Accumulator 1 capacitance	C_{a_1}	$1.82\text{e-}10 \, \frac{\text{m}^3}{\text{Pa}}$
	Accumulator 2 capacitance	C_{a_2}	$2.26\text{e-}11 \, \frac{\text{m}^3}{\text{Pa}}$
	Horizontal fluid track half-inertance	I	$1.90\text{e}7 \, \frac{\text{kg}}{\text{m}^4}$
	Vertical fluid track 1 inertance	I_{v_1}	$8.83\text{e}6 \, \frac{\text{kg}}{\text{m}^4}$
	Vertical fluid track 2 inertance	I_{v_2}	$1.04\text{e}6 \, \frac{\text{kg}}{\text{m}^4}$
	Horizontal fluid track half-length	L	0.73 m
	Accumulator 1 length	L_{a_1}	0.63 m
	Accumulator 2 length	L_{a_2}	0.08 m
	Vertical fluid track 1 length	L_{v_1}	0.34 m
	Vertical fluid track 2 length	L_{v_2}	0.04 m
Fluidic Circuit III	Accumulator capacitance	C_a	$2.89\text{e-}11 \, \frac{\text{m}^3}{\text{Pa}}$
	Outer fluid track inertance	I	$1.35\text{e}7 \, \frac{\text{kg}}{\text{m}^4}$
	Center fluid track inertance	I_3	$5.46\text{e}6 \, \frac{\text{kg}}{\text{m}^4}$
	Outer fluid track length	L	0.52 m
	Center fluid track length	L_3	0.21 m
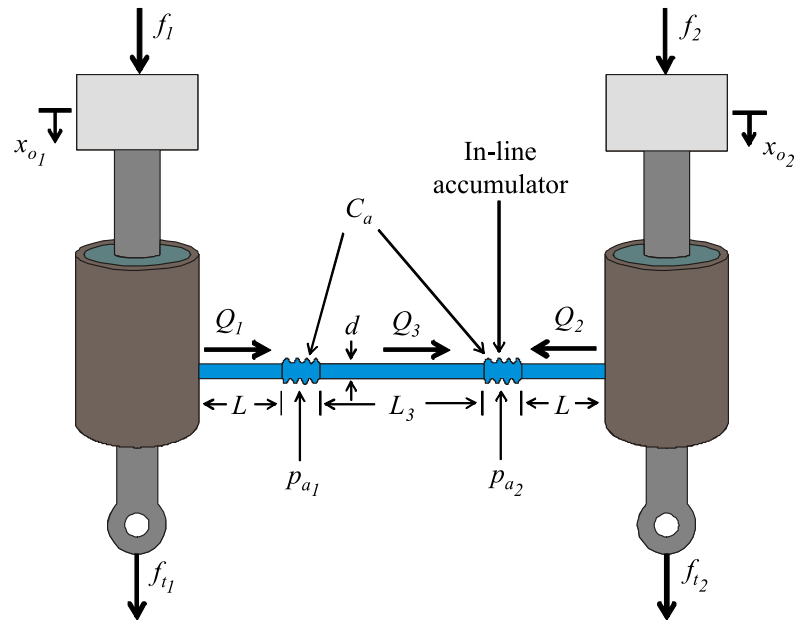
Figure 3.5. Schematic of Fluidic Circuit III.

the best 4/rev and 5/rev loads reduction. All three fluidic circuits increase the 6/rev and

7/rev pitch-link loads.

3.2   Experimental Validation – Fluidic Circuit I

The analysis for each of the three fluidic circuits in the previous sections predicts multi-

harmonic isolation. To demonstrate the performance of Fluidic Circuit I and Fluidic

Circuit III, two benchtop tests are conducted.

Figure 3.8 shows the experimental setup used to validate the model for Fluidic Cir-

cuit I and demonstrate multi-harmonic isolation. Each fluidic pitch link is represented by

a diaphragm pump, consisting of a thin disk of rubber clamped at the edges by a plastic

housing. A threaded rod passes through the center of the diaphragm and is clamped
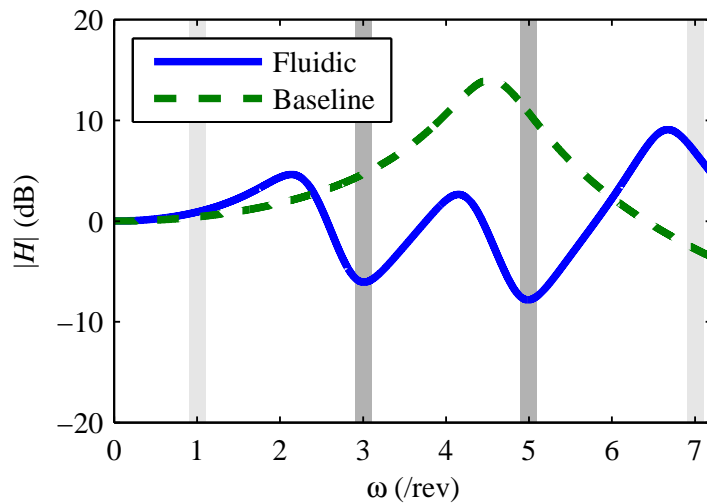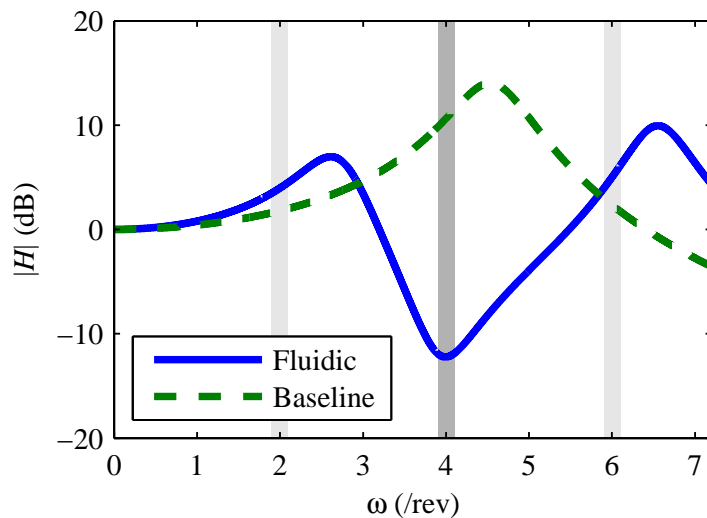
Figure 3.6. Full-scale representative system frequency response of two coupled fluidic pitch links with two in-line accumulators. (See Fig. 3.5.)

to the diaphragm by a washer and nut on each side. (The diaphragm pump is similar to the piston pump used in the analysis sections in that oscillatory motion of the rod deflects the diaphragm, causing fluid to flow into and out of the pitch link.) The mass is suspended from the rod and attached to the stinger of an electromagnetic shaker. Clear
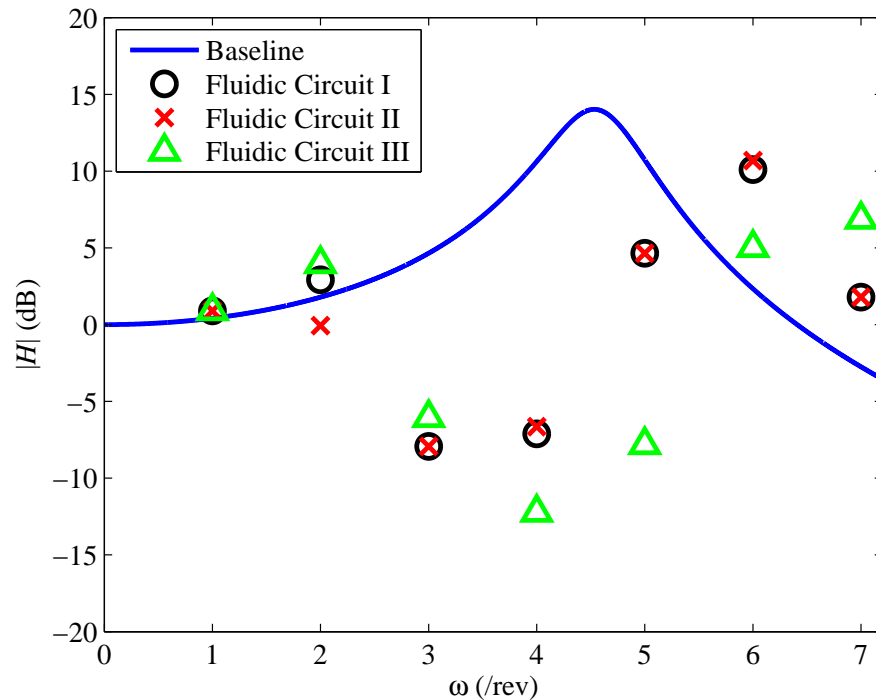
Figure 3.7. Summary of the full-scale representative system frequency responses at the rotor harmonics of two coupled fluidic pitch links with three different fluidic circuits.

Polyvinyl Chloride (PVC) pipe connects the two diaphragm pumps. The vertical fluid track is attached to a tee in the center of the horizontal connecting pipe. The system is filled, then pre-pressurized to prevent cavitation. A Ling LMT-100 shaker and a Vibration Test Systems VG100A-6 shaker excite the system. Force transducers from PCB Piezotronics, Inc. measure the input and transmitted forces (Models 208C02 and 208C01, respectively). A National Instruments LabVIEW system sends chirp signals to the shakers and calculates the input-force-to-transmitted-force frequency response functions based on the resulting force-transducer signals.

Table 3.2. Transmitted loads reduction for full-scale representative system simulation.

	Frequency (/rev)	Baseline (dB)	Fluidic Circuit (dB)	Reduction (%)
	1	0.4	0.9	-6
	2	1.8	2.9	-14
Circuit I	3	4.6	-7.9	76
	4	10.6	-7.1	87
	5	10.7	4.6	50
	1	0.4	0.9	-6
	2	1.8	-0.1	19
Circuit II	3	4.6	-7.9	76
	4	10.6	-6.6	86
	5	10.7	4.6	50
	1	0.4	0.9	-6
	2	1.8	4.0	-28
Circuit III	3	4.6	-6.1	71
	4	10.6	-12.2	93
	5	10.7	-7.8	88

Two experimental runs are conducted to test two different driving conditions. The two shakers drive out-of-phase for the first run and in-phase for the second run. Figure 3.9 shows the experimental frequency responses for both out-of-phase and in-phase forcing for one pitch link compared to the predicted responses. From symmetry, we expect and observe similar performance in the other pitch link. (See Appendix C for the frequency responses of both pitch links and the associated Matlab® code.) Although not shown, the corresponding phase curves decrease and increase, respectively, at the

pole and zero frequencies. The baseline curves are for the system with "no fluid." The baseline model includes only the mass, diaphragm stiffness, and diaphragm damping. (We neglect the stiffness due to the compressibility of the enclosed air because it is much less than the diaphragm stiffness.) The diaphragm stiffness is calculated from the baseline natural frequency and mass. The diaphragm damping is determined by adjusting c_d until the amplitudes of the theoretical and experimental baseline curves match. The theoretical and experimental curves lie on top of each other, showing a resonant peak at 23.7 Hz. The experimental and theoretical responses for the system "with fluid" also match well with the model parameters given in Table 3.3. The pitch-link capacitance is determined by measuring the change in volume of the pitch link as the pitch-link pressure changes. We assume the flow resistance per unit length to be constant, and we determine the effective flow resistance by adjusting r until the amplitudes of the peaks and zeros of the theoretical and experimental curves coincide. The remaining parameters come from dimensions as well as capacitance and inertance formulas. Since the pipe and fittings have different diameters, the inertance for a given fluid track is the sum of the inertances for each section within that fluid track. The baseline system and the system "with fluid" exhibit the same low-frequency behavior, in both forcing cases. The isolation frequency in the out-of-phase-forcing case occurs at 10.6 Hz, where the transmitted load is reduced by 55% from the baseline case. For the in-phase-forcing case, 71% of the baseline load is reduced at the isolation frequency at 16.9 Hz. Table 3.4 summarizes the experimentally measured performance.

3.3 Experimental Validation – Fluidic Circuit III

The objective of this circuit is to provide isolation at two odd harmonics and one even harmonic. Figure 3.10 shows the upper portion of the experimental setup used to validate the model for Fluidic Circuit III. (The lower portion is unchanged from the experimental setup for Fluidic Circuit I.) Each of the two in-line accumulators consists of a section of rubber tubing that is clamped at both ends to the PVC pipe. An external structure supports the fluid track between the two accumulators.

Figure 3.11 shows the experimental frequency responses for both out-of-phase and in-phase forcing compared to the predicted responses for one pitch link. (See Appendix C for the frequency responses of both pitch links and the associated Matlab® code.) The corresponding phase curves (not shown) decrease and increase, respectively, at the pole and zero frequencies. The baseline curve is again the frequency response of the system with "no fluid," and the theoretical and experimental curves show a single resonance at 23.7 Hz. The experimental and theoretical responses for the system "with fluid" also match well. The model parameters are given in Table 3.3. The baseline system and the system "with fluid" exhibit the same low-frequency behavior, in both forcing cases. The isolation frequencies in the out-of-phase-forcing case occur at 10.9 Hz and 20.9 Hz, where the transmitted loads are reduced by 40% and 89% from the baseline case, respectively. For the in-phase-forcing case, 81% of the baseline load is reduced at the isolation frequency of 17.6 Hz. Table 3.4 summarizes the experimental performance.
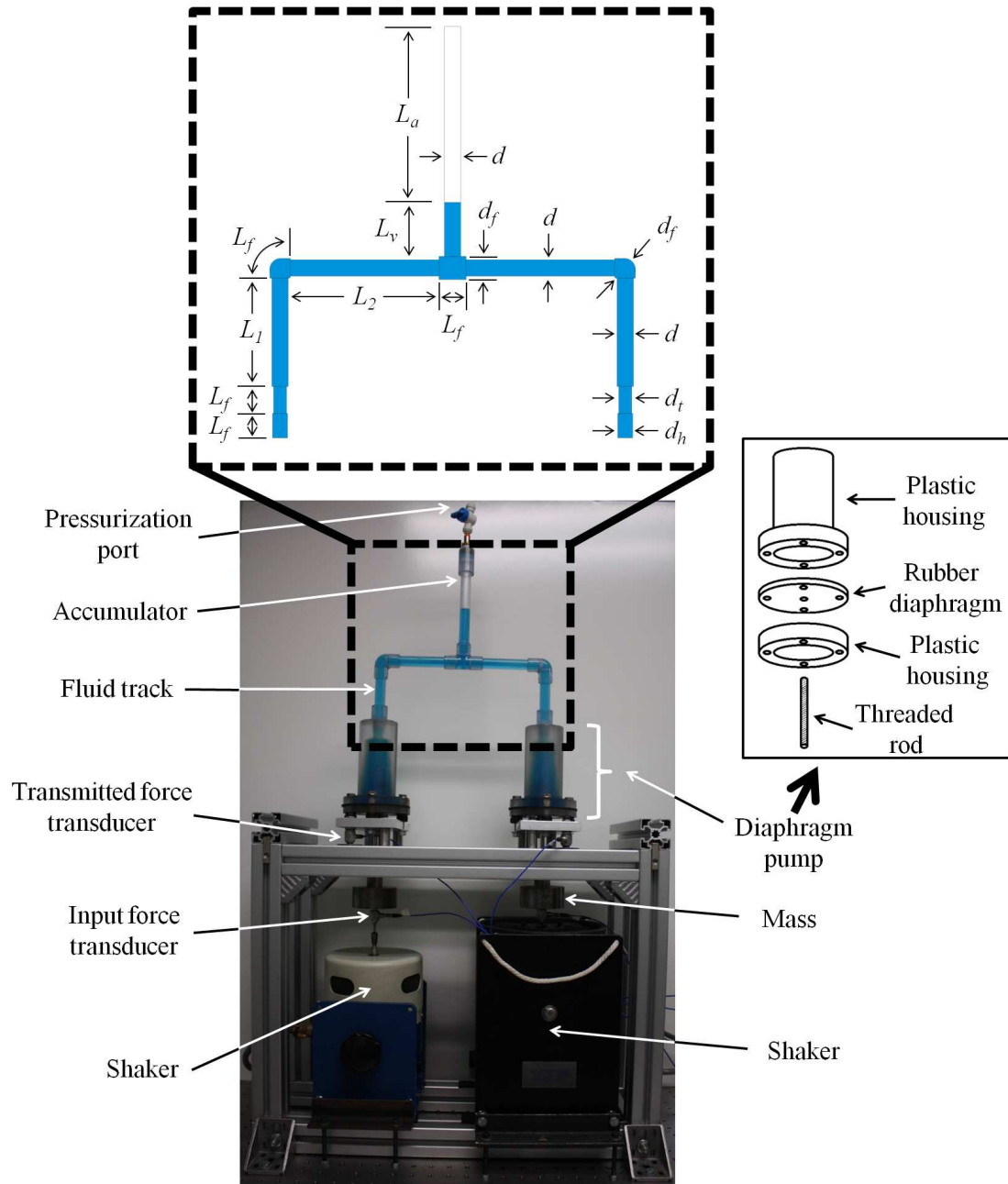
Figure 3.8. Fluidic Circuit I experimental setup.

Figure 3.9. Frequency response of two coupled pitch links with a single vertical fluid track.
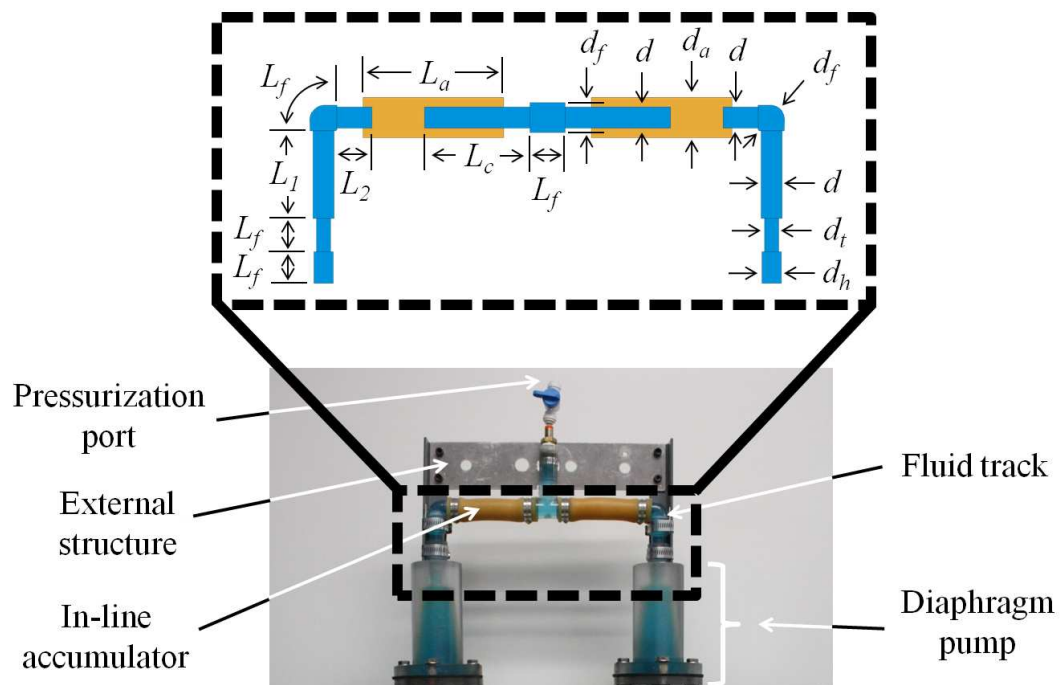
Figure 3.10. Fluidic Circuit III experimental setup.
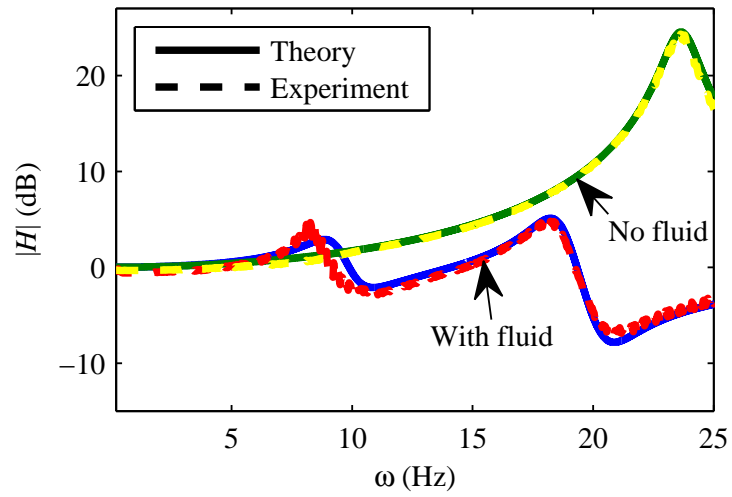
(a) Out−of−phase forcing
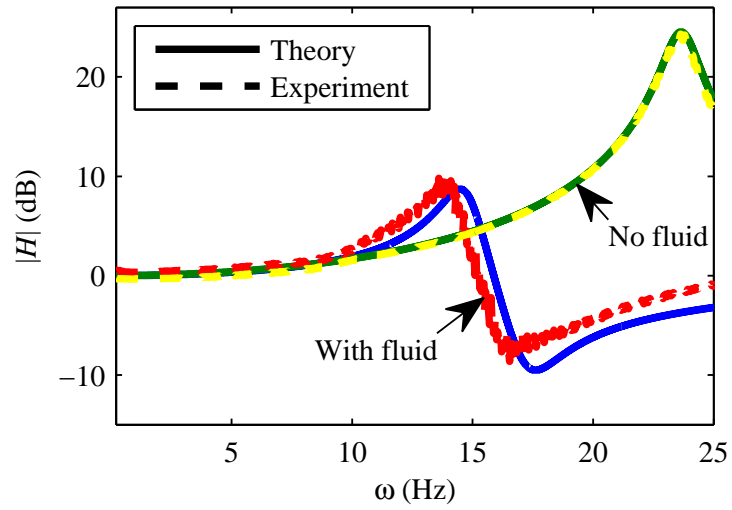
(b) In−phase forcing

Figure 3.11. Frequency response of two coupled pitch links with two in-line accumulators.

Table 3.3. Experimental parameters.

	Description	Parameter	Value
	Mass	m	1.13 kg
Pitch-Link Components	Diaphragm damping	c_d	$10\ \frac{\text{N·s}}{\text{m}}$
	Baseline damping	c_o	$0\ \frac{\text{N·s}}{\text{m}}$
	Pitch-link capacitance	C_p	1.7e-11 $\frac{\text{m}^3}{\text{Pa}}$
	Effective piston diameter	D	0.044 m
	Diaphragm stiffness	k_d	$25\ \frac{\text{kN}}{\text{m}}$
	Stinger stiffness	k_o	$\sim\infty$
	Diaphragm thickness	t	0.0032 m
Fluidic Circuit Components	Pipe inner diameter	d	0.012 m
	Fitting inner diameter	d_f	0.017 m
	Fitting inner diameter	d_h	0.011 m
	Fitting length	L_f	0.02 m
	System pre-pressure (gage)	p_{a_o}	50 kPa
	Fluid (water) density	ρ	$1000\ \frac{\text{kg}}{\text{m}^3}$
Fluidic Circuit I Components	Accumulator capacitance	C_a	9.8e-11 $\frac{\text{m}^3}{\text{Pa}}$
	Fitting inner diameter	d_t	0.010 m
	Connecting fluid track half-inertance	I	2.3e6 $\frac{\text{kg}}{\text{m}^4}$
	Vertical fluid track inertance	I_v	2.6e5 $\frac{\text{kg}}{\text{m}^4}$
	Pipe length	L_1	0.08 m
	Pipe length	L_2	0.11 m
	Accumulator length	L_a	0.13 m
	Vertical fluid track length	L_v	0.04 m
	Flow resistance per length	r	6.0e7 $\frac{\text{Pa·s}}{\text{m}^3}$/m
Fluidic Circuit III Components	Accumulator capacitance	C_a	2.0e-10 $\frac{\text{m}^3}{\text{Pa}}$
	Accum. inner diam. (unpressurized)	d_a	0.019 m
	Fitting inner diameter	d_t	0.008 m
	Outer fluid track inertance	I	1.3e6 $\frac{\text{kg}}{\text{m}^4}$
	Center fluid track inertance	I_3	1.1e6 $\frac{\text{kg}}{\text{m}^4}$
	Pipe length	L_1	0.05 m
	Pipe length	L_2	0.02 m
	Accumulator length	L_a	0.08 m
	Pipe length	L_c	0.06 m
	Flow resistance per length	r	1.1e8 $\frac{\text{Pa·s}}{\text{m}^3}$/m

Table 3.4. Transmitted loads reduction for experiments.

	Frequency	Baseline	Theory		Experiment	
			With Fluid	Reduction	With Fluid	Reduction
	(Hz)	(dB)	(dB)	(%)	(dB)	(%)
Circuit I	10.6 (out-of-phase)	1.8	-6.1	60	-5.2	55
	16.9 (in-phase)	6.1	-7.8	80	-4.8	71
	10.9 (out-of-phase)	2.0	-2.1	38	-2.5	40
Circuit III	17.6 (in-phase)	7.0	-9.5	85	-7.2	81
	20.9 (out-of-phase)	12.9	-7.8	91	-6.6	89

Impedance Tailored Fluidic Pitch Links for Passive Hub Vibration Control and Improved Rotor Efficiency

4.1 Fluidic Pitch Link Model

A schematic diagram of a fluidic pitch link is shown in Fig. 4.1. The pitch link has a piston of area A and mass m that is sealed and elastically restrained by an elastomer with damping c_d and stiffness k_d. The piston moves with displacement $x(t)$ in response to $F(t)$. For a given pitch-horn length, l_{ph}, $F(t)$ and $x(t)$ are related to the blade-root

pitching moment, $M_\theta(t)$, and the blade-root elastic twist, $\theta_r(t)$, respectively, by

$$F = \frac{M_\theta}{l_{ph}} \tag{4.1}$$

and

$$x = l_{ph}\theta_r. \tag{4.2}$$

The primary chamber of the pitch link has capacitance C_p and pressure, $p(t)$, generated by the motion of the piston as it forces fluid volume $V(t)$ into the fluid track. The fluid track has area a and length L. The fluid in the track has density ρ and lumped inertance I, where

$$I = \frac{\rho L}{a}. \tag{4.3}$$

We assume the resistance to fluid flow, R_f, of the fluid track is constant. The fluid track terminates in an accumulator with capacitance C_a and pressure $p_a(t)$.

This model of a fluidic pitch link has two degrees of freedom. Summing the forces on the piston gives the first equation of motion

$$m\ddot{x} + c_d\dot{x} + \left(k_d + \frac{A^2}{C_p}\right)x - \frac{A}{C_p}V = F. \tag{4.4}$$

The mechanical-fluidic coupling equation is

$$V = Ax - C_p p. \tag{4.5}$$

The equation for the fluid flow through the fluid track is

$$p - p_a = I\ddot{V} + R_f\dot{V}. \tag{4.6}$$
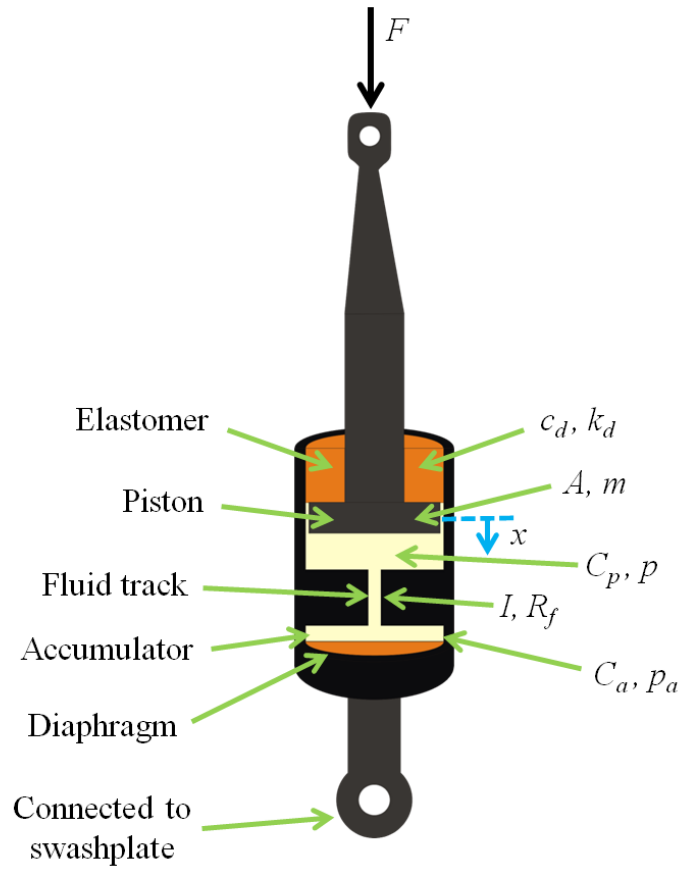
Figure 4.1. Schematic of a fluidic pitch link.

Fluid flow into, and out of, the accumulator dictates the change in accumulator pressure

$$\dot{p}_a = \frac{1}{C_a}\dot{V}. \tag{4.7}$$

Combining Eqs. (4.5)-(4.7) yields the second equation of motion

$$I\ddot{V} + R_f\dot{V} + \left(\frac{1}{C_a} + \frac{1}{C_p}\right)V - \frac{A}{C_p}x = 0. \tag{4.8}$$

4.2   Rotor Aeroelastic Simulation

The rotor aeroelastic simulation from [58] (See Appendix D for flow charts showing how the main subroutines in the aeroelastic simulation interact.) assumes N_b identical blades. The blade radius and rotation rate are the same as those of the UH-60. The rotor blade is modeled as a beam and divided into thirteen finite elements. Each element has eleven nodes – four each for flap and lag, and three for torsion. The root of the blade is hinged to permit flap and lag motions, and the root pitch is prescribed (no elastic root pitch). Aerodynamic loads are determined via a table lookup. Drees' model [62] is used to calculate the inflow. The steady, periodic response of the blade is calculated in modal space (three flap, three lag, and two torsion modes) using finite-element-in-time. Each of the eight time elements has six nodes. The resulting response is used to calculate the blade-root loads. After a propulsive trim converges, the resulting hub loads are reported as forces and moments in the coordinate system shown in Fig. 4.2.
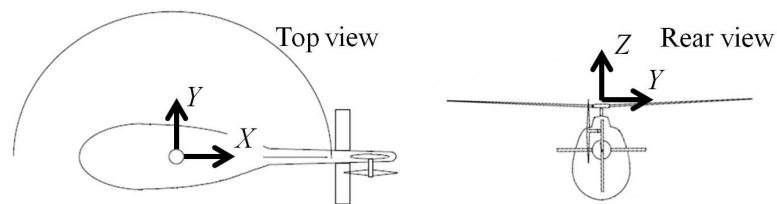
Figure 4.2. Coordinate system for hub loads.

Adding the fluidic pitch link model described above introduces one additional degree of freedom (fluid volume, V) to the rotor aeroelastic simulation. Also, the root of the blade can now pitch elastically in addition to the prescribed pitch necessary for trim.

The mass, damping, and stiffness matrices are modified to include the fluidic pitch link parameters. The introduction of the fluidic pitch link alters the response, which in turn, alters the blade-root loads, and thus, the hub loads. The change in blade pitch response also alters the required rotor power.

4.3   Parametric Study

To investigate the potential of fluidic pitch links to influence hub loads and rotor power, we conduct a series of aeroelastic simulations with reasonable fluidic pitch link parameters. (See Table 4.1.)   The following four fluidic pitch link parameters are varied: accumulator capacitance, elastomer stiffness, inertance, and piston area. These four parameters depend on fluidic pitch link geometry (piston diameter, accumulator volume, and fluid track length) and material properties. Each parameter is assigned three values, as shown in Table 4.2, resulting in eighty-one simulations.

The three best combinations that result in the highest reductions of the 4/rev hub loads are selected for further study and shown in Table 4.2. Figures 4.3-4.5 show the nondimensional 4/rev hub loads for each of these three cases. For Case 1, the longitudinal force, lateral force, and pitching moment are reduced by 47%, 91%, and 58%, respectively. For Case 2, the lateral force, rolling moment, and pitching moment are reduced by 53%, 41%, and 67%, respectively. Unfortunately, Cases 1 and 2 show a large increase in F_Z. Case 3, however, shows a slight decrease in F_Z with reductions in the lateral force, rolling moment, and pitching moment of 17%, 37%, and 20%,

<div align="center">

Table 4.1. Parameters for aeroelastic simulation.

</div>

	Description	Parameter	Value
	Blade-loading coefficient	$\frac{C_T}{\sigma}$	0.073
	Pitch-horn length	l_{ph}	0.18 m
	Blade mass per unit length	m_b	11.4 $\frac{\text{kg}}{\text{m}}$
Rotor System	Number of blades	N_b	4
	Blade radius	R	8.17 m
	Advance ratio	μ	0.3
	Rotor rotation rate	Ω	27 $\frac{\text{rad}}{\text{s}}$
	Piston area*	A	0.0046 m^2
	Elastomer damping	c_d	220 $\frac{\text{N·s}}{\text{m}}$
	Accumulator capacitance*	C_a	1.2e-10 $\frac{\text{m}^3}{\text{Pa}}$
	Pitch-link capacitance	C_p	1.2e-12 $\frac{\text{m}^3}{\text{Pa}}$
Fluidic Pitch Link	Inertance*	I	6.5e6 $\frac{\text{kg}}{\text{m}^4}$
	Elastomer stiffness*	k_d	657 $\frac{\text{kN}}{\text{m}}$
	Piston mass	m	0.44 kg
	Flow resistance	R_f	8.5e6 $\frac{\text{Pa·s}}{\text{m}^3}$

*Varied for parametric study

respectively. The simulation results clearly show that fluidic pitch links can influence all six components of the hub loads. While no case shows simultaneous reduction in all components, the authority and tunability of fluidic pitch links has been demonstrated.

To better understand how a fluidic pitch link changes the higher harmonic pitching motion of the blade and the hub loads, Fig. 4.6 shows the 2/rev – 5/rev amplitudes and phases of the elastic tip torsion response for Case 1 compared to the rigid pitch link case. The amplitude of the 2/rev elastic torsion response increases, but the amplitudes of the

Table 4.2. Parametric study parameter values and best-performing cases.

Symbol [Units]	Accumulator Capacitance $C_a \left[\frac{\text{m}^3}{\text{Pa}}\right]$	Elastomer Stiffness $k_d \left[\frac{\text{kN}}{\text{m}}\right]$	Inertance $I \left[\frac{\text{kg}}{\text{m}^4}\right]$	Piston Area $A \left[\text{m}^2\right]$
Value 1	1.2e-11	438	5.4e6	0.0037
Value 2	1.2e-10	657	6.5e6	0.0046
Value 3	2.4e-10	876	7.6e6	0.0056
Case 1	1.2e-10	657	7.6e6	0.0056
Case 2	1.2e-10	657	7.6e6	0.0037
Case 3	1.2e-11	438	7.6e6	0.0056

3/rev – 5/rev elastic torsion response decrease. The phases of all four fluidic pitch link harmonics differ from the rigid pitch link case.

The total elastic torsion response versus azimuth angle for Case 1 is shown in Fig. 4.7. The tip response of the blade with a fluidic pitch link differs noticeably from the blade with a rigid pitch link. Also, for the blade with a fluidic pitch link, the elastic root response differs from the elastic tip response, indicating the blade elastically twists in addition to the fluidic pitch link deflection.

The fluidic pitch link in Case 1 significantly reduces the 4/rev inplane hub shears, F_X and F_Y, by changing the 3/rev and 5/rev inplane *blade-root* shears. The radial root shear, f_x, and the chordwise root shear, f_y, are shown in Fig. 4.8. Inplane *hub* shears are reduced when f_x and f_y have similar magnitudes and a 90° phase difference. From Fig. 4.8, the 3/rev f_x and f_y with the fluidic pitch link are closer in magnitude than in the rigid pitch link case. This is also true for the 5/rev f_x and f_y. Furthermore, the phase difference between the 5/rev f_x and f_y with the fluidic pitch link (72°) is closer to 90°

(a) Hub forces

(b) Hub moments
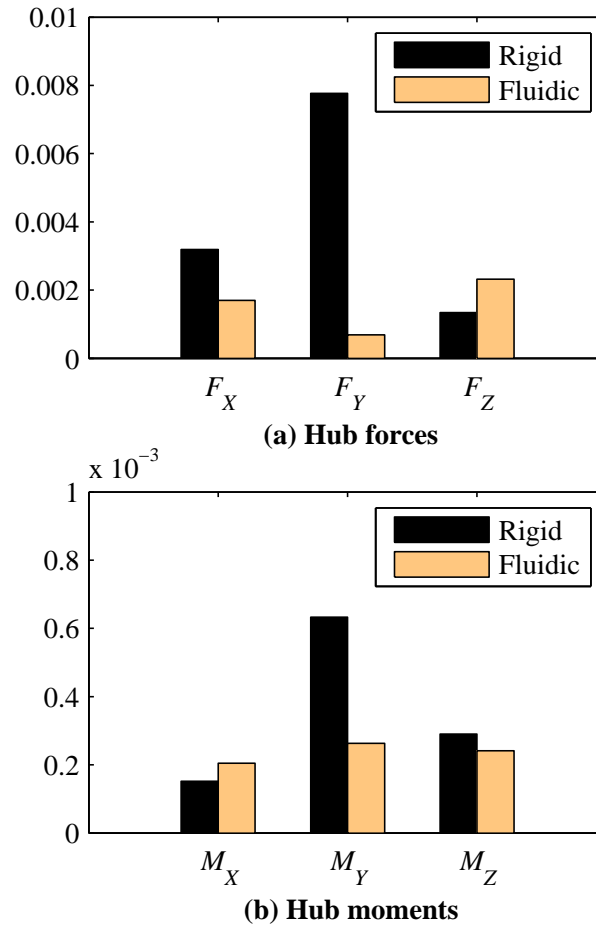
Figure 4.3. Nondimensional 4/rev hub loads for Case 1.

than in the rigid pitch link case ($41°$). These changes in the 3/rev and 5/rev blade-root

shears result in the reductions in 4/rev inplane hub shears in Case 1.

4.4 Impacts on Trim and Torsional Stability

Fluidic pitch links should not significantly impact trim or stability because the aircraft

will handle differently and may become unsafe. Table 4.3 shows the propulsive trim

(a) Hub forces

(b) Hub moments
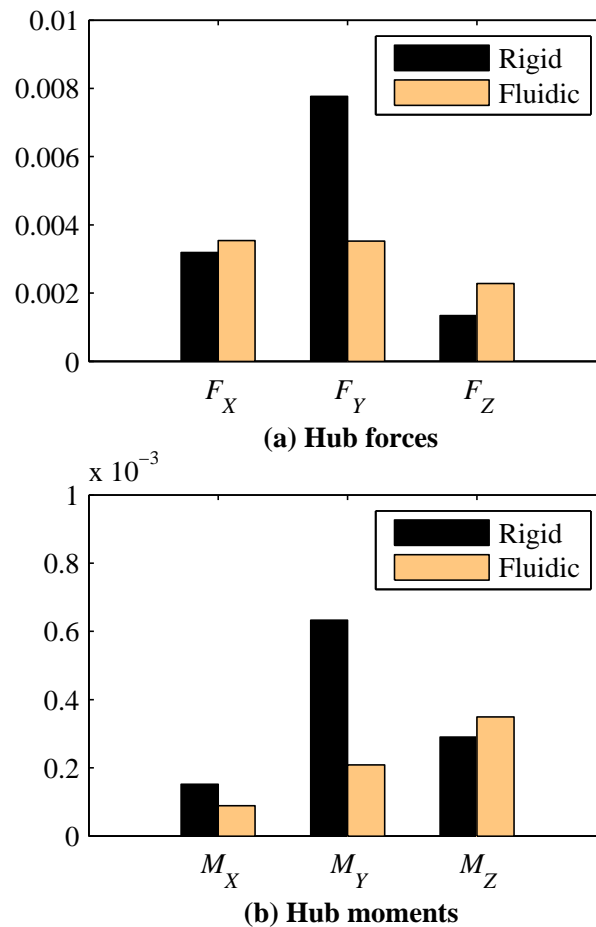
Figure 4.4. Nondimensional 4/rev hub loads for Case 2.

results of Cases 1–3. Introduction of a fluidic pitch link does not significantly change the vehicle trim. The largest discrepancy is in the cosine component of the cyclic pitch for Case 1 that differs from the rigid pitch link case by only $0.4°$. The aeroelastic simulation does not predict torsional stability, but the first torsion natural frequency is related to torsional stability. The first torsion natural frequency is significantly smaller for all three fluidic pitch link cases compared to the rigid pitch link case. This large reduction is due
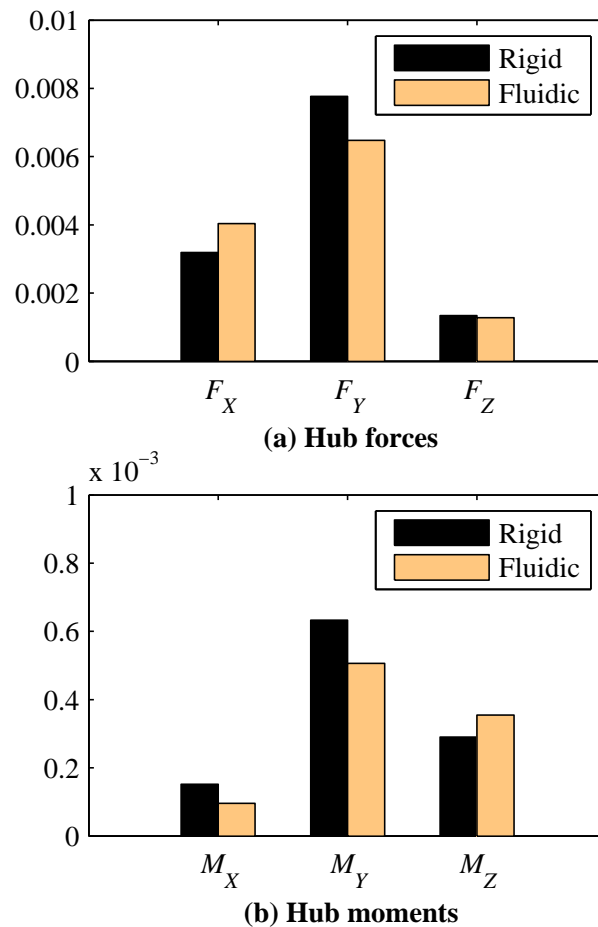
Figure 4.5. Nondimensional 4/rev hub loads for Case 3.

to the combined effects of decreased stiffness and increased inertia, resulting from the

relatively soft elastomer stiffness and the addition of fluid inertance, respectively. The

impact on rotor torsional stability is unclear, but the stability may be ameliorated by the

added damping provided by the fluid track resistance.

The elastomer stiffness may be increased, but the remaining pitch-link parameters

may also have to be changed to maintain a similar reduction in hub loads. For instance,
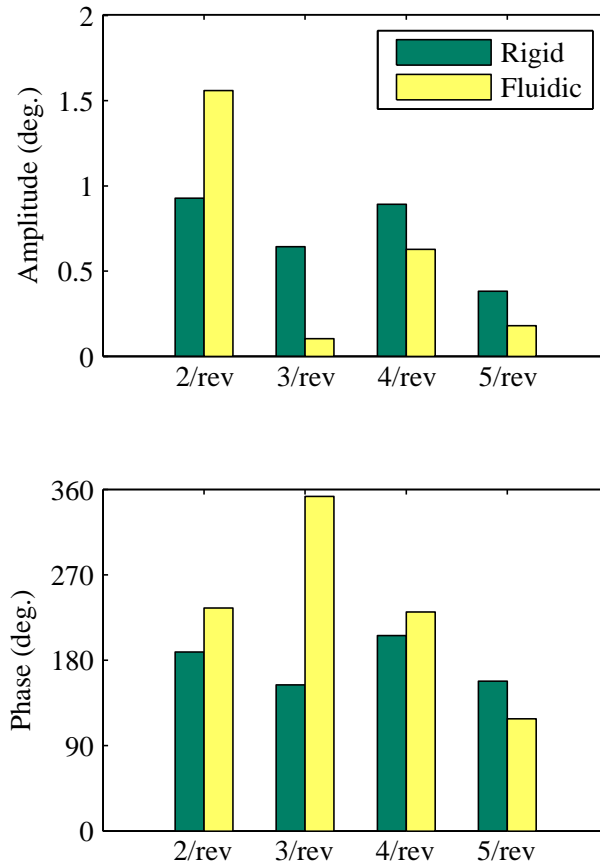
Figure 4.6. Amplitude and phase of higher harmonic pitching motion for Case 1.

doubling the elastomer stiffness for the pitch link in Case 2 increases the 4/rev lateral and pitching moment hub loads. If the elastomer stiffness is doubled, *and* the piston diameter and inertance are each increased by about 50%, the 4/rev pitching moment returns to nearly the same value as in the original Case 2 results. Interestingly, the aeroelastic simulation also predicts a reduction in the 4/rev vertical hub load with these modified parameters, as well as a significant increase in the required rotor power. If
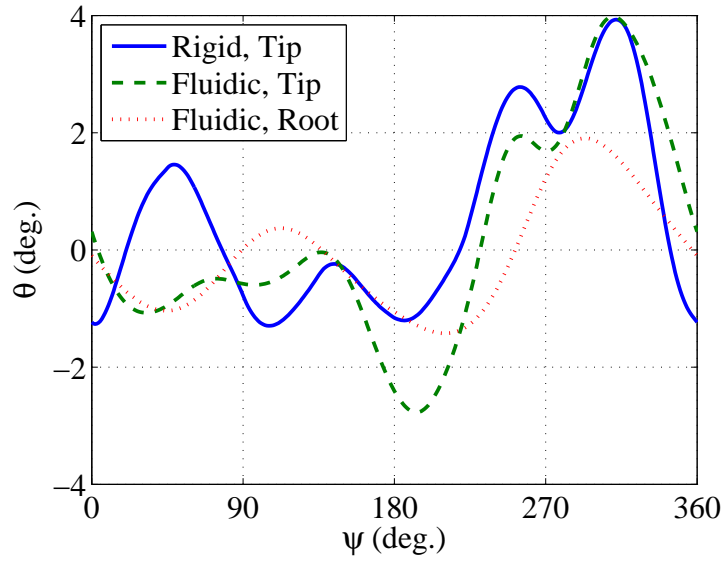
Figure 4.7. Elastic torsion response for Case 1.
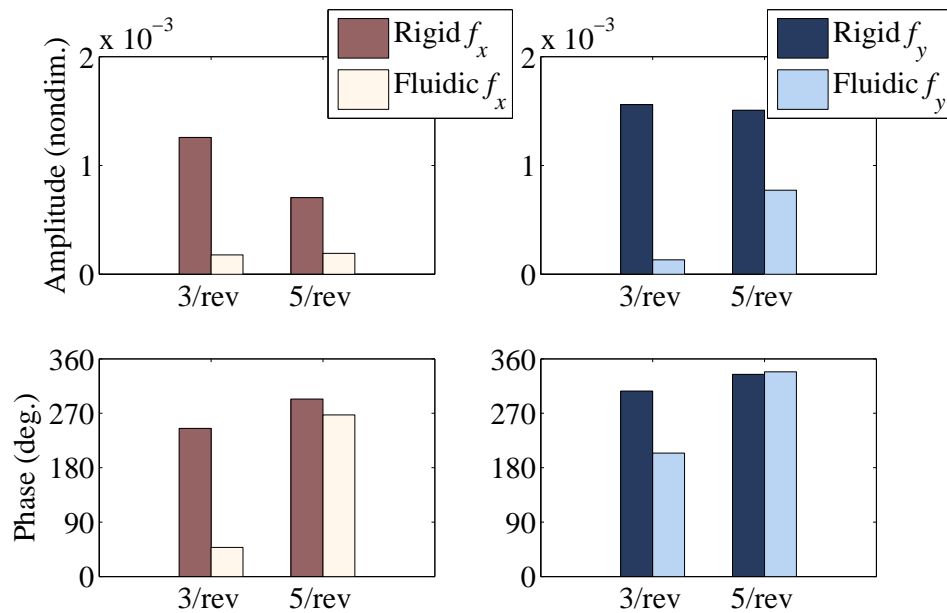
Figure 4.8. Inplane, 3/rev and 5/rev blade shears for Case 1.

Table 4.3. Propulsive trim and first torsion frequency for best-performing cases.

	Rigid Baseline	Case 1	Case 2	Case 3
Collective pitch (75% R)	7.7°	8.0°	8.0°	7.8°
Cyclic pitch (cosine component)	0.9°	1.3°	0.9°	0.8°
Cyclic pitch (sine component)	-7.6°	-7.5°	-7.5°	-7.5°
Forward shaft tilt	2.7°	2.5°	2.6°	2.8°
Lateral shaft tilt (roll right, positive)	-0.4°	-0.6°	-0.5°	-0.4°
Tail-rotor thrust (nondimensional)	0.20	0.21	0.20	0.19
First torsion natural frequency (/rev)	4.5	2.1	2.4	3.4

the elastomer stiffness is further increased to ten times its original value (and no other parameters are changed from the original Case 2), the 4/rev vertical hub load doubles, and the required rotor power decreases moderately. The remaining hub loads are very similar to the rigid pitch link baseline.

4.5 Rotor Efficiency

Higher harmonic pitching motion of the rotor blade can reduce the required rotor power, increasing the vehicle's efficiency. Power is reduced if the pitching motion of the blade decreases the steady torque on the rotor shaft. While the lift distribution of the rotor disk may be altered in the process, the total rotor thrust must remain constant to maintain vehicle trim. A 2/rev input with a phase that decreases the magnitude of the blade's angle of attack on the advancing side near 90° decreases the resulting drag on the blade. The associated loss in lift is compensated by the increase in the blade's angle of attack

at other azimuths. The lower air velocity at these angular positions results in a lower drag penalty than at azimuths close to $90°$.

Cases 1–3 studied above for vibration reduction result in a 4.0% *increase*, a 1.0% *increase*, and a 2.5% *decrease* in rotor power, respectively. The three cases from the parametric study with the largest increase in rotor efficiency predict power reductions of 5.0%, 3.7%, and 3.5%, respectively. The corresponding pitch-link parameters for these cases are shown in Table 4.4. Figure 4.9 shows the amplitudes and phases of the 2/rev – 5/rev pitching harmonics for the case with a 5.0% reduction in rotor power. Compared to the rigid pitch link case, the 2/rev amplitude and phase increase with the fluidic pitch link. Since the blade tip is pitched down on the advancing side in forward flight, increasing the 2/rev amplitude and phase would decrease the magnitude of the blade's angle of attack at azimuths near $90°$. This result is consistent with the explanation in the previous paragraph. The amplitudes and phases of the 4/rev and 5/rev harmonics decrease slightly. The 3/rev pitching motion is almost eliminated. The higher harmonic pitching motions of the 3.7% and 3.5% power reduction cases are similar to the 5.0% power reduction case.

Table 4.4. Fluidic pitch link parameters for highest rotor power reduction.

	Accumulator Capacitance	Elastomer Stiffness	Inertance	Piston Area
Symbol [Units]	$C_a \left[\frac{m^3}{Pa}\right]$	$k_d \left[\frac{kN}{m}\right]$	$I \left[\frac{kg}{m^4}\right]$	$A \left[m^2\right]$
5.0% power reduction	1.2e-10	876	6.5e6	0.0056
3.7% power reduction	1.2e-10	657	5.4e6	0.0056
3.5% power reduction	2.4e-10	876	7.6e6	0.0046
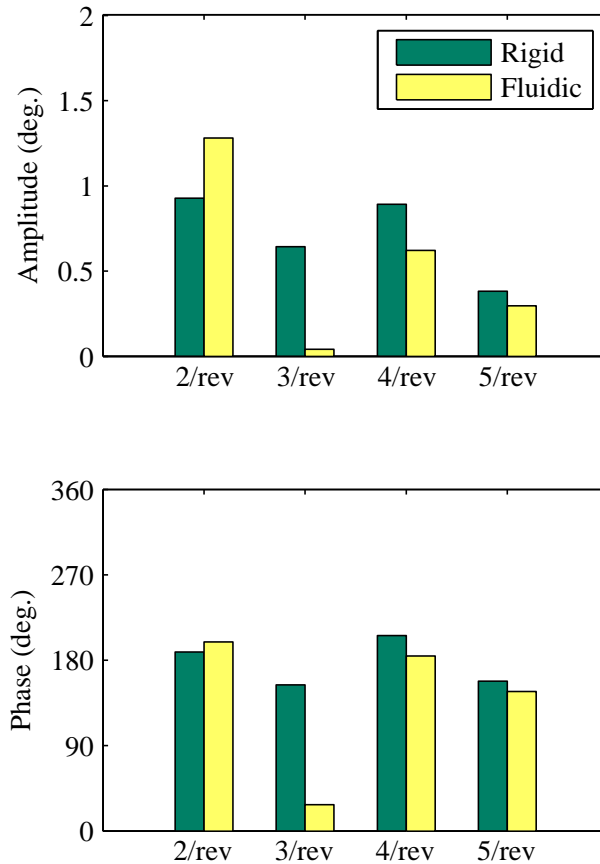
Figure 4.9. Amplitude and phase of higher harmonic pitching motion for the case with a 5.0% rotor power reduction.

Higher harmonic pitching motion that causes a decrease in required rotor power can increase hub vibration levels. Figure 4.10 shows the corresponding change in 4/rev hub loads for the case with a 5.0% reduction in rotor power. The longitudinal force and torsion moment are similar to the rigid pitch link case. The lateral force, rolling moment, and pitching moment are reduced by 54%, 35%, and 50%, respectively. Unfortunately,

the vertical force increases by 75%. Again, the changes in hub loads for the 3.7% and 3.5% power reduction cases are similar.

(a) Hub forces

(b) Hub moments
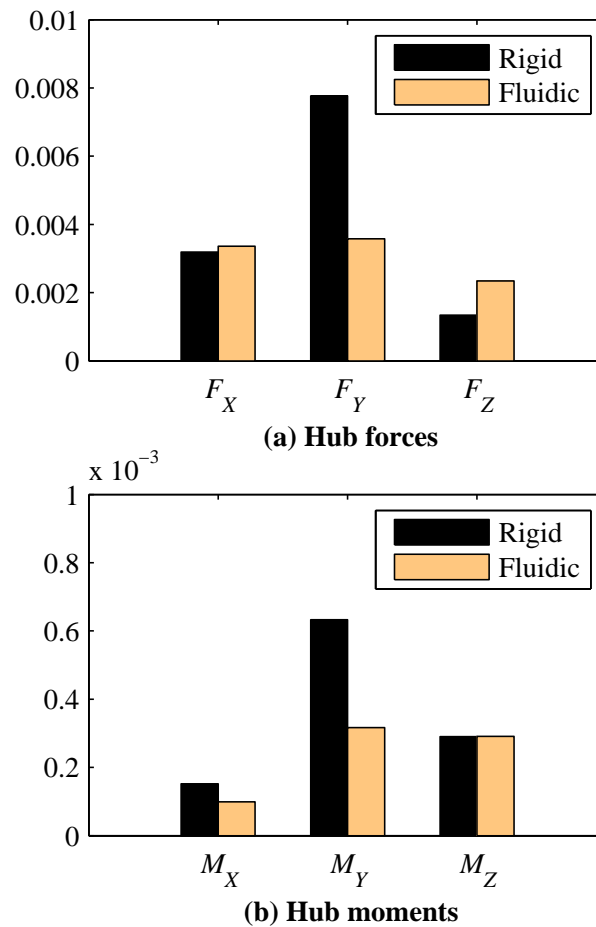
Figure 4.10. Nondimensional 4/rev hub loads for the case with a 5.0% rotor power reduction.

4.6   Semi-Active Fluidic Pitch Link

The optimal fluidic circuit that reduces the most vibration and/or power may depend on flight condition (advance ratio, maneuvering, *etc.*). Using valves, fluidic circuits

with different fluid track lengths, for example, could be switched in based on the flight regime. Another advantage of semi-active control is the ability to turn off the pitch links by closing the valves. Closing all the fluid tracks would prevent fluid flow, and the pitch link would mimic a rigid pitch link. To verify this behavior, Fig. 4.11 shows the aeroelastic simulation results with a fluidic pitch link that has been turned off. Apart from a modest increase in F_Z, all of the 4/rev hub loads for the fluidic pitch link with a closed orifice (no flow) match the rigid pitch link 4/rev hub loads. Thus, turning off a fluidic pitch link using valves results in the baseline, rigid pitch link performance.

(a) Hub forces

(b) Hub moments
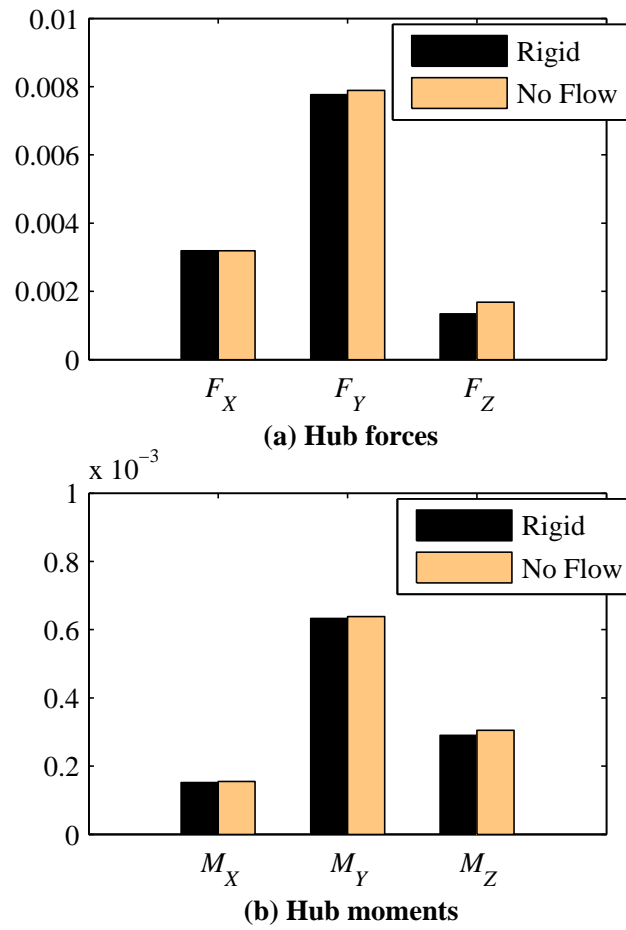
Figure 4.11. Nondimensional 4/rev hub loads for no fluid flow in the fluid track.

Chapter 5

Conclusions and Recommendations for Future Work

5.1   Fluidic Composite Tunable Vibration Isolators

Coupling a Fluidic Flexible Matrix Composite (F^2MC) to an air-pressurized fluid port produces a tunable vibration isolator. A nonlinear model describes the tube length as a function of pressure and axial load. Linearization of this static model and combination with the lumped-parameter fluid dynamics flow in the fluid port produces an overall system model. This model accurately predicts the primary resonance and isolation frequency of the transfer function from input force to transmitted force. The isolation frequency depends strongly on the fluid inertance. The isolation frequency can be tuned by varying the system pressure. Experimental results show a tunable isolation range from 9 Hz to 36 Hz with experimentally observed force reductions of 20 dB to 60 dB

at the isolation frequency. The isolation frequency is theoretically and experimentally shown to be relatively insensitive to changes in the isolated mass.

5.2   Coupled Pitch Links for Multi-Harmonic Isolation Using Fluidic Circuits

Replacing the stiff pitch links on rotorcraft having an even number of blades with coupled fluidic devices has the potential to reduce the higher harmonic blade loads transmitted through the pitch links to the swashplate. Analytical models of two fluidic devices coupled with three different fluidic circuits allow model-based tuning of the fluid inertances and capacitances to reduce the transmitted pitch-link loads for up to three main rotor harmonics. Each of the three circuits is the simplest configuration that results in loads reduction for the desired combination of out-of-phase and in-phase harmonics.

The simulation results using representative full-scale pitch-link parameters show loads reduction at the targeted out-of-phase and in-phase harmonics (3/rev and 4/rev, respectively) of 76% and 87%, respectively, for the fluidic circuit with a single vertical fluid track. The fluidic circuit with two vertical fluid tracks reduces the targeted out-of-phase harmonic load (3/rev) by 76% and the targeted in-phase harmonic loads (2/rev and 4/rev) by 19% and 86%, respectively. Pitch links coupled by a fluid track with two in-line accumulators reduce the targeted out-of-phase harmonic loads (3/rev and 5/rev)

by more than 71% and the targeted in-phase harmonic load (4/rev) by 93%. Increases in the non-targeted harmonics are observed.

Experimental results validate the theoretical predictions. The benchtop experiment for the fluidic circuit with a single vertical fluid track reduces the out-of-phase load and in-phase load by 55% and 71% at the respective isolation frequencies. Experimental results for the fluidic circuit with two in-line accumulators show out-of-phase loads reduction of 40% and 89% at the two isolation frequencies and in-phase loads reduction of 81% at the isolation frequency. Pitch-link loads may be amplified at a harmonic that is close to the primary resonance. The percent reductions of the experimental results differ from the theoretical percent reductions by less than 12%. Reducing the dissimilarity between pitch links, smoothing the fluid track, and replacing the diaphragm pumps with piston pumps should reduce the discrepancy between theory and experiment. Optimization of the benchtop experiments may further improve loads reduction performance.

5.3 Impedance Tailored Fluidic Pitch Links for Passive Hub Vibration Control and Improved Rotor Efficiency

Replacing rigid pitch links on rotorcraft with fluidic pitch links has the potential to reduce the vibratory hub loads and rotor power. A rotor aeroelastic simulation for a rotor similar to the UH-60 predicts reductions in the lateral hub force of up to 91% and

reductions in the hub rolling and pitching moments of up to 41% and 67%, respectively. Some of the remaining hub loads increase modestly. Rotor power reductions of up to 5% are also predicted. A semi-active fluidic pitch link with valves can have multiple fluid circuits that are switched in based on flight condition, including a fail-safe mode where the fluidic pitch link is rigid.

5.4   Summary

Coupling a Fluidic Flexible Matrix Composite (F^{2}MC) to an air-pressurized fluid port produces a fundamentally new class of tunable vibration isolator. This fluidlastic device provides significant vibration reduction at an isolation frequency that can be tuned over a broad frequency range. A unique feature of this device is that the port inertance depends on pressure so the isolation frequency can be adjusted by changing the air pressure. Experiments agree with theory, demonstrating a tunable isolation range from 9 Hz to 36 Hz and transmitted force reductions of up to 60 dB at the isolation frequency.

Replacing rigid pitch links on rotorcraft with coupled fluidic devices has the potential to reduce the aerodynamic blade loads transmitted through the pitch links. The simulation results show loads reduction at the targeted odd and even harmonics of up to 88% and 93%, respectively. The first and third fluidic circuits are validated with benchtop experiments and demonstrate loads reduction of up to 89% and 81% for out-of-phase and in-phase loads, respectively.

Replacing rigid pitch links on rotorcraft with fluidic pitch links has the potential to reduce the vibratory hub loads and rotor power. A rotor aeroelastic simulation for a rotor similar to the UH-60 predicts reductions in the lateral hub force of up to 91% and reductions in the hub rolling and pitching moments of up to 41% and 67%, respectively. Some of the remaining hub loads increase modestly. Rotor power reductions of up to 5% are also predicted.

5.5   Recommendations for Future Work

Three major practical aspects need to be analyzed before installing fluidic pitch links on rotorcraft. First, the effect of fluidic pitch links on the aeroelastic stability of the rotor is an unknown that urgently needs to be addressed. Rigid blade pitch-flap and pitch-flap-lag stability analyses should be conducted for both single fluidic pitch link and coupled fluidic pitch link configurations. The remaining two practical aspects are the robustness of fluidic pitch links to changing flight condition and sensitivity to variations in the design parameters. The rotor aeroelastic simulation should be conducted for representative flight conditions as well as fluidic pitch link parameter variations.

Another consideration for future work is accumulator design. The current air-over-fluid accumulators should be redesigned as sections of soft tubing, or a bladder should be inserted between the fluid and the air so that the behavior of the coupled pitch link system is not affected by changing orientation. Furthermore, pre-pressurization to

compensate for changing pressure with altitude and provision for fluid expansion with increasing temperature should be considered.

The models presented in the preceding chapters could be expanded to include additional material properties. For example, elastomer stiffness and damping depend on temperature, amplitude, and frequency [63, 64]. Replacing the simple lumped-parameter fluid models with Computational Fluid Dynamics (CFD) would permit the modeling of complex geometry and unsteady flow effects [65, 66]. Including more than just linear viscous damping would also improve the fidelity of the models. The nonlinearity introduced by the addition of CFD and more complete damping models would also improve the accuracy of future stability analyses.

Three additional items for future work include repeating the rotor aeroelastic simulation using a free-wake model for the inflow, adding a fluidic pitch link model to a coupled Computational Fluid Dynamics/Computational Structural Dynamics (CFD/CSD) analysis [59], and optimizing the fluidic pitch link design to achieve even further reduction of hub loads and increased rotor efficiency. A free-wake inflow model provides a time-averaged inflow that is more geometrically complex than the linear inflow distribution assumed by Drees' model [62]. The resulting change in aerodynamic loads would improve the accuracy of the predicted blade response and associated hub loads [67]. CFD/CSD analyses provide improved estimates of the blade pitching moment and blade pitch response, but the long run times required make them impractical for assessing a

large number of design cases or conducting a formal optimization. Before choosing an optimization method, the optimization work of [68] and [69, 70] should be reviewed.

In addition to the analysis and benchtop experiments already described, further analysis and testing is recommended. Coupling fluidic pitch links [43, 44] to improve failure modes may further reduce vibratory hub loads and increase rotor performance. Wind-tunnel tests should be conducted to study the centrifugal force effects on the fluidic pitch link system. Fatigue tests should be used to analyze the resilience of a design to the vibratory environment. Finally, theoretical predictions should be verified with flight tests.

5.6 Significant Contributions

Changing the system pressure of a flexible composite tunable vibration isolator adjusts the isolation frequency. This method of tuning is very simple and relatively easy to implement. Most tunable vibration isolators require significant alterations to the basic isolator design, such as adding an electric motor and mechanism to change the fluid track geometry. While the isolator of [19] is also tuned via pressure changes, the requirement to maintain a high air stiffness in the accumulators restricts the rate of tuning. Since changing the system pressure of a flexible composite tunable vibration isolator primarily affects the fluid track length and a high air stiffness in the accumulator is not required, a flexible composite tunable vibration isolator can be tuned rapidly.

A simple, tunable vibration isolator has multiple potential applications. Future helicopters with variable-speed rotors will require tunable vibration isolators that track the changes in rotor speed. A rapidly-tunable vibration isolator could also be used to increase passenger comfort in off-road vehicles. The isolators could either be integrated into the vehicle suspension or directly applied to the occupant's seat. An active control system using road preview [71] would tune the isolators to maximize passenger comfort.

Furthermore, the Fluidic Flexible Matrix Composite (F^2MC) can pump up to twenty times more fluid than a comparable piston pump [72]. Existing isolators can be re-designed more compactly with this increase in pumping efficiency. Because of the compactness of flexible composite vibration isolators and the simplicity of their design, they can be formed into arrays. These arrays of F^2MC isolators can then be tuned and inserted into composite panels to reduce structural vibration and noise.

Coupling fluidic rotorcraft pitch links with tuned fluidic circuits results in up to an 81% reduction of multiple harmonic pitch-link loads. The analytical results for the three fluidic circuits studied predict pitch link loads reductions that are approximately double the reductions achieved in [40] using spring-damper pitch links. In comparison to the directly coupled pitch links of [43, 44], the ability to target individual harmonics by configuring and tuning the connecting circuit gives the designer more control over the number of pitch-link loads to reduce as well as the extent of the reduction.

Multiple active blade pitch control approaches have been proposed and tested to reduce helicopter hub loads and to improve rotor efficiency. Although these active

control approaches are often effective, the complexity they add to the rotor increases cost and raises reliability and maintenance concerns. As such, helicopter manufacturers have yet to adopt any active blade pitch control designs. Replacing rigid pitch links with fluidic pitch links to passively reduce vibratory hub loads and improve rotor efficiency is much less complex than active control solutions, and similar fluidic devices are already standard equipment on some production rotorcraft.

The modified rotor aeroelastic simulation is the first rotorcraft comprehensive analysis to include a fluidic pitch link model. The rotor aeroelastic simulation results predict reductions in vibratory hub loads that exceed the moderate reductions predicted for passive spring-damper pitch links [53]. Furthermore, passively changing the higher harmonic pitch to increase the rotor efficiency is unique, and the predicted 5% decrease in required rotor power is significant. The fluidlastic devices used for pitch links in this study would be an excellent means to tune the impedance of many mechanical systems, as they permit significant tuning of the system mass, damping, and stiffness without adding much weight.

Source Code for F^{2}MC Isolator

A.1 Matlab® Code for F^{2}MC Isolator Pressure Plots

The following Matlab® code was used to generate Fig. 2.5. The code calls two functions,

exprII_dyn_I and exprII_dyn_II, which are given in the two sections following the code.

```matlab
%Lloyd Scarborough
%Created April 24, 2010
%Last modified November 14, 2013
%Code to generate pressure plots for F2MC isolator

close all
clear all
clc

global p F alpha Rio Roo Er Ep ds Ls nu rf delta m L lambda1

Rio=0.15;                   %initial inner tube radius, in
Roo=0.22;                   %initial outer tube radius, in
L=5+7/16;                   %initial tube length, in
alpha=(18.5)*pi/180;        %initial mesh angle, rad
Er=150;                     %Young's modulus of rubber, psi
nu=0.5;                     %Poisson's ratio of rubber
Ep=430000;                  %Young's modulus of mesh, psi
ds=0.008;                   %mesh strand diameter, in
Ls=L/cos(alpha);            %mesh strand length, in
m=80;                       %number of mesh strands
```

```matlab
rf=0.2;                             %radius of lower tube fitting, in
delta=11111115/16;                  %end effect dimension(making this value
                                    %   very large negates the end effect)

pr=[30 40 50 60];                   %vector of operating pressures, psi

for i=1:length(pr)

p_op=pr(i);                         %operating pressure, psi
F_op=26;                            %operating load, lbs

p_res=0.01;                         %resolution of pressure step, psi
lambda1_res=0.001;                  %resolution of lambda1

%Find lambda1_op
p=p_op;
F=F_op;
lambda1_op=fsolve('exprII_dyn_I',1);

%Find Ro_op
lambda2_op=sqrt(1-lambda1_op^2*(cos(alpha))^2)/sin(alpha);
t_op=(Roo-Rio)/(lambda1_op*lambda2_op);
Ro_op=0.5*(lambda2_op*(Rio+Roo)+t_op);

%Find Vtube_op (volume of tube without end effect), in^3
Vtube_op=pi.*((0.1e1-lambda1_op.^2.*cos(alpha).^2).^(1/2) ...
    ./sin(alpha).*(Rio+Roo)./0.2e1-(Roo-Rio)./lambda1_op ...
    .*(0.1e1-lambda1_op.^2.*cos(alpha).^2).^(-0.1e1./0.2e1) ...
    .*sin(alpha)./0.2e1).^2.*lambda1_op.*L;

%%%%%%%%%%%%%%%%%%%%%%%%%%%%%%%%%%%%%%%%%%%%%%%%%%%%%%%%%%%%%%%%%%%%%%%
%Port fluid level calculation
d1=0.38;                            %1/4" pipe ID, in
L1=6;                               %length of 1/4" pipe, in
a1=pi/4*d1^2;                       %area of 1/4" pipe, in^2
L1bT=2;                             %length of 1/4" lower leg of tee, in
L1tT=L1bT+d1;                       %length of lower leg of tee plus
                                    %   length of mid-section of tee, in
LT=1;                               %length of tee, in
dt=0.25;                            %clear tubing ID, in
Lt=46;                              %length of clear tubing, in
dct=0.5;                            %solid clear pipe ID, in
Lct=12;                             %length of solid clear pipe, in
dp=0.13;                            %diameter of peep tube, in

p_ref=30;                           %reference pressure, psi
F_ref=26;                           %reference load, lbs
Ltr=9.75;                           %reference height of fluid in system
                                    %   when p=p_ref and F=F_ref, in
```

```matlab
%Find V_ref (reference volume of tube without end effect), in^3
p=p_ref;
F=F_ref;
lambda1_ref=fsolve('exprII_dyn_I',1);
lambda2_ref=sqrt(1-lambda1_ref^2*(cos(alpha))^2)/sin(alpha);
t_ref=(Roo-Rio)/(lambda1_ref*lambda2_ref);
Ro_ref=0.5*(lambda2_ref*(Rio+Roo)+t_ref);
V_ref=pi.*((0.1e1-lambda1_ref.^2.*cos(alpha).^2).^(1/2)./sin(alpha) ...
    .*(Rio+Roo)./0.2e1-(Roo-Rio)./lambda1_ref.*(0.1e1 ...
    -lambda1_ref.^2.*cos(alpha).^2).^(-0.1e1./0.2e1).*sin(alpha) ...
    ./0.2e1).^2.*lambda1_ref.*L;

if Ltr<L1
    if Ltr<L1bT
        %Calculation of total amount of fluid in system, in^3
        Vwater=V_ref+pi/4*(d1^2+dp^2)*Ltr;
        %Volume of fluid in pipe and tubing combined, in^3
        Vpt=Vwater-Vtube_op;
    elseif Ltr<L1tT
        %Calculation of total amount of fluid in system, in^3
        Vwater=V_ref+pi/4*(d1^2+dp^2)*Ltr+0.5*pi/4*d1^2*LT;
        %Volume of fluid in pipe and tubing combined, in^3
        Vpt=Vwater-Vtube_op;
    else
        %Calculation of total amount of fluid in system, in^3
        Vwater=V_ref+pi/4*(d1^2+dp^2)*Ltr+pi/4*d1^2*LT;
        %Volume of fluid in pipe and tubing combined, in^3
        Vpt=Vwater-Vtube_op;
    end
else
    %Calculation of total amount of fluid in system, in^3
    Vwater=V_ref+pi/4*(d1^2*(L1+LT)+dt^2*(Ltr-L1)+dp^2*Ltr);
    %Volume of fluid in pipe and tubing combined, in^3
    Vpt=Vwater-Vtube_op;
end

V1=pi/4*(d1^2+dp^2)*L1bT;        %capacity of lower leg of tee, in^3
V2=pi/4*(d1^2*(LT+d1)+dp^2*d1);  %capacity of middle of tee, in^3
V3=pi/4*(d1^2+dp^2)*(L1-L1tT);   %capacity of upper leg of tee, in^3

if Vpt<(V1+V2+V3)
    if Vpt<V1
        h=Vpt/(pi/4*(d1^2+dp^2));
    elseif Vpt<(V1+V2)
        h=L1bT+d1/V2*(Vpt-V1);
    else
        h=L1tT+(Vpt-(V1+V2))/(pi/4*(d1^2+dp^2));
    end
else
    h=L1+(Vpt-(V1+V2+V3))/(pi/4*(dt^2+dp^2));
end
```

```matlab
%%%%%%%%%%%%%%%%%%%%%%%%%%%%%%%%%%%%%%%%%%%%%%%%%%%%%%%%%%%%%%%%%%%%%%%
%Frequency response

patm=14.7;                      %atmospheric pressure, psi

rho_ft=62.4;                    %density of water, lb/ft^3
rho_in=rho_ft/12^3;             %density of water, lb/in^3
rho=rho_in/(32.2*12);           %density of water, lb*s^2/in^4

M=(F_op)/(32.2*12);             %mass in motion, lb*s^2/in

R=0.01;                         %resistance to fluid flow, lb*s/in^5

f=[0:0.1:60];                   %frequency vector, Hz
w=2*pi*f;                       %frequency vector, rad/s
s=1i*w;                         %s=jw


%%%%%%%%%%%%%%%%%%%%%%%%%%%%%%%%%%%%%%%%%%%%%%%%%%%%%%%%%%%%%%%%%%%%%%%
%Find C3
lambda1_op=lambda1_op-lambda1_res;
V_tube_b=pi.*((0.1e1-lambda1_op.^2.*cos(alpha).^2).^(1/2) ...
    ./sin(alpha).*(Rio+Roo)./0.2e1-(Roo-Rio)./lambda1_op.*(0.1e1 ...
    -lambda1_op.^2.*cos(alpha).^2).^(-0.1e1./0.2e1).*sin(alpha) ...
    ./0.2e1).^2.*lambda1_op.*L;
lambda1_op=lambda1_op+2*lambda1_res;
V_tube_a=pi.*((0.1e1-lambda1_op.^2.*cos(alpha).^2).^(1/2) ...
    ./sin(alpha).*(Rio+Roo)./0.2e1-(Roo-Rio)./lambda1_op.*(0.1e1 ...
    -lambda1_op.^2.*cos(alpha).^2).^(-0.1e1./0.2e1).*sin(alpha) ...
    ./0.2e1).^2.*lambda1_op.*L;
A3=(V_tube_a-V_tube_b)/(2*lambda1_res);
C3=-A3/L;
%%%%%%%%%%%%%%%%%%%%%%%%%%%%%%%%%%%%%%%%%%%%%%%%%%%%%%%%%%%%%%%%%%%%%%%

lambda1_op=lambda1_op-lambda1_res; %reset lambda1_op to true lambda1_op

%%%%%%%%%%%%%%%%%%%%%%%%%%%%%%%%%%%%%%%%%%%%%%%%%%%%%%%%%%%%%%%%%%%%%%%
%Find C1
p=p_op;
lambda1=lambda1_op-lambda1_res;
Ftube_b=fsolve('exprII_dyn_II',20);
lambda1=lambda1_op+2*lambda1_res;
Ftube_a=fsolve('exprII_dyn_II',20);
A1=(Ftube_a-Ftube_b)/(2*lambda1_res);
C1=A1/L;
%%%%%%%%%%%%%%%%%%%%%%%%%%%%%%%%%%%%%%%%%%%%%%%%%%%%%%%%%%%%%%%%%%%%%%%

lambda1_op=lambda1_op-lambda1_res; %reset lambda1_op to true lambda1_op
```

```
%%%%%%%%%%%%%%%%%%%%%%%%%%%%%%%%%%%%%%%%%%%%%%%%%%%%%%%%%%%%%%%%%%%%%%%%%
%Find C2
lambda1=lambda1_op;
p=p_op-p_res;
Ftube_b=fsolve('exprII_dyn_II',20);
p=p_op+2*p_res;
Ftube_a=fsolve('exprII_dyn_II',20);
C2=(Ftube_a-Ftube_b)/(2*p_res);
%%%%%%%%%%%%%%%%%%%%%%%%%%%%%%%%%%%%%%%%%%%%%%%%%%%%%%%%%%%%%%%%%%%%%%%%%

p=p_op;                              %reset p

%%%%%%%%%%%%%%%%%%%%%%%%%%%%%%%%%%%%%%%%%%%%%%%%%%%%%%%%%%%%%%%%%%%%%%%%%
%Experiment Data

%Pressure test
load sixty_psi_two_in_water.lvm
load fifty_psi_two_and_three_fourths_in_water_II.lvm
load forty_psi_five_and_one_fourth_in_water_II.lvm
load thirty_psi_nine_and_three_fourths_in_water.lvm

fs=sixty_psi_two_in_water(:,1);
frfs=sixty_psi_two_in_water(:,2);

ff=fifty_psi_two_and_three_fourths_in_water_II(:,1);
frff=fifty_psi_two_and_three_fourths_in_water_II(:,2);

ffo=forty_psi_five_and_one_fourth_in_water_II(:,1);
frffo=forty_psi_five_and_one_fourth_in_water_II(:,2);

ft=thirty_psi_nine_and_three_fourths_in_water(:,1);
frft=thirty_psi_nine_and_three_fourths_in_water(:,2);
%%%%%%%%%%%%%%%%%%%%%%%%%%%%%%%%%%%%%%%%%%%%%%%%%%%%%%%%%%%%%%%%%%%%%%%%%

if h<L1
    %Capacitance, in^5/lb
    C=pi/4*(dct^2*Lct+dt^2*Lt+d1^2*(L1-h)+dp^2*(72-h))/(p_op+patm);
    %Inertance, lb*s^2/in^5
    I=4*rho*h/(pi*d1^2);
    %Area of port in contact with fluid, in^2
    AR=pi*d1*h;

    XoverF=1./((M+I*C2*C3)*s.^2+R*C2*C3*s+C1+C2*C3*(1/C));

    FtoverF=((a1-C2)*I*-C3*s.^2+((a1-C2)-AR)*R*-C3*s...
        +(a1-C2)*(1/C)*-C3+C1).*XoverF;
    H(:,i)=FtoverF;
else
    %Capacitance, in^5/lb
    C=pi/4*(dct^2*Lct+dt^2*(Lt-h+L1)+dp^2*(72-h))/(p_op+patm);
    %Inertance, lb*s^2/in^5
```

```matlab
    I=4*rho/pi*(L1/d1^2+(h-L1)/dt^2);
    %Area of port in contact with fluid, in^2
    AR=pi*(d1*L1+dt*(h-L1));

    XoverF=1./((M+I*C2*C3)*s.^2+R*C2*C3*s+C1+C2*C3*(1/C));

    FtoverF=((a1-C2)*I*-C3*s.^2+((a1-C2)-AR)*R*-C3*s...
        +(a1-C2)*(1/C)*-C3+C1).*XoverF;
    H(:,i)=FtoverF;
end

if i<2
    subplot(2,2,1)
    plot(f,20*log10(abs(H(:,1))),'-',ft,20*log10(0.4)+frft,...
        '--','LineWidth',1.5)
    axis([4 50 -60 30])
    set(gca,'FontSize',12,'FontName','Times New Roman')
    xlabel('\itf \rm(Hz)','FontSize',12,'FontName','Times New Roman')
    ylabel('|\itH\rm| (dB)','FontSize',12,'FontName','Times New Roman')
    gtext({'(a)'},'FontName','Times New Roman','Fontsize',12)
elseif i<3
    subplot(2,2,2)
    plot(f,20*log10(abs(H(:,2))),'-',ffo,20*log10(0.4)+frffo,...
        '--','LineWidth',1.5)
    axis([4 50 -60 30])
    set(gca,'FontSize',12,'FontName','Times New Roman')
    xlabel('\itf \rm(Hz)','FontSize',12,'FontName','Times New Roman')
    ylabel('|\itH\rm| (dB)','FontSize',12,'FontName','Times New Roman')
    gtext({'(b)'},'FontName','Times New Roman','Fontsize',12)
elseif i<4
    subplot(2,2,3)
    plot(f,20*log10(abs(H(:,3))),'-',ff,20*log10(0.4)+frff,...
        '--','LineWidth',1.5)
    axis([4 50 -60 30])
    set(gca,'FontSize',12,'FontName','Times New Roman')
    xlabel('\itf \rm(Hz)','FontSize',12,'FontName','Times New Roman')
    ylabel('|\itH\rm| (dB)','FontSize',12,'FontName','Times New Roman')
    gtext({'(c)'},'FontName','Times New Roman','Fontsize',12)
else
    subplot(2,2,4)
    plot(f,20*log10(abs(H(:,4))),'-',fs,20*log10(0.4)+frfs,...
        '--','LineWidth',1.5)
    axis([4 50 -60 30])
    set(gca,'FontSize',12,'FontName','Times New Roman')
    xlabel('\itf \rm(Hz)','FontSize',12,'FontName','Times New Roman')
    ylabel('|\itH\rm| (dB)','FontSize',12,'FontName','Times New Roman')
    gtext({'(d)'},'FontName','Times New Roman','Fontsize',12)
end

end
```

A.2   Function exprII_dyn_I

```matlab
%Lloyd Scarborough
%Created April 12, 2010
%Last modified November 14, 2013
%Function to be solved numerically by F2MC_isolator_pressure_plots.m

function Fo=exprII_dyn_I(lambda1_op)
global p alpha Rio Roo Er Ep ds Ls nu rf delta m F L

Fo=-p.*pi.*L.*(0.2e1.*(sqrt(0.1e1-lambda1_op.^2.*cos(alpha).^2) ...
./sin(alpha).*(Rio+Roo)./0.2e1-(Roo-Rio)./lambda1_op ...
.*(0.1e1-lambda1_op.^2.*cos(alpha).^2).^(-0.1e1./0.2e1) ...
.*sin(alpha)./0.2e1).*lambda1_op.*(-(0.1e1-lambda1_op.^2 ...
.*cos(alpha).^2).^(-0.1e1./0.2e1)./sin(alpha).*(Rio+Roo) ...
.*lambda1_op.*cos(alpha).^2./0.2e1+(Roo-Rio)./lambda1_op.^2 ...
.*(0.1e1-lambda1_op.^2.*cos(alpha).^2).^(-0.1e1./0.2e1) ...
.*sin(alpha)./0.2e1-(Roo-Rio).*(0.1e1-lambda1_op.^2 ...
.*cos(alpha).^2).^(-0.3e1./0.2e1).*sin(alpha).*cos(alpha).^2 ...
./0.2e1)+(sqrt(0.1e1-lambda1_op.^2.*cos(alpha).^2)./sin(alpha) ...
.*(Rio+Roo)./0.2e1-(Roo-Rio)./lambda1_op.*(0.1e1-lambda1_op.^2 ...
.*cos(alpha).^2).^(-0.1e1./0.2e1).*sin(alpha)./0.2e1).^2)-F.*L+Er ...
.*(0.2e1.*lambda1_op-0.2e1.*lambda1_op.*cos(alpha).^2 ...
./sin(alpha).^2-0.2e1./lambda1_op.^3./(0.1e1-lambda1_op.^2 ...
.*cos(alpha).^2).*sin(alpha).^2+0.2e1./lambda1_op ...
./(0.1e1-lambda1_op.^2.*cos(alpha).^2).^2.*sin(alpha).^2 ...
.*cos(alpha).^2).*pi.*L.*(Roo.^2-Rio.^2)./0.6e1+0.4e1.*m.*(Er ...
.*(lambda1_op-0.1e1)+nu.*p.*(sqrt(0.1e1-lambda1_op.^2 ...
.*cos(alpha).^2)./sin(alpha).*(Rio+Roo)./0.2e1-(Roo-Rio) ...
./lambda1_op.*(0.1e1-lambda1_op.^2.*cos(alpha).^2).^(-0.1e1 ...
./0.2e1).*sin(alpha)./0.2e1)./(Roo-Rio).*lambda1_op ...
.*sqrt(0.1e1-lambda1_op.^2.*cos(alpha).^2)./sin(alpha)-(pi.*p ...
.*(sqrt(0.1e1-lambda1_op.^2.*cos(alpha).^2)./sin(alpha).*(Rio+Roo) ...
./0.2e1-(Roo-Rio)./lambda1_op.*(0.1e1-lambda1_op.^2 ...
.*cos(alpha).^2).^(-0.1e1./0.2e1).*sin(alpha)./0.2e1).^2+F)./pi ...
./((sqrt(0.1e1-lambda1_op.^2.*cos(alpha).^2)./sin(alpha).*(Rio ...
+Roo)./0.2e1+(Roo-Rio)./lambda1_op.*(0.1e1-lambda1_op.^2 ...
.*cos(alpha).^2).^(-0.1e1./0.2e1).*sin(alpha) ...
./0.2e1).^2-(sqrt(0.1e1-lambda1_op.^2.*cos(alpha).^2)./sin(alpha) ...
.*(Rio+Roo)./0.2e1-(Roo-Rio)./lambda1_op.*(0.1e1-lambda1_op.^2 ...
.*cos(alpha).^2).^(-0.1e1./0.2e1).*sin(alpha)./0.2e1).^2)).*(0.1e1 ...
+(sqrt(0.1e1-lambda1_op.^2.*cos(alpha).^2)./sin(alpha).*(Rio+Roo) ...
./0.2e1+(Roo-Rio)./lambda1_op.*(0.1e1-lambda1_op.^2 ...
.*cos(alpha).^2).^(-0.1e1./0.2e1).*sin(alpha)./0.2e1-rf).^2 ...
./delta.^2)./(nu.*m.*tan(alpha).*(0.1e1-lambda1_op.^2 ...
.*cos(alpha).^2)./(Roo-Rio)./sin(alpha)./pi./Roo./0.2e1-m ...
.*lambda1_op.*cos(alpha)./pi./((sqrt(0.1e1-lambda1_op.^2 ...
.*cos(alpha).^2)./sin(alpha).*(Rio+Roo)./0.2e1+(Roo-Rio) ...
./lambda1_op.*(0.1e1-lambda1_op.^2.*cos(alpha).^2).^(-0.1e1 ...
```

```
./0.2e1).*sin(alpha)./0.2e1).^2-(sqrt(0.1e1-lambda1_op.^2 ...
.*cos(alpha).^2)./sin(alpha).*(Rio+Roo)./0.2e1-(Roo-Rio) ...
./lambda1_op.*(0.1e1-lambda1_op.^2.*cos(alpha).^2).^(-0.1e1 ...
./0.2e1).*sin(alpha)./0.2e1).^2)).^2.*L./cos(alpha)./Ep./pi./ds.^2 ...
.*(Er+nu.*p.*(-(0.1e1-lambda1_op.^2.*cos(alpha).^2).^(-0.1e1 ...
./0.2e1)./sin(alpha).*(Rio+Roo).*lambda1_op.*cos(alpha).^2./0.2e1 ...
+(Roo-Rio)./lambda1_op.^2.*(0.1e1-lambda1_op.^2 ...
.*cos(alpha).^2).^(-0.1e1./0.2e1).*sin(alpha)./0.2e1-(Roo-Rio) ...
.*(0.1e1-lambda1_op.^2.*cos(alpha).^2).^(-0.3e1./0.2e1) ...
.*sin(alpha).*cos(alpha).^2./0.2e1)./(Roo-Rio).*lambda1_op ...
.*sqrt(0.1e1-lambda1_op.^2.*cos(alpha).^2)./sin(alpha)+nu.*p ...
.*(sqrt(0.1e1-lambda1_op.^2.*cos(alpha).^2)./sin(alpha).*(Rio+Roo) ...
./0.2e1-(Roo-Rio)./lambda1_op.*(0.1e1-lambda1_op.^2 ...
.*cos(alpha).^2).^(-0.1e1./0.2e1).*sin(alpha)./0.2e1)./(Roo-Rio) ...
.*sqrt(0.1e1-lambda1_op.^2.*cos(alpha).^2)./sin(alpha)-nu.*p ...
.*(sqrt(0.1e1-lambda1_op.^2.*cos(alpha).^2)./sin(alpha).*(Rio+Roo) ...
./0.2e1-(Roo-Rio)./lambda1_op.*(0.1e1-lambda1_op.^2 ...
.*cos(alpha).^2).^(-0.1e1./0.2e1).*sin(alpha)./0.2e1)./(Roo-Rio) ...
.*lambda1_op.^2.*(0.1e1-lambda1_op.^2.*cos(alpha).^2).^(-0.1e1 ...
./0.2e1)./sin(alpha).*cos(alpha).^2-0.2e1.*p ...
.*(sqrt(0.1e1-lambda1_op.^2.*cos(alpha).^2)./sin(alpha).*(Rio+Roo) ...
./0.2e1-(Roo-Rio)./lambda1_op.*(0.1e1-lambda1_op.^2 ...
.*cos(alpha).^2).^(-0.1e1./0.2e1).*sin(alpha)./0.2e1) ...
.*(-(0.1e1-lambda1_op.^2.*cos(alpha).^2).^(-0.1e1./0.2e1) ...
./sin(alpha).*(Rio+Roo).*lambda1_op.*cos(alpha).^2./0.2e1 ...
+(Roo-Rio)./lambda1_op.^2.*(0.1e1-lambda1_op.^2 ...
.*cos(alpha).^2).^(-0.1e1./0.2e1).*sin(alpha)./0.2e1-(Roo-Rio) ...
.*(0.1e1-lambda1_op.^2.*cos(alpha).^2).^(-0.3e1./0.2e1) ...
.*sin(alpha).*cos(alpha).^2./0.2e1)./((sqrt(0.1e1-lambda1_op.^2 ...
.*cos(alpha).^2)./sin(alpha).*(Rio+Roo)./0.2e1+(Roo-Rio) ...
./lambda1_op.*(0.1e1-lambda1_op.^2.*cos(alpha).^2).^(-0.1e1 ...
./0.2e1).*sin(alpha)./0.2e1).^2-(sqrt(0.1e1-lambda1_op.^2 ...
.*cos(alpha).^2)./sin(alpha).*(Rio+Roo)./0.2e1-(Roo-Rio) ...
./lambda1_op.*(0.1e1-lambda1_op.^2.*cos(alpha).^2).^(-0.1e1 ...
./0.2e1).*sin(alpha)./0.2e1).^2)+(pi.*p.*(sqrt(0.1e1-lambda1_op.^2 ...
.*cos(alpha).^2)./sin(alpha).*(Rio+Roo)./0.2e1-(Roo-Rio) ...
./lambda1_op.*(0.1e1-lambda1_op.^2.*cos(alpha).^2).^(-0.1e1 ...
./0.2e1).*sin(alpha)./0.2e1).^2+F)./pi./((sqrt(0.1e1-lambda1_op.^2 ...
.*cos(alpha).^2)./sin(alpha).*(Rio+Roo)./0.2e1+(Roo-Rio) ...
./lambda1_op.*(0.1e1-lambda1_op.^2.*cos(alpha).^2).^(-0.1e1 ...
./0.2e1).*sin(alpha)./0.2e1).^2-(sqrt(0.1e1-lambda1_op.^2 ...
.*cos(alpha).^2)./sin(alpha).*(Rio+Roo)./0.2e1-(Roo-Rio) ...
./lambda1_op.*(0.1e1-lambda1_op.^2.*cos(alpha).^2).^(-0.1e1 ...
./0.2e1).*sin(alpha)./0.2e1).^2).^2.*(0.2e1 ...
.*(sqrt(0.1e1-lambda1_op.^2.*cos(alpha).^2)./sin(alpha).*(Rio+Roo) ...
./0.2e1+(Roo-Rio)./lambda1_op.*(0.1e1-lambda1_op.^2 ...
.*cos(alpha).^2).^(-0.1e1./0.2e1).*sin(alpha)./0.2e1) ...
.*(-(0.1e1-lambda1_op.^2.*cos(alpha).^2).^(-0.1e1./0.2e1) ...
./sin(alpha).*(Rio+Roo).*lambda1_op.*cos(alpha).^2 ...
./0.2e1-(Roo-Rio)./lambda1_op.^2.*(0.1e1-lambda1_op.^2 ...
.*cos(alpha).^2).^(-0.1e1./0.2e1).*sin(alpha)./0.2e1+(Roo-Rio) ...
```

```
.*(0.1e1-lambda1_op.^2.*cos(alpha).^2).^(-0.3e1./0.2e1) ...
.*sin(alpha).*cos(alpha).^2./0.2e1)-0.2e1 ...
.*(sqrt(0.1e1-lambda1_op.^2.*cos(alpha).^2)./sin(alpha).*(Rio+Roo) ...
./0.2e1-(Roo-Rio)./lambda1_op.*(0.1e1-lambda1_op.^2 ...
.*cos(alpha).^2).^(-0.1e1./0.2e1).*sin(alpha)./0.2e1) ...
.*(-(0.1e1-lambda1_op.^2.*cos(alpha).^2).^(-0.1e1./0.2e1) ...
./sin(alpha).*(Rio+Roo).*lambda1_op.*cos(alpha).^2./0.2e1 ...
+(Roo-Rio)./lambda1_op.^2.*(0.1e1-lambda1_op.^2 ...
.*cos(alpha).^2).^(-0.1e1./0.2e1).*sin(alpha)./0.2e1-(Roo-Rio) ...
.*(0.1e1-lambda1_op.^2.*cos(alpha).^2).^(-0.3e1./0.2e1) ...
.*sin(alpha).*cos(alpha).^2./0.2e1)))+0.4e1.*m.*(Er ...
.*(lambda1_op-0.1e1)+nu.*p.*(sqrt(0.1e1-lambda1_op.^2 ...
.*cos(alpha).^2)./sin(alpha).*(Rio+Roo)./0.2e1-(Roo-Rio) ...
./lambda1_op.*(0.1e1-lambda1_op.^2.*cos(alpha).^2).^(-0.1e1 ...
./0.2e1).*sin(alpha)./0.2e1)./(Roo-Rio).*lambda1_op ...
.*sqrt(0.1e1-lambda1_op.^2.*cos(alpha).^2)./sin(alpha)-(pi.*p ...
.*(sqrt(0.1e1-lambda1_op.^2.*cos(alpha).^2)./sin(alpha).*(Rio+Roo) ...
./0.2e1-(Roo-Rio)./lambda1_op.*(0.1e1-lambda1_op.^2 ...
.*cos(alpha).^2).^(-0.1e1./0.2e1).*sin(alpha)./0.2e1).^2+F)./pi ...
./((sqrt(0.1e1-lambda1_op.^2.*cos(alpha).^2)./sin(alpha).*(Rio ...
+Roo)./0.2e1+(Roo-Rio)./lambda1_op.*(0.1e1-lambda1_op.^2 ...
.*cos(alpha).^2).^(-0.1e1./0.2e1).*sin(alpha) ...
./0.2e1).^2-(sqrt(0.1e1-lambda1_op.^2.*cos(alpha).^2)./sin(alpha) ...
.*(Rio+Roo)./0.2e1-(Roo-Rio)./lambda1_op.*(0.1e1-lambda1_op.^2 ...
.*cos(alpha).^2).^(-0.1e1./0.2e1).*sin(alpha)./0.2e1).^2)).^2 ...
.*(sqrt(0.1e1-lambda1_op.^2.*cos(alpha).^2)./sin(alpha).*(Rio+Roo) ...
./0.2e1+(Roo-Rio)./lambda1_op.*(0.1e1-lambda1_op.^2 ...
.*cos(alpha).^2).^(-0.1e1./0.2e1).*sin(alpha)./0.2e1-rf)./delta.^2 ...
.*(-(0.1e1-lambda1_op.^2.*cos(alpha).^2).^(-0.1e1./0.2e1) ...
./sin(alpha).*(Rio+Roo).*lambda1_op.*cos(alpha).^2 ...
./0.2e1-(Roo-Rio)./lambda1_op.^2.*(0.1e1-lambda1_op.^2 ...
.*cos(alpha).^2).^(-0.1e1./0.2e1).*sin(alpha)./0.2e1+(Roo-Rio) ...
.*(0.1e1-lambda1_op.^2.*cos(alpha).^2).^(-0.3e1./0.2e1) ...
.*sin(alpha).*cos(alpha).^2./0.2e1)./(nu.*m.*tan(alpha) ...
.*(0.1e1-lambda1_op.^2.*cos(alpha).^2)./(Roo-Rio)./sin(alpha)./pi ...
./Roo./0.2e1-m.*lambda1_op.*cos(alpha)./pi ...
./((sqrt(0.1e1-lambda1_op.^2.*cos(alpha).^2)./sin(alpha).*(Rio ...
+Roo)./0.2e1+(Roo-Rio)./lambda1_op.*(0.1e1-lambda1_op.^2 ...
.*cos(alpha).^2).^(-0.1e1./0.2e1).*sin(alpha) ...
./0.2e1).^2-(sqrt(0.1e1-lambda1_op.^2.*cos(alpha).^2)./sin(alpha) ...
.*(Rio+Roo)./0.2e1-(Roo-Rio)./lambda1_op.*(0.1e1-lambda1_op.^2 ...
.*cos(alpha).^2).^(-0.1e1./0.2e1).*sin(alpha)./0.2e1).^2)).^2.*L ...
./cos(alpha)./Ep./pi./ds.^2-0.4e1.*m.*(Er.*(lambda1_op-0.1e1)+nu ...
.*p.*(sqrt(0.1e1-lambda1_op.^2.*cos(alpha).^2)./sin(alpha).*(Rio ...
+Roo)./0.2e1-(Roo-Rio)./lambda1_op.*(0.1e1-lambda1_op.^2 ...
.*cos(alpha).^2).^(-0.1e1./0.2e1).*sin(alpha)./0.2e1)./(Roo-Rio) ...
.*lambda1_op.*sqrt(0.1e1-lambda1_op.^2.*cos(alpha).^2) ...
./sin(alpha)-(pi.*p.*(sqrt(0.1e1-lambda1_op.^2.*cos(alpha).^2) ...
./sin(alpha).*(Rio+Roo)./0.2e1-(Roo-Rio)./lambda1_op ...
.*(0.1e1-lambda1_op.^2.*cos(alpha).^2).^(-0.1e1./0.2e1) ...
.*sin(alpha)./0.2e1).^2+F)./pi./((sqrt(0.1e1-lambda1_op.^2 ...
```

```
.*cos(alpha).^2)./sin(alpha).*(Rio+Roo)./0.2e1+(Roo-Rio) ...
./lambda1_op.*(0.1e1-lambda1_op.^2.*cos(alpha).^2).^(-0.1e1 ...
./0.2e1).*sin(alpha)./0.2e1).^2-(sqrt(0.1e1-lambda1_op.^2 ...
.*cos(alpha).^2)./sin(alpha).*(Rio+Roo)./0.2e1-(Roo-Rio) ...
./lambda1_op.*(0.1e1-lambda1_op.^2.*cos(alpha).^2).^(-0.1e1 ...
./0.2e1).*sin(alpha)./0.2e1).^2)).^2.*(0.1e1 ...
+(sqrt(0.1e1-lambda1_op.^2.*cos(alpha).^2)./sin(alpha).*(Rio+Roo) ...
./0.2e1+(Roo-Rio)./lambda1_op.*(0.1e1-lambda1_op.^2 ...
.*cos(alpha).^2).^(-0.1e1./0.2e1).*sin(alpha)./0.2e1-rf).^2 ...
./delta.^2)./(nu.*m.*tan(alpha).*(0.1e1-lambda1_op.^2 ...
.*cos(alpha).^2)./(Roo-Rio)./sin(alpha)./pi./Roo./0.2e1-m ...
.*lambda1_op.*cos(alpha)./pi./((sqrt(0.1e1-lambda1_op.^2 ...
.*cos(alpha).^2)./sin(alpha).*(Rio+Roo)./0.2e1+(Roo-Rio) ...
./lambda1_op.*(0.1e1-lambda1_op.^2.*cos(alpha).^2).^(-0.1e1 ...
./0.2e1).*sin(alpha)./0.2e1).^2-(sqrt(0.1e1-lambda1_op.^2 ...
.*cos(alpha).^2)./sin(alpha).*(Rio+Roo)./0.2e1-(Roo-Rio) ...
./lambda1_op.*(0.1e1-lambda1_op.^2.*cos(alpha).^2).^(-0.1e1 ...
./0.2e1).*sin(alpha)./0.2e1).^2)).^3.*L./cos(alpha)./Ep./pi./ds.^2 ...
.*(-nu.*m.*tan(alpha).*lambda1_op.*cos(alpha).^2./(Roo-Rio) ...
./sin(alpha)./pi./Roo-m.*cos(alpha)./pi ...
./((sqrt(0.1e1-lambda1_op.^2.*cos(alpha).^2)./sin(alpha).*(Rio ...
+Roo)./0.2e1+(Roo-Rio)./lambda1_op.*(0.1e1-lambda1_op.^2 ...
.*cos(alpha).^2).^(-0.1e1./0.2e1).*sin(alpha) ...
./0.2e1).^2-(sqrt(0.1e1-lambda1_op.^2.*cos(alpha).^2)./sin(alpha) ...
.*(Rio+Roo)./0.2e1-(Roo-Rio)./lambda1_op.*(0.1e1-lambda1_op.^2 ...
.*cos(alpha).^2).^(-0.1e1./0.2e1).*sin(alpha)./0.2e1).^2)+m ...
.*lambda1_op.*cos(alpha)./pi./((sqrt(0.1e1-lambda1_op.^2 ...
.*cos(alpha).^2)./sin(alpha).*(Rio+Roo)./0.2e1+(Roo-Rio) ...
./lambda1_op.*(0.1e1-lambda1_op.^2.*cos(alpha).^2).^(-0.1e1 ...
./0.2e1).*sin(alpha)./0.2e1).^2-(sqrt(0.1e1-lambda1_op.^2 ...
.*cos(alpha).^2)./sin(alpha).*(Rio+Roo)./0.2e1-(Roo-Rio) ...
./lambda1_op.*(0.1e1-lambda1_op.^2.*cos(alpha).^2).^(-0.1e1 ...
./0.2e1).*sin(alpha)./0.2e1).^2).^2.*(0.2e1 ...
.*(sqrt(0.1e1-lambda1_op.^2.*cos(alpha).^2)./sin(alpha).*(Rio+Roo) ...
./0.2e1+(Roo-Rio)./lambda1_op.*(0.1e1-lambda1_op.^2 ...
.*cos(alpha).^2).^(-0.1e1./0.2e1).*sin(alpha)./0.2e1) ...
.*(-(0.1e1-lambda1_op.^2.*cos(alpha).^2).^(-0.1e1./0.2e1) ...
./sin(alpha).*(Rio+Roo).*lambda1_op.*cos(alpha).^2 ...
./0.2e1-(Roo-Rio)./lambda1_op.^2.*(0.1e1-lambda1_op.^2 ...
.*cos(alpha).^2).^(-0.1e1./0.2e1).*sin(alpha)./0.2e1+(Roo-Rio) ...
.*(0.1e1-lambda1_op.^2.*cos(alpha).^2).^(-0.3e1./0.2e1) ...
.*sin(alpha).*cos(alpha).^2./0.2e1)-0.2e1 ...
.*(sqrt(0.1e1-lambda1_op.^2.*cos(alpha).^2)./sin(alpha).*(Rio+Roo) ...
./0.2e1-(Roo-Rio)./lambda1_op.*(0.1e1-lambda1_op.^2 ...
.*cos(alpha).^2).^(-0.1e1./0.2e1).*sin(alpha)./0.2e1) ...
.*(-(0.1e1-lambda1_op.^2.*cos(alpha).^2).^(-0.1e1./0.2e1) ...
./sin(alpha).*(Rio+Roo).*lambda1_op.*cos(alpha).^2./0.2e1 ...
+(Roo-Rio)./lambda1_op.^2.*(0.1e1-lambda1_op.^2 ...
.*cos(alpha).^2).^(-0.1e1./0.2e1).*sin(alpha)./0.2e1-(Roo-Rio) ...
.*(0.1e1-lambda1_op.^2.*cos(alpha).^2).^(-0.3e1./0.2e1) ...
.*sin(alpha).*cos(alpha).^2./0.2e1)));
```

A.3   Function exprII_dyn_II

```
%Lloyd Scarborough
%Created April 2, 2010
%Last modified November 14, 2013
%Function to be solved numerically by F2MC_isolator_pressure_plots.m

function Fo=exprII_dyn_II(Ftube)
global p alpha Rio Roo Er Ep ds Ls nu rf delta m L lambda1

Fo=-p.*pi.*L.*(0.2e1.*(sqrt(0.1e1-lambda1.^2.*cos(alpha).^2) ...
./sin(alpha).*(Rio+Roo)./0.2e1-(Roo-Rio)./lambda1 ...
.*(0.1e1-lambda1.^2.*cos(alpha).^2).^(-0.1e1./0.2e1).*sin(alpha) ...
./0.2e1).*lambda1.*(-(0.1e1-lambda1.^2.*cos(alpha).^2).^(-0.1e1 ...
./0.2e1)./sin(alpha).*(Rio+Roo).*lambda1.*cos(alpha).^2./0.2e1 ...
+(Roo-Rio)./lambda1.^2.*(0.1e1-lambda1.^2 ...
.*cos(alpha).^2).^(-0.1e1./0.2e1).*sin(alpha)./0.2e1-(Roo-Rio) ...
.*(0.1e1-lambda1.^2.*cos(alpha).^2).^(-0.3e1./0.2e1).*sin(alpha) ...
.*cos(alpha).^2./0.2e1)+(sqrt(0.1e1-lambda1.^2.*cos(alpha).^2) ...
./sin(alpha).*(Rio+Roo)./0.2e1-(Roo-Rio)./lambda1 ...
.*(0.1e1-lambda1.^2.*cos(alpha).^2).^(-0.1e1./0.2e1).*sin(alpha) ...
./0.2e1).^2)-Ftube.*L ...
+Er.*(0.2e1.*lambda1-0.2e1.*lambda1 ...
.*cos(alpha).^2./sin(alpha).^2-0.2e1./lambda1.^3 ...
./(0.1e1-lambda1.^2.*cos(alpha).^2).*sin(alpha).^2+0.2e1./lambda1 ...
./(0.1e1-lambda1.^2.*cos(alpha).^2).^2.*sin(alpha).^2 ...
.*cos(alpha).^2).*pi.*L.*(Roo.^2-Rio.^2)./0.6e1+0.4e1.*m.*(Er ...
.*(lambda1-0.1e1)+nu.*p.*(sqrt(0.1e1-lambda1.^2.*cos(alpha).^2) ...
./sin(alpha).*(Rio+Roo)./0.2e1-(Roo-Rio)./lambda1 ...
.*(0.1e1-lambda1.^2.*cos(alpha).^2).^(-0.1e1./0.2e1).*sin(alpha) ...
./0.2e1)./(Roo-Rio).*lambda1.*sqrt(0.1e1-lambda1.^2 ...
.*cos(alpha).^2)./sin(alpha)-(pi.*p.*(sqrt(0.1e1-lambda1.^2 ...
.*cos(alpha).^2)./sin(alpha).*(Rio+Roo)./0.2e1-(Roo-Rio)./lambda1 ...
.*(0.1e1-lambda1.^2.*cos(alpha).^2).^(-0.1e1./0.2e1).*sin(alpha) ...
./0.2e1).^2+Ftube)./pi./((sqrt(0.1e1-lambda1.^2.*cos(alpha).^2) ...
./sin(alpha).*(Rio+Roo)./0.2e1+(Roo-Rio)./lambda1 ...
.*(0.1e1-lambda1.^2.*cos(alpha).^2).^(-0.1e1./0.2e1).*sin(alpha) ...
./0.2e1).^2-(sqrt(0.1e1-lambda1.^2.*cos(alpha).^2)./sin(alpha) ...
.*(Rio+Roo)./0.2e1-(Roo-Rio)./lambda1.*(0.1e1-lambda1.^2 ...
.*cos(alpha).^2).^(-0.1e1./0.2e1).*sin(alpha)./0.2e1).^2)).*(0.1e1 ...
+(sqrt(0.1e1-lambda1.^2.*cos(alpha).^2)./sin(alpha).*(Rio+Roo) ...
./0.2e1+(Roo-Rio)./lambda1.*(0.1e1-lambda1.^2 ...
.*cos(alpha).^2).^(-0.1e1./0.2e1).*sin(alpha)./0.2e1-rf).^2 ...
./delta.^2)./(nu.*m.*tan(alpha).*(0.1e1-lambda1.^2.*cos(alpha).^2) ...
./(Roo-Rio)./sin(alpha)./pi./Roo./0.2e1-m.*lambda1.*cos(alpha)./pi ...
./((sqrt(0.1e1-lambda1.^2.*cos(alpha).^2)./sin(alpha).*(Rio+Roo) ...
./0.2e1+(Roo-Rio)./lambda1.*(0.1e1-lambda1.^2 ...
.*cos(alpha).^2).^(-0.1e1./0.2e1).*sin(alpha) ...
./0.2e1).^2-(sqrt(0.1e1-lambda1.^2.*cos(alpha).^2)./sin(alpha) ...
```

```
.*(Rio+Roo)./0.2e1—(Roo—Rio)./lambda1.*(0.1e1—lambda1.^2 ...
.*cos(alpha).^2).^(—0.1e1./0.2e1).*sin(alpha)./0.2e1).^2)).^2.*L ...
./cos(alpha)./Ep./pi./ds.^2.*(Er+nu.*p.*(—(0.1e1—lambda1.^2 ...
.*cos(alpha).^2).^(—0.1e1./0.2e1)./sin(alpha).*(Rio+Roo).*lambda1 ...
.*cos(alpha).^2./0.2e1+(Roo—Rio)./lambda1.^2.*(0.1e1—lambda1.^2 ...
.*cos(alpha).^2).^(—0.1e1./0.2e1).*sin(alpha)./0.2e1—(Roo—Rio) ...
.*(0.1e1—lambda1.^2.*cos(alpha).^2).^(—0.3e1./0.2e1).*sin(alpha) ...
.*cos(alpha).^2./0.2e1)./(Roo—Rio).*lambda1.*sqrt(0.1e1—lambda1.^2 ...
.*cos(alpha).^2)./sin(alpha)+nu.*p.*(sqrt(0.1e1—lambda1.^2 ...
.*cos(alpha).^2)./sin(alpha).*(Rio+Roo)./0.2e1—(Roo—Rio)./lambda1 ...
.*(0.1e1—lambda1.^2.*cos(alpha).^2).^(—0.1e1./0.2e1).*sin(alpha) ...
./0.2e1)./(Roo—Rio).*sqrt(0.1e1—lambda1.^2.*cos(alpha).^2) ...
./sin(alpha)—nu.*p.*(sqrt(0.1e1—lambda1.^2.*cos(alpha).^2) ...
./sin(alpha).*(Rio+Roo)./0.2e1—(Roo—Rio)./lambda1 ...
.*(0.1e1—lambda1.^2.*cos(alpha).^2).^(—0.1e1./0.2e1).*sin(alpha) ...
./0.2e1)./(Roo—Rio)./lambda1.^2.*(0.1e1—lambda1.^2 ...
.*cos(alpha).^2).^(—0.1e1./0.2e1)./sin(alpha).*cos(alpha).^2—0.2e1 ...
.*p.*(sqrt(0.1e1—lambda1.^2.*cos(alpha).^2)./sin(alpha).*(Rio+Roo) ...
./0.2e1—(Roo—Rio)./lambda1.*(0.1e1—lambda1.^2 ...
.*cos(alpha).^2).^(—0.1e1./0.2e1).*sin(alpha)./0.2e1) ...
.*(—(0.1e1—lambda1.^2.*cos(alpha).^2).^(—0.1e1./0.2e1)./sin(alpha) ...
.*(Rio+Roo).*lambda1.*cos(alpha).^2./0.2e1+(Roo—Rio)./lambda1.^2 ...
.*(0.1e1—lambda1.^2.*cos(alpha).^2).^(—0.1e1./0.2e1).*sin(alpha) ...
./0.2e1—(Roo—Rio).*(0.1e1—lambda1.^2.*cos(alpha).^2).^(—0.3e1 ...
./0.2e1).*sin(alpha).*cos(alpha).^2./0.2e1) ...
./((sqrt(0.1e1—lambda1.^2.*cos(alpha).^2)./sin(alpha).*(Rio+Roo) ...
./0.2e1+(Roo—Rio)./lambda1.*(0.1e1—lambda1.^2 ...
.*cos(alpha).^2).^(—0.1e1./0.2e1).*sin(alpha) ...
./0.2e1).^2—(sqrt(0.1e1—lambda1.^2.*cos(alpha).^2)./sin(alpha) ...
.*(Rio+Roo)./0.2e1—(Roo—Rio)./lambda1.*(0.1e1—lambda1.^2 ...
.*cos(alpha).^2).^(—0.1e1./0.2e1).*sin(alpha)./0.2e1).^2)+(pi.*p ...
.*(sqrt(0.1e1—lambda1.^2.*cos(alpha).^2)./sin(alpha).*(Rio+Roo) ...
./0.2e1—(Roo—Rio)./lambda1.*(0.1e1—lambda1.^2 ...
.*cos(alpha).^2).^(—0.1e1./0.2e1).*sin(alpha)./0.2e1).^2+Ftube) ...
./pi./((sqrt(0.1e1—lambda1.^2.*cos(alpha).^2)./sin(alpha).*(Rio ...
+Roo)./0.2e1+(Roo—Rio)./lambda1.*(0.1e1—lambda1.^2 ...
.*cos(alpha).^2).^(—0.1e1./0.2e1).*sin(alpha) ...
./0.2e1).^2—(sqrt(0.1e1—lambda1.^2.*cos(alpha).^2)./sin(alpha) ...
.*(Rio+Roo)./0.2e1—(Roo—Rio)./lambda1.*(0.1e1—lambda1.^2 ...
.*cos(alpha).^2).^(—0.1e1./0.2e1).*sin(alpha)./0.2e1).^2).^2 ...
.*(0.2e1.*(sqrt(0.1e1—lambda1.^2.*cos(alpha).^2)./sin(alpha).*(Rio ...
+Roo)./0.2e1+(Roo—Rio)./lambda1.*(0.1e1—lambda1.^2 ...
.*cos(alpha).^2).^(—0.1e1./0.2e1).*sin(alpha)./0.2e1) ...
.*(—(0.1e1—lambda1.^2.*cos(alpha).^2).^(—0.1e1./0.2e1)./sin(alpha) ...
.*(Rio+Roo).*lambda1.*cos(alpha).^2./0.2e1—(Roo—Rio)./lambda1.^2 ...
.*(0.1e1—lambda1.^2.*cos(alpha).^2).^(—0.1e1./0.2e1).*sin(alpha) ...
./0.2e1+(Roo—Rio).*(0.1e1—lambda1.^2.*cos(alpha).^2).^(—0.3e1 ...
./0.2e1).*sin(alpha).*cos(alpha).^2./0.2e1)—0.2e1 ...
.*(sqrt(0.1e1—lambda1.^2.*cos(alpha).^2)./sin(alpha).*(Rio+Roo) ...
./0.2e1—(Roo—Rio)./lambda1.*(0.1e1—lambda1.^2 ...
.*cos(alpha).^2).^(—0.1e1./0.2e1).*sin(alpha)./0.2e1) ...
```

```
.*(-(0.1e1-lambda1.^2.*cos(alpha).^2).^(-0.1e1./0.2e1)./sin(alpha) ...
.*(Rio+Roo).*lambda1.*cos(alpha).^2./0.2e1+(Roo-Rio)./lambda1.^2 ...
.*(0.1e1-lambda1.^2.*cos(alpha).^2).^(-0.1e1./0.2e1).*sin(alpha) ...
./0.2e1-(Roo-Rio).*(0.1e1-lambda1.^2.*cos(alpha).^2).^(-0.3e1 ...
./0.2e1).*sin(alpha).*cos(alpha).^2./0.2e1)))+0.4e1.*m.*(Er ...
.*(lambda1-0.1e1)+nu.*p.*(sqrt(0.1e1-lambda1.^2.*cos(alpha).^2) ...
./sin(alpha).*(Rio+Roo)./0.2e1-(Roo-Rio)./lambda1 ...
.*(0.1e1-lambda1.^2.*cos(alpha).^2).^(-0.1e1./0.2e1).*sin(alpha) ...
./0.2e1)./(Roo-Rio).*lambda1.*sqrt(0.1e1-lambda1.^2 ...
.*cos(alpha).^2)./sin(alpha)-(pi.*p.*(sqrt(0.1e1-lambda1.^2 ...
.*cos(alpha).^2)./sin(alpha).*(Rio+Roo)./0.2e1-(Roo-Rio)./lambda1 ...
.*(0.1e1-lambda1.^2.*cos(alpha).^2).^(-0.1e1./0.2e1).*sin(alpha) ...
./0.2e1).^2+Ftube)./pi./((sqrt(0.1e1-lambda1.^2.*cos(alpha).^2) ...
./sin(alpha).*(Rio+Roo)./0.2e1+(Roo-Rio)./lambda1 ...
.*(0.1e1-lambda1.^2.*cos(alpha).^2).^(-0.1e1./0.2e1).*sin(alpha) ...
./0.2e1).^2-(sqrt(0.1e1-lambda1.^2.*cos(alpha).^2)./sin(alpha) ...
.*(Rio+Roo)./0.2e1-(Roo-Rio)./lambda1.*(0.1e1-lambda1.^2 ...
.*cos(alpha).^2).^(-0.1e1./0.2e1).*sin(alpha)./0.2e1).^2)).^2 ...
.*(sqrt(0.1e1-lambda1.^2.*cos(alpha).^2)./sin(alpha).*(Rio+Roo) ...
./0.2e1+(Roo-Rio)./lambda1.*(0.1e1-lambda1.^2 ...
.*cos(alpha).^2).^(-0.1e1./0.2e1).*sin(alpha)./0.2e1-rf)./delta.^2 ...
.*(-(0.1e1-lambda1.^2.*cos(alpha).^2).^(-0.1e1./0.2e1)./sin(alpha) ...
.*(Rio+Roo).*lambda1.*cos(alpha).^2./0.2e1-(Roo-Rio)./lambda1.^2 ...
.*(0.1e1-lambda1.^2.*cos(alpha).^2).^(-0.1e1./0.2e1).*sin(alpha) ...
./0.2e1+(Roo-Rio).*(0.1e1-lambda1.^2.*cos(alpha).^2).^(-0.3e1 ...
./0.2e1).*sin(alpha).*cos(alpha).^2./0.2e1)./(nu.*m.*tan(alpha) ...
.*(0.1e1-lambda1.^2.*cos(alpha).^2)./(Roo-Rio)./sin(alpha)./pi ...
./Roo./0.2e1-m.*lambda1.*cos(alpha)./pi./((sqrt(0.1e1-lambda1.^2 ...
.*cos(alpha).^2)./sin(alpha).*(Rio+Roo)./0.2e1+(Roo-Rio)./lambda1 ...
.*(0.1e1-lambda1.^2.*cos(alpha).^2).^(-0.1e1./0.2e1).*sin(alpha) ...
./0.2e1).^2-(sqrt(0.1e1-lambda1.^2.*cos(alpha).^2)./sin(alpha) ...
.*(Rio+Roo)./0.2e1-(Roo-Rio)./lambda1.*(0.1e1-lambda1.^2 ...
.*cos(alpha).^2).^(-0.1e1./0.2e1).*sin(alpha)./0.2e1).^2)).^2.*L ...
./cos(alpha)./Ep./pi./ds.^2-0.4e1.*m.*(Er.*(lambda1-0.1e1)+nu.*p ...
.*(sqrt(0.1e1-lambda1.^2.*cos(alpha).^2)./sin(alpha).*(Rio+Roo) ...
./0.2e1-(Roo-Rio)./lambda1.*(0.1e1-lambda1.^2 ...
.*cos(alpha).^2).^(-0.1e1./0.2e1).*sin(alpha)./0.2e1)./(Roo-Rio) ...
.*lambda1.*sqrt(0.1e1-lambda1.^2.*cos(alpha).^2)./sin(alpha)-(pi ...
.*p.*(sqrt(0.1e1-lambda1.^2.*cos(alpha).^2)./sin(alpha).*(Rio+Roo) ...
./0.2e1-(Roo-Rio)./lambda1.*(0.1e1-lambda1.^2 ...
.*cos(alpha).^2).^(-0.1e1./0.2e1).*sin(alpha)./0.2e1).^2+Ftube) ...
./pi./((sqrt(0.1e1-lambda1.^2.*cos(alpha).^2)./sin(alpha).*(Rio ...
+Roo)./0.2e1+(Roo-Rio)./lambda1.*(0.1e1-lambda1.^2 ...
.*cos(alpha).^2).^(-0.1e1./0.2e1).*sin(alpha) ...
./0.2e1).^2-(sqrt(0.1e1-lambda1.^2.*cos(alpha).^2)./sin(alpha) ...
.*(Rio+Roo)./0.2e1-(Roo-Rio)./lambda1.*(0.1e1-lambda1.^2 ...
.*cos(alpha).^2).^(-0.1e1./0.2e1).*sin(alpha)./0.2e1).^2)).^2 ...
.*(0.1e1+(sqrt(0.1e1-lambda1.^2.*cos(alpha).^2)./sin(alpha).*(Rio ...
+Roo)./0.2e1+(Roo-Rio)./lambda1.*(0.1e1-lambda1.^2 ...
.*cos(alpha).^2).^(-0.1e1./0.2e1).*sin(alpha)./0.2e1-rf).^2 ...
./delta.^2)./(nu.*m.*tan(alpha).*(0.1e1-lambda1.^2.*cos(alpha).^2) ...
```

```
./(Roo—Rio)./sin(alpha)./pi./Roo./0.2e1—m.*lambda1.*cos(alpha)./pi ...
./((sqrt(0.1e1—lambda1.^2.*cos(alpha).^2)./sin(alpha).*(Rio+Roo) ...
./0.2e1+(Roo—Rio)./lambda1.*(0.1e1—lambda1.^2 ...
.*cos(alpha).^2).^(—0.1e1./0.2e1).*sin(alpha) ...
./0.2e1).^2—(sqrt(0.1e1—lambda1.^2.*cos(alpha).^2)./sin(alpha) ...
.*(Rio+Roo)./0.2e1—(Roo—Rio)./lambda1.*(0.1e1—lambda1.^2 ...
.*cos(alpha).^2).^(—0.1e1./0.2e1).*sin(alpha)./0.2e1).^2)).^3.*L ...
./cos(alpha)./Ep./pi./ds.^2.*(—nu.*m.*tan(alpha).*lambda1 ...
.*cos(alpha).^2./(Roo—Rio)./sin(alpha)./pi./Roo—m.*cos(alpha)./pi ...
./((sqrt(0.1e1—lambda1.^2.*cos(alpha).^2)./sin(alpha).*(Rio+Roo) ...
./0.2e1+(Roo—Rio)./lambda1.*(0.1e1—lambda1.^2 ...
.*cos(alpha).^2).^(—0.1e1./0.2e1).*sin(alpha) ...
./0.2e1).^2—(sqrt(0.1e1—lambda1.^2.*cos(alpha).^2)./sin(alpha) ...
.*(Rio+Roo)./0.2e1—(Roo—Rio)./lambda1.*(0.1e1—lambda1.^2 ...
.*cos(alpha).^2).^(—0.1e1./0.2e1).*sin(alpha)./0.2e1).^2)+m ...
.*lambda1.*cos(alpha)./pi./((sqrt(0.1e1—lambda1.^2.*cos(alpha).^2) ...
./sin(alpha).*(Rio+Roo)./0.2e1+(Roo—Rio)./lambda1 ...
.*(0.1e1—lambda1.^2.*cos(alpha).^2).^(—0.1e1./0.2e1).*sin(alpha) ...
./0.2e1).^2—(sqrt(0.1e1—lambda1.^2.*cos(alpha).^2)./sin(alpha) ...
.*(Rio+Roo)./0.2e1—(Roo—Rio)./lambda1.*(0.1e1—lambda1.^2 ...
.*cos(alpha).^2).^(—0.1e1./0.2e1).*sin(alpha)./0.2e1).^2).^2 ...
.*(0.2e1.*(sqrt(0.1e1—lambda1.^2.*cos(alpha).^2)./sin(alpha).*(Rio ...
+Roo)./0.2e1+(Roo—Rio)./lambda1.*(0.1e1—lambda1.^2 ...
.*cos(alpha).^2).^(—0.1e1./0.2e1).*sin(alpha)./0.2e1) ...
.*(—(0.1e1—lambda1.^2.*cos(alpha).^2).^(—0.1e1./0.2e1)./sin(alpha) ...
.*(Rio+Roo).*lambda1.*cos(alpha).^2./0.2e1—(Roo—Rio)./lambda1.^2 ...
.*(0.1e1—lambda1.^2.*cos(alpha).^2).^(—0.1e1./0.2e1).*sin(alpha) ...
./0.2e1+(Roo—Rio).*(0.1e1—lambda1.^2.*cos(alpha).^2).^(—0.3e1 ...
./0.2e1).*sin(alpha).*cos(alpha).^2./0.2e1)—0.2e1 ...
.*(sqrt(0.1e1—lambda1.^2.*cos(alpha).^2)./sin(alpha).*(Rio+Roo) ...
./0.2e1—(Roo—Rio)./lambda1.*(0.1e1—lambda1.^2 ...
.*cos(alpha).^2).^(—0.1e1./0.2e1).*sin(alpha)./0.2e1) ...
.*(—(0.1e1—lambda1.^2.*cos(alpha).^2).^(—0.1e1./0.2e1)./sin(alpha) ...
.*(Rio+Roo).*lambda1.*cos(alpha).^2./0.2e1+(Roo—Rio)./lambda1.^2 ...
.*(0.1e1—lambda1.^2.*cos(alpha).^2).^(—0.1e1./0.2e1).*sin(alpha) ...
./0.2e1—(Roo—Rio).*(0.1e1—lambda1.^2.*cos(alpha).^2).^(—0.3e1 ...
./0.2e1).*sin(alpha).*cos(alpha).^2./0.2e1)));
```

B

Input-Force-to-Transmitted-Force Transfer Function Coefficients for Pitch Links Coupled with Three Different Fluidic Circuits

Fluidic Circuits I and II: Out-of-Phase Forcing

$a_1 = A^2 I m$

$a_2 = A^2 (c_o I + m R_f)$

$a_3 = A^2 (c_o R_f + I k_o) + m(k_d + k_o)$

$a_4 = A^2 k_o R_f + c_o (k_d + k_o)$

$a_5 = k_d k_o$

$b_1 = A^2 I k_o$

$b_2 = A^2 k_o R_f$

$b_3 = k_d k_o$

Fluidic Circuit I: In-Phase Forcing

$$a_1 = A^2 C_a m(I + 2I_v)$$

$$a_2 = A^2 C_a \left[c_o(I + 2I_v) + m(R_f + 2R_v) \right]$$

$$a_3 = A^2 C_a \left[k_o(I + 2I_v) + c_o(R_f + 2R_v) \right] + C_a m(k_d + k_o) + 2A^2 m$$

$$a_4 = A^2 C_a k_o(R_f + 2R_v) + C_a c_o(k_d + k_o) + 2A^2 c_o$$

$$a_5 = k_o(2A^2 + C_a k_d)$$

$$b_1 = A^2 C_a k_o(I + 2I_v)$$

$$b_2 = A^2 C_a k_o(R_f + 2R_v)$$

$$b_3 = k_o(2A^2 + C_a k_d)$$

Fluidic Circuit II: In-Phase Forcing

$$a_1 = A^2 C_{a_1} C_{a_2} m \left[I(I_{v_1} + I_{v_2}) + 2 I_{v_1} I_{v_2} \right]$$

$$a_2 = A^2 C_{a_1} C_{a_2} \left[c_o \left[I(I_{v_1} + I_{v_2}) + 2 I_{v_1} I_{v_2} \right] + m \left[I(R_{v_1} + R_{v_2}) + R_f(I_{v_1} + I_{v_2}) \right.\right.$$
$$\left.\left. + 2(I_{v_1} R_{v_2} + I_{v_2} R_{v_1}) \right] \right]$$

$$a_3 = A^2 m C_{a_1} (I + 2 I_{v_1}) + A^2 m C_{a_2} (I + 2 I_{v_2}) + C_{a_1} C_{a_2} \left[A^2 \left[c_o(I(R_{v_1} + R_{v_2}) + R_f(I_{v_1} + I_{v_2}) \right.\right.$$
$$\left. + 2(I_{v_1} R_{v_2} + I_{v_2} R_{v_1})) + k_o(I(I_{v_1} + I_{v_2}) + 2 I_{v_1} I_{v_2}) + m(R_f(R_{v_1} + R_{v_2}) + 2 R_{v_1} R_{v_2}) \right]$$
$$\left. + m(k_d + k_o)(I_{v_1} + I_{v_2}) \right]$$

$$a_4 = A^2 C_{a_1} \left[c_o(I + 2 I_{v_1}) + m(R_f + 2 R_{v_1}) \right] + A^2 C_{a_2} \left[c_o(I + 2 I_{v_2}) + m(R_f + 2 R_{v_2}) \right]$$
$$+ C_{a_1} C_{a_2} \left[A^2 \left[c_o(R_f(R_{v_1} + R_{v_2}) + 2 R_{v_1} R_{v_2}) + k_o(I(R_{v_1} + R_{v_2}) + R_f(I_{v_1} + I_{v_2}) \right.\right.$$
$$\left.\left. + 2(I_{v_1} R_{v_2} + I_{v_2} R_{v_1})) \right] + (k_d + k_o) \left[c_o(I_{v_1} + I_{v_2}) + m(R_{v_1} + R_{v_2}) \right] \right]$$

$$a_5 = 2 A^2 m + C_{a_1} \left[A^2 \left[c_o(R_f + 2 R_{v_1}) + k_o(I + 2 I_{v_1}) \right] + m(k_d + k_o) \right]$$
$$+ C_{a_2} \left[A^2 \left[c_o(R_f + 2 R_{v_2}) + k_o(I + 2 I_{v_2}) \right] + m(k_d + k_o) \right]$$
$$+ C_{a_1} C_{a_2} \left[A^2 k_o(R_f(R_{v_1} + R_{v_2}) + 2 R_{v_1} R_{v_2}) + c_o(k_d + k_o)(R_{v_1} + R_{v_2}) + k_d k_o(I_{v_1} + I_{v_2}) \right]$$

$$a_6 = 2 A^2 c_o + C_{a_1} \left[c_o(k_d + k_o) + A^2 k_o(R_f + 2 R_{v_1}) \right] + C_{a_2} \left[c_o(k_d + k_o) + A^2 k_o(R_f + 2 R_{v_2}) \right]$$
$$+ C_{a_1} C_{a_2} k_d k_o(R_{v_1} + R_{v_2})$$

$$a_7 = k_o \left[2 A^2 + k_d(C_{a_1} + C_{a_2}) \right]$$

$$b_1 = A^2 C_{a_1} C_{a_2} k_o \left[I(I_{v_1} + I_{v_2}) + 2I_{v_1} I_{v_2} \right]$$

$$b_2 = A^2 C_{a_1} C_{a_2} k_o \left[I(R_{v_1} + R_{v_2}) + R_f(I_{v_1} + I_{v_2}) + 2(I_{v_1} R_{v_2} + I_{v_2} R_{v_1}) \right]$$

$$b_3 = k_o \left[A^2 C_{a_1}(I + 2I_{v_1}) + A^2 C_{a_2}(I + 2I_{v_2}) \right.$$
$$\left. + C_{a_1} C_{a_2} \left[A^2(R_f(R_{v_1} + R_{v_2}) + 2R_{v_1} R_{v_2}) + k_d(I_{v_1} + I_{v_2}) \right] \right]$$

$$b_4 = k_o \left[A^2 C_{a_1}(R_f + 2R_{v_1}) + A^2 C_{a_2}(R_f + 2R_{v_2}) + C_{a_1} C_{a_2} k_d(R_{v_1} + R_{v_2}) \right]$$

$$b_5 = k_o \left[2A^2 + k_d(C_{a_1} + C_{a_2}) \right]$$

Fluidic Circuit III: Out-of-Phase Forcing

$$a_1 = A^2 C_a I I_3 m$$

$$a_2 = A^2 C_a \left[c_o I I_3 + m(IR_3 + I_3 R_f) \right]$$

$$a_3 = A^2 \left[m(2I + I_3) + C_a \left[I I_3 k_o + c_o(IR_3 + I_3 R_f) + mR_f R_3 \right] \right] + C_a I_3 m(k_d + k_o)$$

$$a_4 = A^2 \left[m(2R_f + R_3) + C_a \left[c_o R_f R_3 + k_o(IR_3 + I_3 R_f) \right] + c_o(2I + I_3) \right]$$
$$+ C_a(k_d + k_o)(c_o I_3 + mR_3)$$

$$a_5 = A^2 \left[c_o(2R_f + R_3) + k_o(2I + I_3 + C_a R_f R_3) \right] + C_a \left[k_o(c_o R_3 + I_3 k_d) + c_o k_d R_3 \right]$$
$$+ 2m(k_d + k_o)$$

$$a_6 = A^2 k_o(2R_f + R_3) + C_a k_d k_o R_3 + 2c_o(k_d + k_o)$$

$$a_7 = 2k_d k_o$$

$$b_1 = A^2 C_a I I_3 k_o$$

$$b_2 = A^2 C_a k_o (I R_3 + I_3 R_f)$$

$$b_3 = k_o \left[A^2 (2I + I_3 + C_a R_f R_3) + C_a I_3 k_d \right]$$

$$b_4 = k_o \left[A^2 (2R_f + R_3) + C_a k_d R_3 \right]$$

$$b_5 = 2 k_d k_o$$

Fluidic Circuit III: In-Phase Forcing

$$a_1 = A^2 C_a I m$$

$$a_2 = A^2 C_a (c_o I + m R_f)$$

$$a_3 = A^2 m + C_a \left[A^2 (c_o R_f + I k_o) + m(k_d + k_o) \right]$$

$$a_4 = A^2 c_o + C_a \left[A^2 k_o R_f + c_o(k_d + k_o) \right]$$

$$a_5 = k_o (A^2 + C_a k_d)$$

$$b_1 = A^2 C_a I k_o$$

$$b_2 = A^2 C_a k_o R_f$$

$$b_3 = k_o (A^2 + C_a k_d)$$

Frequency Responses and Source Code for Coupled Pitch Links

C.1 Frequency Responses of Both Fluidic Pitch Links for Fluidic Circuit I

Figure C.1 shows the theoretical and experimental frequency responses, with and without fluid, for two coupled fluidic pitch links with a single vertical fluid track. See Fig. 3.8 for the experimental setup.

C.2 Matlab® Code for Fluidic Circuit I

```
%Lloyd Scarborough
%Created March 21, 2012
%Last modified November 13, 2013
%Force transfer functions for 2-pitch link case with an accumulator,
%forcing split into odd and even cases, ko added, co and cd added
%Total transmitted force calculated and plotted

clear all
close all
clc
```
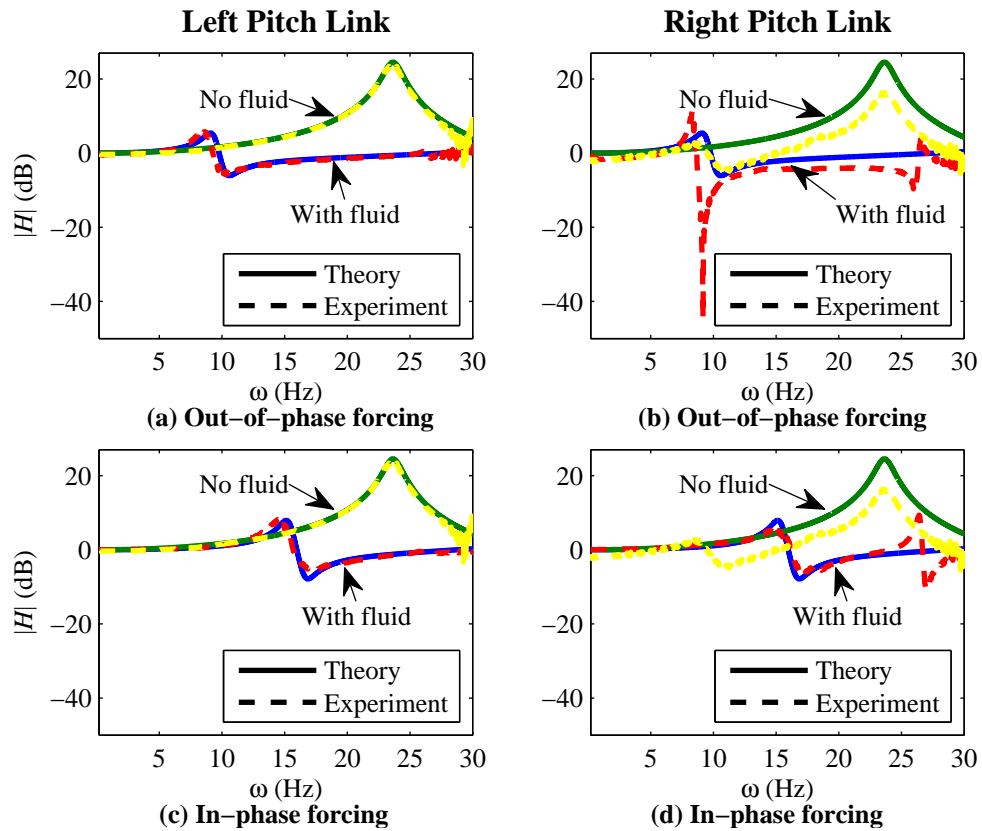
Figure C.1. Frequency responses of two coupled pitch links with a single vertical fluid track.

```matlab
load 'IsolatorI_empty.lvm'
load 'IsolatorII_empty.lvm'
load 'odd_total_I.lvm'
load 'odd_total_II.lvm'
load 'even_total_I.lvm'
load 'even_total_II.lvm'

f1b=IsolatorI_empty(:,1);
f2b=IsolatorII_empty(:,1);
H1b=IsolatorI_empty(:,2);
H2b=IsolatorII_empty(:,2);

fo11=odd_total_I(:,1);
fo22=odd_total_II(:,1);
fe11=even_total_I(:,1);
fe22=even_total_II(:,1);
Ho11=odd_total_I(:,2);
Ho22=odd_total_II(:,2);
He11=even_total_I(:,2);
He22=even_total_II(:,2);
```

```
m=1.13;                 %mass, kg
ko=100000000*460e3; %baseline stiffness, N/m (rigid)
cd=10;                  %diaphragm damping (3% of critical), N.s/m
co=0;                   %baseline damping, N.s/m
kd=2.5e4;               %elastomer stiffness, N/m
D=0.044;                %pumper diameter, m
d=0.473*0.0254;         %fluid-track diameter, m
L=0.19;                 %horizontal fluid-track half-length, m
rho=1000;               %fluid density, kg/m^3

%Fluid-track inertance, kg/m^4
I=(4*rho*0.018/(pi*0.011^2)+4*rho*0.02/(pi*0.0095^2)...
    +4*rho*L/(pi*d^2))+4*rho*0.03/(pi*0.017^2);

A=pi/4*D^2;             %pumper area, m^2
Afp=pi/4*d^2;           %fluid-port area, m^2

Cp=1.7e-11;             %pitch-link capacitance, m^3/Pa

r=6.0e7;                %resistance to flow per length, kg*s/m^4/m
R=r*(L+0.07);           %resistance to flow, kg*s/m^4

%%%%%%%%%%%%%%%%%%%%%%%%%%%%%%%%%%%%%%%%%%%%%%%%%%%%%%%%%%%%%%%%%%%%%%
%Accumulator values and calculations
da=0.473*0.0254;    %fluid track to accumulator diameter, m
La=0.03;                %fluid track to accumulator length, m
Lt=La+0.13;             %total length of accumulator and fluid track, m
p_atm=101e3;            %atmospheric pressure, Pa
p_ao=50e3;              %accumulator initial pressure, Pa
%Accumulator fluid-track inertance, kg/m^4
Ia=4*rho*La/(pi*da^2);
%Accumulator capacitance, m^4.s^2/kg
Ca=(pi/4)*da^2*(Lt-La)/(p_ao+p_atm);
%Resistance to flow of track to accumulator, kg*s/m^4
Ra=r*La;
%%%%%%%%%%%%%%%%%%%%%%%%%%%%%%%%%%%%%%%%%%%%%%%%%%%%%%%%%%%%%%%%%%%%%%

w=0:0.01:2*pi*50;   %frequency vector, rad/s
s=1i*w;                 %s=jw

%Input-force-to-transmitted-force transfer fnc. for out-of-phase forcing
FtoverFodd=2.*ko.*(I.*s.^3.*Cp.*cd+((R.*cd+I.*kd).*Cp-1./2.*A.*I ...
.*(-2.*A+Afp)).*s.^2+(R.*Cp.*kd-1./2.*A.*(-2.*A+Afp).*R+cd).*s+kd) ...
./(2.*m.*I.*s.^5.*Cp.*cd+(((2.*cd.*co+2.*ko.*m+2.*m.*kd).*I ...
+2.*m.*R.*cd).*Cp+2.*I.*A.^2.*m).*s.^4+((((2.*cd+2.*co).*ko+2.*kd ...
.*co).*I+2.*R.*(ko.*m+m.*kd+cd.*co)).*Cp+2.*I.*A.^2.*co+2.*m.*(R ...
.*A.^2+cd)).*s.^3+((2.*ko.*I.*kd+2.*((cd+co).*ko+kd.*co).*R).*Cp+2 ...
.*m.*kd+2.*cd.*co+2.*ko.*m+2.*ko.*I.*A.^2+2.*R.*A.^2.*co).*s.^2+(2 ...
.*R.*Cp.*kd.*ko+(2.*co+2.*R.*A.^2+2.*cd).*ko+2.*kd.*co).*s+2.*kd.*ko);
```

```matlab
%Input-force-to-transmitted-force transfer fnc. for in-phase forcing
FtoverFeven=2.*ko.*(Cp.*cd.*Ca.*(2.*Ia+I).*s.^3+Ca.*(((2.*Ia+I).*kd ...
+cd.*(R+2.*Ra)).*Cp+(A-1./2.*Afp).*A.*(2.*Ia+I)).*s.^2+((kd.*(R+2 ...
.*Ra).*Cp+cd+(R+2.*Ra).*A.^2+(-Ra.*Afp-1./2.*R.*Afp).*A).*Ca+2.*Cp ...
.*cd).*s+2.*Cp.*kd+2.*A.^2+Ca.*kd).*(2.*Cp.*cd.*m.*Ca.*(2.*Ia+I) ...
.*s.^5+2.*((m.*(2.*Ia+I).*ko+m.*(2.*Ia+I).*kd+((2.*Ia+I).*co+m.*(R ...
+2.*Ra)).*cd).*Cp+A.^2.*m.*(2.*Ia+I)).*Ca.*s.^4+(((((4.*Ia+2.*I) ...
.*cd+(4.*Ia+2.*I).*co+2.*m.*(R+2.*Ra)).*ko+((4.*Ia+2.*I).*co+2.*m ...
.*(R+2.*Ra)).*kd+2.*cd.*co.*(R+2.*Ra)).*Cp+2.*m.*cd+2.*A.^2.*((2 ...
.*Ia+I).*co+m.*(R+2.*Ra))).*Ca+4.*Cp.*cd.*m).*s.^3+(((((4.*Ia+2 ...
.*I).*kd+2.*(cd+co).*(R+2.*Ra)).*ko+2.*kd.*co.*(R+2.*Ra)).*Cp+(2.*m ...
+(4.*Ia+2.*I).*A.^2).*ko+2.*kd.*m+2.*co.*(cd+(R+2.*Ra).*A.^2)).*Ca ...
+(4.*cd.*co+4.*kd.*m+4.*ko.*m).*Cp+4.*A.^2.*m).*s.^2+((2.*kd.*ko ...
.*(R+2.*Ra).*Cp+(2.*co+2.*cd+(4.*Ra+2.*R).*A.^2).*ko+2.*kd.*co).*Ca ...
+((4.*cd+4.*co).*ko+4.*kd.*co).*Cp+4.*A.^2.*co).*s+4.*ko.*(Cp.*kd ...
+1./2.*Ca.*kd+A.^2));

%Baseline input-force-to-transmitted-force transfer function
FtoverF_base=(cd*s+kd)./(m*s.^2+cd*s+kd);

figure(1)
subplot(2,2,1)
hold on
plot(w/(2*pi),20*log10(abs(FtoverFodd)),w/(2*pi),...
    20*log10(abs(FtoverF_base)),fo22,20*log10(Ho22),'--',...
    f2b,20*log10(H2b),'y--','LineWidth',2,'HandleVisibility','off')
plot(w/(2*pi),w+100,'k',w/(2*pi),w+101,'k--','LineWidth',2)
axis([0.2 30 -50 27])
set(gca,'FontName','Times New Roman','FontSize',10);
title('\bf{Left Pitch Link}','FontName','Times New Roman',...
    'FontSize',12)
xlabel('\it\omega \rm(Hz)','FontName','Times New Roman','FontSize',10)
ylabel('|\itH\rm| (dB)','FontName','Times New Roman','FontSize',10)
legend('Theory','Experiment','location','southeast')
hold off
box on
text(4,-71,'\bf{(a) Out-of-phase forcing}','FontName',...
    'Times New Roman','FontSize',10)
annotation('textarrow',[0.3,0.34],[0.87,0.85],'string','No fluid',...
    'FontName','Times New Roman','FontSize',10)
annotation('textarrow',[0.35,0.34],[0.75,0.795],'string',...
    'With fluid','FontName','Times New Roman','FontSize',10)

subplot(2,2,2)
hold on
plot(w/(2*pi),20*log10(abs(FtoverFodd)),w/(2*pi),...
    20*log10(abs(FtoverF_base)),fo11,20*log10(Ho11),'--',...
    f1b,20*log10(H1b),'y--','LineWidth',2,'HandleVisibility','off')
plot(w/(2*pi),w+100,'k',w/(2*pi),w+101,'k--','LineWidth',2)
axis([0.2 30 -50 27])
set(gca,'FontName','Times New Roman','FontSize',10);
```

```matlab
title('\bf{Right Pitch Link}','FontName','Times New Roman',...
    'FontSize',12)
xlabel('\it\omega \rm(Hz)','FontName','Times New Roman','FontSize',10)
legend('Theory','Experiment','location','southeast')
hold off
box on
text(4,-71,'\bf{(b) Out-of-phase forcing}','FontName',...
    'Times New Roman','FontSize',10)
annotation('textarrow',[0.73,0.78],[0.87,0.85],'string','No fluid',...
    'FontName','Times New Roman','FontSize',10)
annotation('textarrow',[0.79,0.75],[0.75,0.79],'string',...
    'With fluid','FontName','Times New Roman','FontSize',10)

subplot(2,2,3)
hold on
plot(w/(2*pi),20*log10(abs(FtoverFeven)),w/(2*pi),...
    20*log10(abs(FtoverF_base)),fe22,20*log10(He22),'--',...
    f2b,20*log10(H2b),'y--','LineWidth',2,'HandleVisibility','off')
plot(w/(2*pi),w+100,'k',w/(2*pi),w+101,'k--','LineWidth',2)
axis([0.2 30 -50 27])
set(gca,'FontName','Times New Roman','FontSize',10);
xlabel('\it\omega \rm(Hz)','FontName','Times New Roman','FontSize',10)
ylabel('|\itH\rm| (dB)','FontName','Times New Roman','FontSize',10)
legend('Theory','Experiment','location','southeast')
hold off
box on
text(5,-71,'\bf{(c) In-phase forcing}','FontName',...
    'Times New Roman','FontSize',10)
annotation('textarrow',[0.3,0.34],[0.41,0.38],'string',...
    'No fluid','FontName','Times New Roman','FontSize',10)
annotation('textarrow',[0.36,0.35],[0.27,0.31],'string',...
    'With fluid','FontName','Times New Roman','FontSize',10)

subplot(2,2,4)
hold on
plot(w/(2*pi),20*log10(abs(FtoverFeven)),w/(2*pi),...
    20*log10(abs(FtoverF_base)),fe11,20*log10(He11),'--',...
    f1b,20*log10(H1b),'y--','LineWidth',2,'HandleVisibility','off')
plot(w/(2*pi),w+100,'k',w/(2*pi),w+101,'k--','LineWidth',2)
axis([0.2 30 -50 27])
set(gca,'FontName','Times New Roman','FontSize',10);
xlabel('\it\omega \rm(Hz)','FontName','Times New Roman','FontSize',10)
legend('Theory','Experiment','location','southeast')
hold off
box on
text(5,-71,'\bf{(d) In-phase forcing}','FontName',...
    'Times New Roman','FontSize',10)
annotation('textarrow',[0.73,0.78],[0.41,0.38],'string',...
    'No fluid','FontName','Times New Roman','FontSize',10)
annotation('textarrow',[0.8,0.79],[0.27,0.31],'string',...
    'With fluid','FontName','Times New Roman','FontSize',10)
```
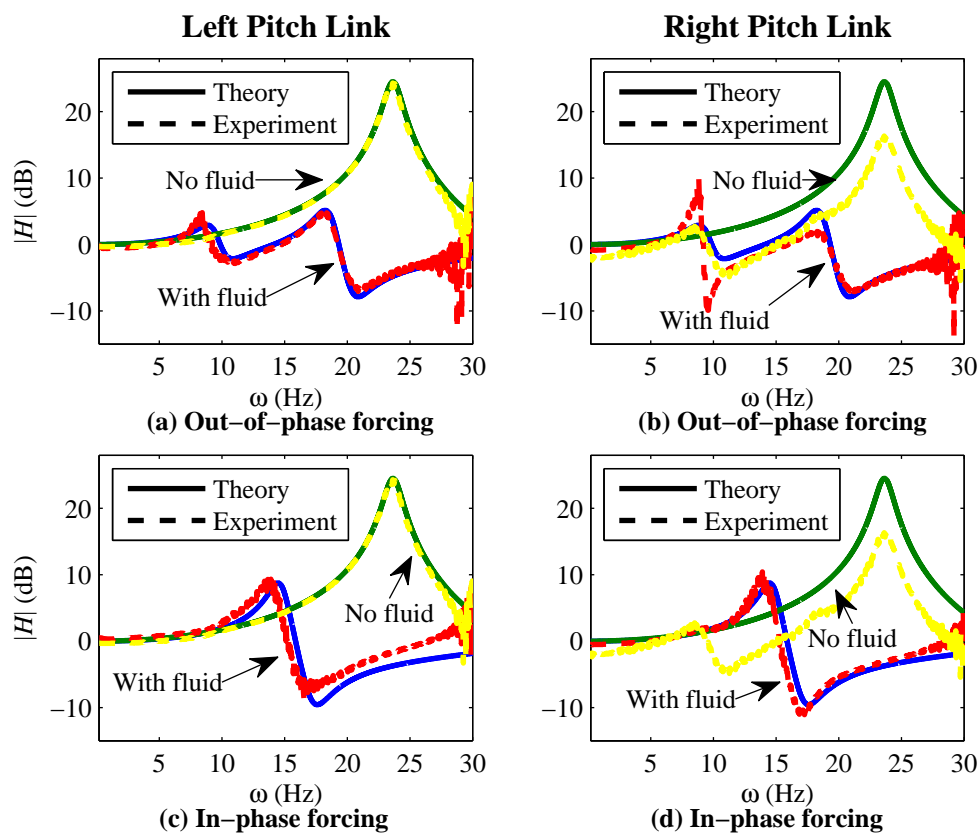
C.3 Frequency Responses of Both Fluidic Pitch Links for Fluidic Circuit III

Figure C.2 shows the theoretical and experimental frequency responses, with and without fluid, for two coupled fluidic pitch links with a single fluid track with two in-line accumulators. See Fig. 3.10 for the experimental setup.

Figure C.2. Frequency responses of two coupled fluidic pitch links with a single fluid track with two in-line accumulators.

C.4 Matlab® Code for Fluidic Circuit III

```matlab
%Lloyd Scarborough
%Created September 11, 2012
%Last modified November 13, 2013
%Force transfer functions for 2-pitch link case with a single fluid
%track with two in-line accumulators - forcing split into odd and
%even cases, ko added, co and cd added

clear all
close all
clc

load 'IsolatorI_empty.lvm'
load 'IsolatorII_empty.lvm'
load 'tia_odd_total_I_ss_st_insts_as_synch.lvm'
load 'tia_odd_total_II_ss_st_insts_as_synch.lvm'
load 'tia_even_total_I_ss_st_insts_as_synch.lvm'
load 'tia_even_total_II_ss_st_insts_as_synch.lvm'

f1b=IsolatorI_empty(:,1);
f2b=IsolatorII_empty(:,1);
H1b=IsolatorI_empty(:,2);
H2b=IsolatorII_empty(:,2);

fo11ssstinstsassy=tia_odd_total_I_ss_st_insts_as_synch(:,1);
fe11ssstinstsassy=tia_even_total_I_ss_st_insts_as_synch(:,1);
fo22ssstinstsassy=tia_odd_total_II_ss_st_insts_as_synch(:,1);
fe22ssstinstsassy=tia_even_total_II_ss_st_insts_as_synch(:,1);
Ho11ssstinstsassy=tia_odd_total_I_ss_st_insts_as_synch(:,2);
He11ssstinstsassy=tia_even_total_I_ss_st_insts_as_synch(:,2);
Ho22ssstinstsassy=tia_odd_total_II_ss_st_insts_as_synch(:,2);
He22ssstinstsassy=tia_even_total_II_ss_st_insts_as_synch(:,2);

m=1.13;              %mass, kg
ko=460e3*100000000;  %baseline stiffness, N/m (rigid)
cd=10;               %diaphragm damping (3% of critical), N.s/m
co=0;                %baseline damping, N.s/m
kd=2.5e4;            %elastomer stiffness, N/m
D=0.044;             %pumper diameter, m
d=0.473*0.0254;      %fluid-track diameter, m
L=0.07;              %outer fluid-track length, m
rho=1000;            %fluid density, kg/m^3
Lel=0.8*L;           %distance from pitch link to nearest accumulator, m

%Fluid-track inertance, kg/m^4
I=4*rho*0.018/(pi*0.011^2)+4*rho*0.019/(pi*0.008^2)...
    +4*rho*L/(pi*d^2)+4*rho*0.02/(pi*0.017^2);
```

```
A=pi/4*D^2;              %pumper area, m^2
Afp=pi/4*d^2;            %fluid-port area, m^2

Ca=2.0e-10;             %accumulator capacitance, m^3/Pa
Cp=1.7e-11;             %pitch-link capacitance, m^3/Pa

r=1.1e8;                %resistance to flow per length, kg*s/m^4/m
R=r*(L+0.06);           %resistance to flow, kg*s/m^4

L3=0.12;                %center fluid-track length, m
d3=0.012;               %tee diameter, m

%Fluid-track inertance, kg/m^4
I3=4*rho*L3/(pi*d3^2)+4*rho*0.02/(pi*0.017^2);

R3=r*(L3+0.02);         %resistance to flow, kg*s/m^4

w=0:0.01:2*pi*50;       %frequency vector, rad/s
s=1i*w;                 %s=jw

%Input-force-to-transmitted-force transfer fnc. for out-of-phase forcing
FtoverFodd=-ko.*(-cd.*s.^5.*L.*Ca.*I.*I3.*Cp-Ca.*((R3.*I.*cd+I3 ...
.*(R.*cd+I.*kd)).*L.*Cp-A.*I.*I3.*(-L.*A+Lel.*Afp)).*s.^4+((-L ...
.*((R.*cd+I.*kd).*R3+kd.*I3.*R).*Cp+A.*I.*(-L.*A+Lel.*Afp).*R3+I3 ...
.*((-A.^2.*L+A.*Afp.*Lel).*R-cd.*L)).*Ca-L.*cd.*Cp.*(2.*I+I3)) ...
.*s.^3+((-kd.*L.*R3.*Cp.*R+((-A.^2.*L+A.*Afp.*Lel).*R-cd.*L) ...
.*R3-kd.*L.*I3).*Ca-2.*(1./2.*cd.*R3+R.*cd+1./2.*kd.*I3+I.*kd).*L ...
.*Cp-A.^2.*L.*I3+2.*A.*I.*(-L.*A+Lel.*Afp)).*s.^2+(-kd.*L.*Ca ...
.*R3-2.*L.*kd.*(R+1./2.*R3).*Cp-A.^2.*L.*R3+(-2.*A.^2.*L+2.*A.*Afp ...
.*Lel).*R-2.*cd.*L).*s-2.*kd.*L)./L./(I3.*s.^7.*Ca.*I.*Cp.*cd.*m ...
+((R3.*I.*cd.*m+(ko.*I.*m+(cd.*co+kd.*m).*I+R.*cd.*m).*I3).*Cp+I ...
.*I3.*A.^2.*m).*Ca.*s.^6+((((ko.*I.*m+(cd.*co+kd.*m).*I+R.*cd.*m) ...
.*R3+(((cd+co).*I+R.*m).*ko+co.*I.*kd+R.*(cd.*co+kd.*m)).*I3).*Cp ...
+I.*R3.*A.^2.*m+(I.*A.^2.*co+m.*(cd+R.*A.^2)).*I3).*Ca+m.*Cp.*cd ...
.*(2.*I+I3)).*s.^5+((((((cd+co).*I+R.*m).*ko+co.*I.*kd+R.*(cd.*co ...
+kd.*m)).*R3+I3.*((I.*kd+R.*(cd+co)).*ko+R.*co.*kd)).*Cp+(I.*A.^2 ...
.*co+m.*(cd+R.*A.^2)).*R3+((I.*A.^2+m).*ko+kd.*m+R.*A.^2.*co+cd ...
.*co).*I3).*Ca+(R3.*cd.*m+(cd.*co+ko.*m+kd.*m).*I3+2.*ko.*I.*m+(2 ...
.*kd.*m+2.*cd.*co).*I+2.*R.*cd.*m).*Cp+A.^2.*m.*(2.*I+I3)).*s.^4 ...
+((((((I.*kd+R.*(cd+co)).*ko+R.*co.*kd).*R3+I3.*R.*kd.*ko).*Cp+((I ...
.*A.^2+m).*ko+kd.*m+R.*A.^2.*co+cd.*co).*R3+I3.*((co+R.*A.^2+cd) ...
.*ko+kd.*co)).*Ca+((cd.*co+ko.*m+kd.*m).*R3+((cd+co).*ko+kd.*co) ...
.*I3+((2.*cd+2.*co).*I+2.*R.*m).*ko+2.*co.*I.*kd+2.*R.*(cd.*co+kd ...
.*m)).*Cp+R3.*A.^2.*m+I3.*A.^2.*co+2.*I.*A.^2.*co+2.*m.*(cd+R ...
.*A.^2)).*s.^3+((R3.*R.*ko.*Cp.*kd+((co+R.*A.^2+cd).*ko+kd.*co).*R3 ...
+I3.*ko.*kd).*Ca+(((cd+co).*ko+kd.*co).*R3+I3.*ko.*kd+(2.*I.*kd+2 ...
.*R.*(cd+co)).*ko+2.*R.*co.*kd).*Cp+R3.*A.^2.*co+ko.*I3.*A.^2+(2.*m ...
+2.*I.*A.^2).*ko+2.*R.*A.^2.*co+2.*kd.*m+2.*cd.*co).*s.^2+(R3.*ko ...
.*Ca.*kd+2.*(R+1./2.*R3).*kd.*ko.*Cp+ko.*R3.*A.^2+(2.*R.*A.^2+2.*co ...
+2.*cd).*ko+2.*kd.*co).*s+2.*kd.*ko);
```

```matlab
%Input-force-to-transmitted-force transfer fnc. for in-phase forcing
FtoverFeven=-(-cd.*s.^3.*L.*Ca.*Cp.*I+Ca.*(-L.*(R.*cd+kd.*I).*Cp+A ...
.*I.*(-L.*A+Afp.*Lel)).*s.^2+((-kd.*L.*R.*Cp-cd.*L+A.*R.*(-L.*A ...
+Afp.*Lel)).*Ca-Cp.*cd.*L).*s-L.*(Ca.*kd+Cp.*kd+A.^2)).*ko./L./(Ca ...
.*I.*s.^5.*Cp.*cd.*m+((I.*ko.*m+I.*kd.*m+cd.*(R.*m+I.*co)).*Cp+I ...
.*A.^2.*m).*Ca.*s.^4+((((I.*co+R.*m+I.*cd).*ko+(R.*m+I.*co).*kd+R ...
.*cd.*co).*Cp+cd.*m+A.^2.*(R.*m+I.*co)).*Ca+Cp.*cd.*m).*s.^3 ...
+((((kd.*I+R.*(cd+co)).*ko+R.*kd.*co).*Cp+(m+I.*A.^2).*ko+kd.*m+co ...
.*(R.*A.^2+cd)).*Ca+(co.*cd+ko.*m+kd.*m).*Cp+A.^2.*m).*s.^2+((R ...
.*Cp.*kd.*ko+(cd+R.*A.^2+co).*ko+kd.*co).*Ca+((cd+co).*ko+kd.*co) ...
.*Cp+A.^2.*co).*s+ko.*(Ca.*kd+Cp.*kd+A.^2));

%Baseline input-force-to-transmitted-force transfer function
FtoverF_base=(cd*s+kd)./(m*s.^2+cd*s+kd);

figure(1)
subplot(2,2,1)
hold on
plot(w/(2*pi),20*log10(abs(FtoverFodd)),w/(2*pi),...
    20*log10(abs(FtoverF_base)),fo22ssstinstsassy,...
    20*log10(Ho22ssstinstsassy),'--',f2b,20*log10(H2b),...
    'y--','LineWidth',2,'HandleVisibility','off')
plot(w/(2*pi),w+100,'k',w/(2*pi),w+101,'k--','LineWidth',2)
axis([0.2 30 -15 28])
set(gca,'FontName','Times New Roman','FontSize',10);
title('\bf{Left Pitch Link}','FontName','Times New Roman',...
    'FontSize',12)
xlabel('\it\omega \rm(Hz)','FontName','Times New Roman','FontSize',10)
ylabel('|\itH\rm| (dB)','FontName','Times New Roman','FontSize',10)
legend('Theory','Experiment','location','northwest')
hold off
box on
text(4,-26.5,'\bf{(a) Out-of-phase forcing}','FontName',...
    'Times New Roman','FontSize',10)
annotation('textarrow',[0.27,0.33],[0.78,0.78],'string',...
    'No fluid','FontName','Times New Roman','FontSize',10)
annotation('textarrow',[0.28,0.34],[0.64,0.68],'string',...
    'With fluid','FontName','Times New Roman','FontSize',10)

subplot(2,2,2)
hold on
plot(w/(2*pi),20*log10(abs(FtoverFodd)),w/(2*pi),...
    20*log10(abs(FtoverF_base)),fo11ssstinstsassy,...
    20*log10(Ho11ssstinstsassy),'--',f1b,20*log10(H1b),...
    'y--','LineWidth',2,'HandleVisibility','off')
plot(w/(2*pi),w+100,'k',w/(2*pi),w+101,'k--','LineWidth',2)
axis([0.2 30 -15 28])
set(gca,'FontName','Times New Roman','FontSize',10);
title('\bf{Right Pitch Link}','FontName','Times New Roman',...
    'FontSize',12)
xlabel('\it\omega \rm(Hz)','FontName','Times New Roman','FontSize',10)
```

```matlab
legend('Theory','Experiment','location','northwest')
hold off
box on
text(4,-26.5,'\bf{(b) Out-of-phase forcing}','FontName',...
    'Times New Roman','FontSize',10)
annotation('textarrow',[0.76,0.79],[0.78,0.78],'string',...
    'No fluid','FontName','Times New Roman','FontSize',10)
annotation('textarrow',[0.73,0.78],[0.63,0.68],'string',...
    'With fluid','FontName','Times New Roman','FontSize',10)

subplot(2,2,3)
hold on
plot(w/(2*pi),20*log10(abs(FtoverFeven)),w/(2*pi),...
    20*log10(abs(FtoverF_base)),fe22ssstinstsassy,...
    20*log10(He22ssstinstsassy),'--',f2b,20*log10(H2b),...
    'y--','LineWidth',2,'HandleVisibility','off')
plot(w/(2*pi),w+100,'k',w/(2*pi),w+101,'k--','LineWidth',2)
axis([0.2 30 -15 28])
set(gca,'FontName','Times New Roman','FontSize',10);
xlabel('\it\omega \rm(Hz)','FontName','Times New Roman','FontSize',10)
ylabel('|\itH\rm| (dB)','FontName','Times New Roman','FontSize',10)
legend('Theory','Experiment','location','northwest')
hold off
box on
text(5,-26.5,'\bf{(c) In-phase forcing}','FontName',...
    'Times New Roman','FontSize',10)
annotation('textarrow',[0.39,0.41],[0.28,0.33],'string',...
    'No fluid','FontName','Times New Roman','FontSize',10)
annotation('textarrow',[0.24,0.29],[0.18,0.21],'string',...
    'With fluid','FontName','Times New Roman','FontSize',10)

subplot(2,2,4)
hold on
plot(w/(2*pi),20*log10(abs(FtoverFeven)),w/(2*pi),...
    20*log10(abs(FtoverF_base)),fe11ssstinstsassy,...
    20*log10(He11ssstinstsassy),'--',f1b,20*log10(H1b),...
    'y--','LineWidth',2,'HandleVisibility','off')
plot(w/(2*pi),w+100,'k',w/(2*pi),w+101,'k--','LineWidth',2)
axis([0.2 30 -15 28])
set(gca,'FontName','Times New Roman','FontSize',10);
xlabel('\it\omega \rm(Hz)','FontName','Times New Roman','FontSize',10)
legend('Theory','Experiment','location','northwest')
hold off
box on
text(5,-26.5,'\bf{(d) In-phase forcing}','FontName',...
    'Times New Roman','FontSize',10)
annotation('textarrow',[0.805,0.79],[0.25,0.29],'string',...
    'No fluid','FontName','Times New Roman','FontSize',10)
annotation('textarrow',[0.70,0.74],[0.16,0.18],'string',...
    'With fluid','FontName','Times New Roman','FontSize',10)
```

Appendix D

Flow Charts for Aeroelastic Simulation

Figures D.1-D.9 show how the main subroutines of the aeroelastic simulation of [58] interact. Each box is a subroutine, and the arrows point to other subroutines that are called by the originating subroutine. In general, the flow in each figure begins with a shaded box in the lower left and progresses to the upper right. Shaded boxes at the end of the flow of each figure indicate that the flow continues onto another figure. The box to the counterclockwise side of the arrow is a list of variables that are passed to the next subroutine, and the box to the clockwise side of the arrow is a list of variables that are returned to the originating subroutine.

Subroutine sol1 calculates the natural frequencies and modes of the blade. Subroutine sol2 calculates the response of the blade, using just linear terms initially, then incorporating nonlinear terms as well. Thus, Figs. D.2 and D.3 (blade response, linear portion) are similar to Figs. D.4 and D.5 (blade response, nonlinear portion). Subroutine sol3 calculates the blade and hub loads.
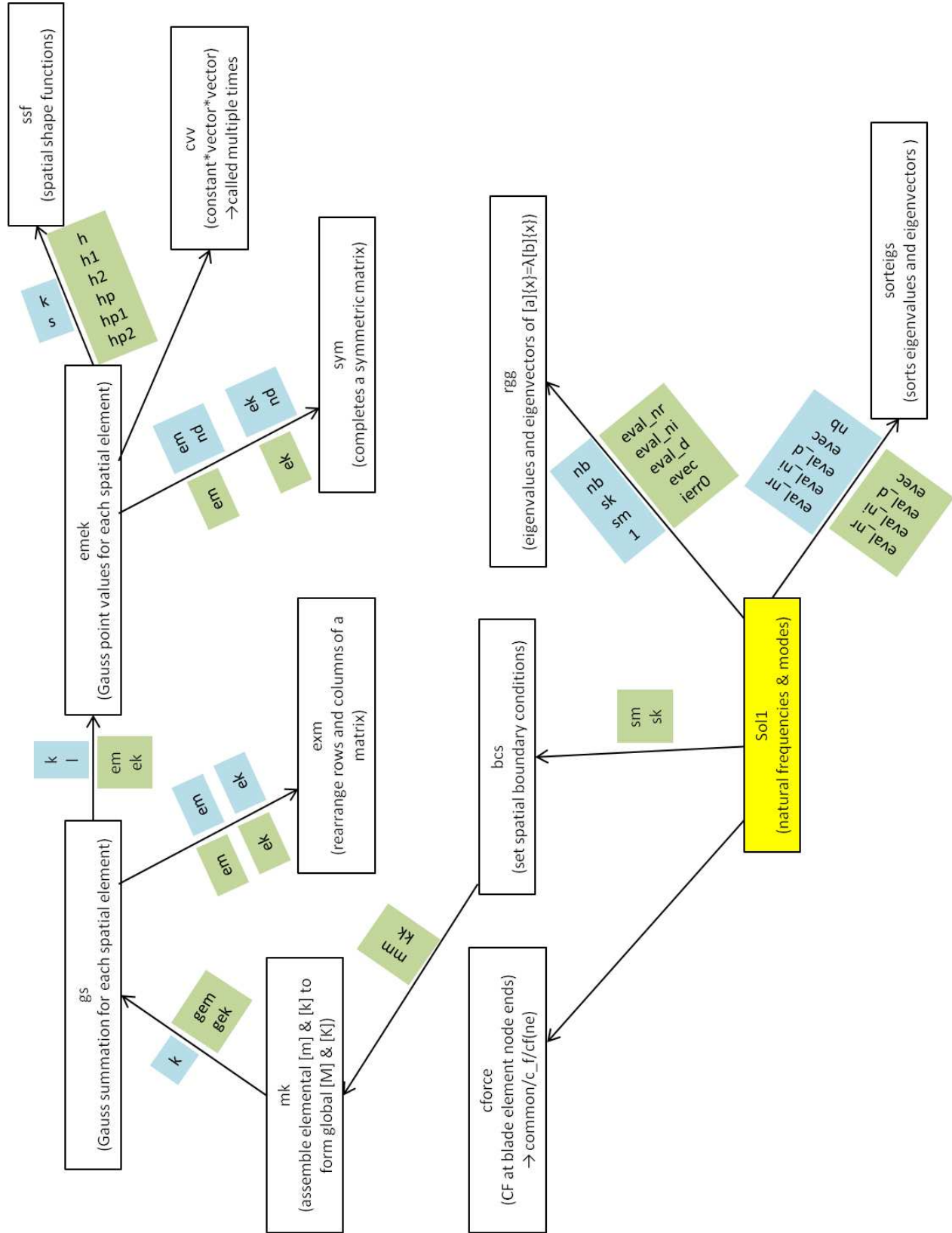
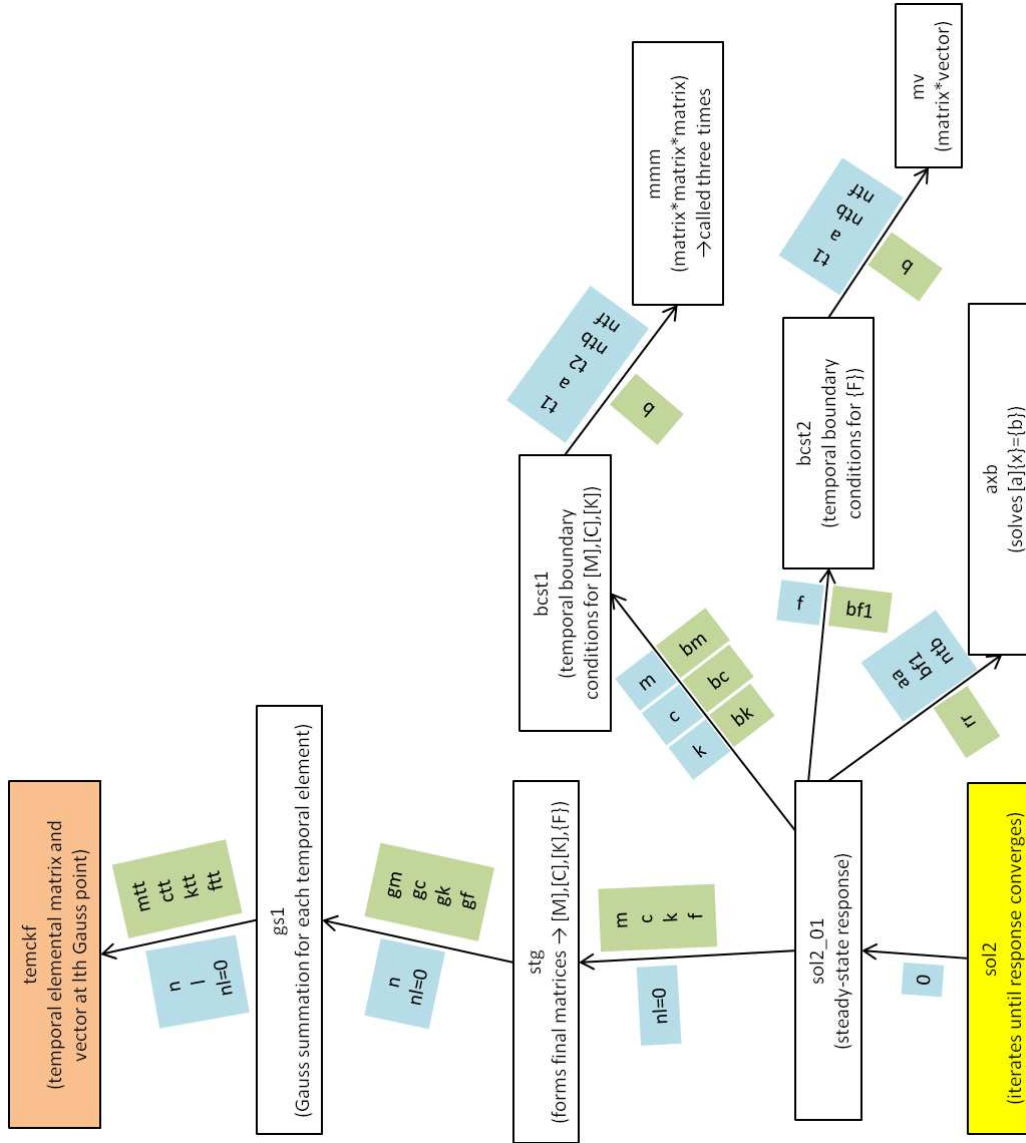**Figure D.1.** Flow chart for subroutine sol1 – natural frequencies and modes.

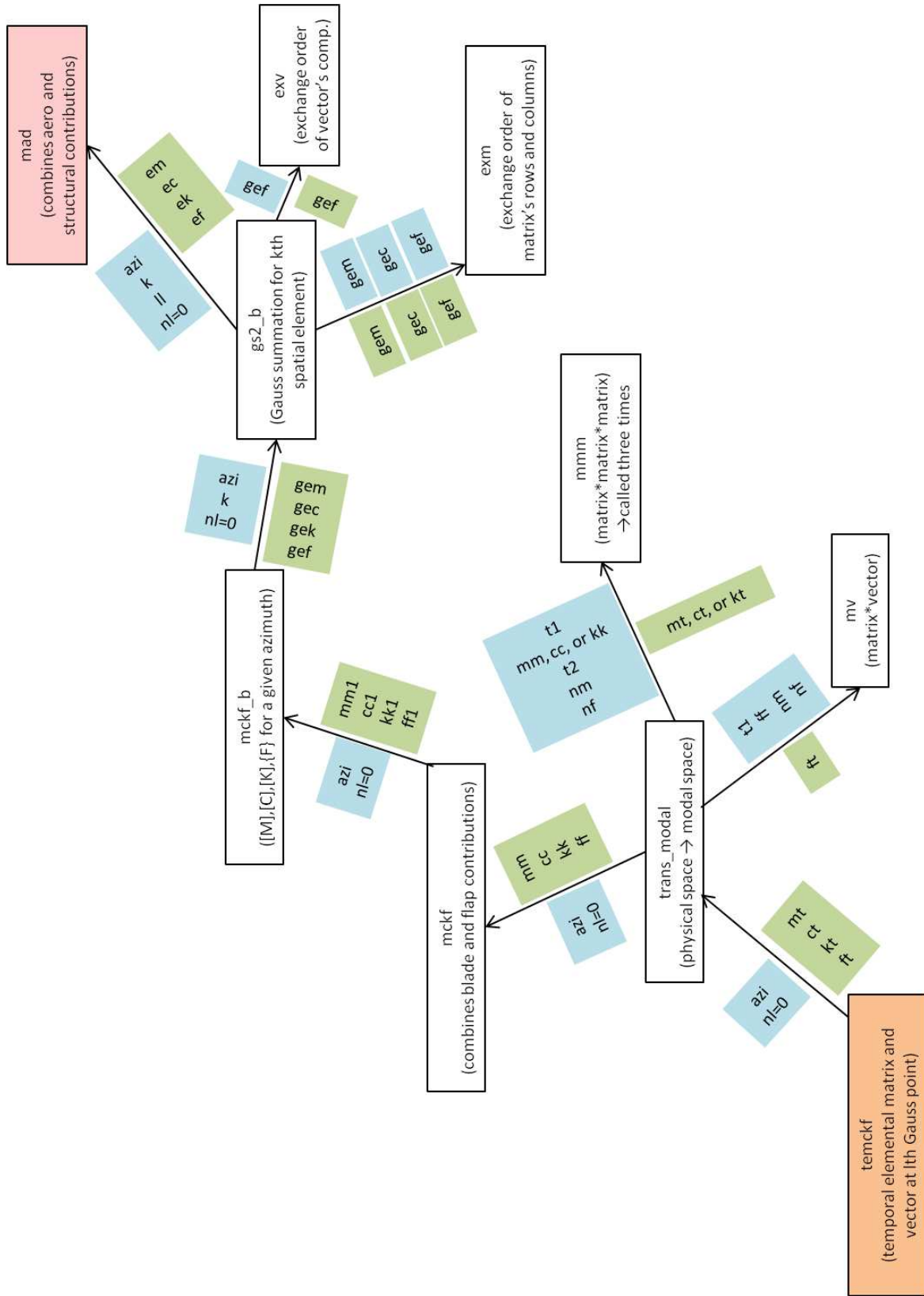**Figure D.2.** Flow chart for subroutine sol2 – blade-response calculation, linear part.

Figure D.3. Flow chart for subroutine sol2 – blade-response calculation, linear part, continued.
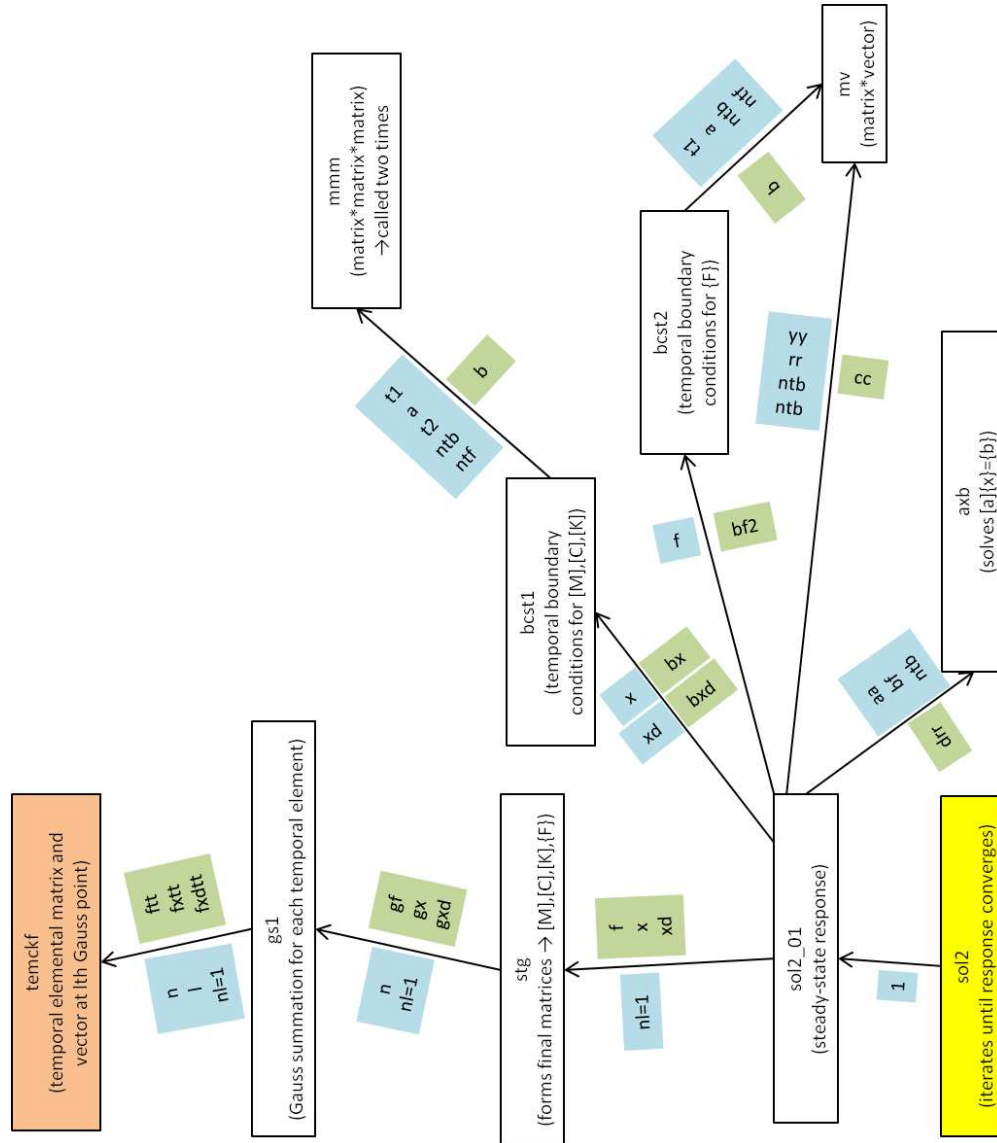
Figure D.4. Flow chart for subroutine sol2 – blade-response calculation, nonlinear part.

Figure D.5. Flow chart for subroutine sol2 – blade-response calculation, nonlinear part, continued.
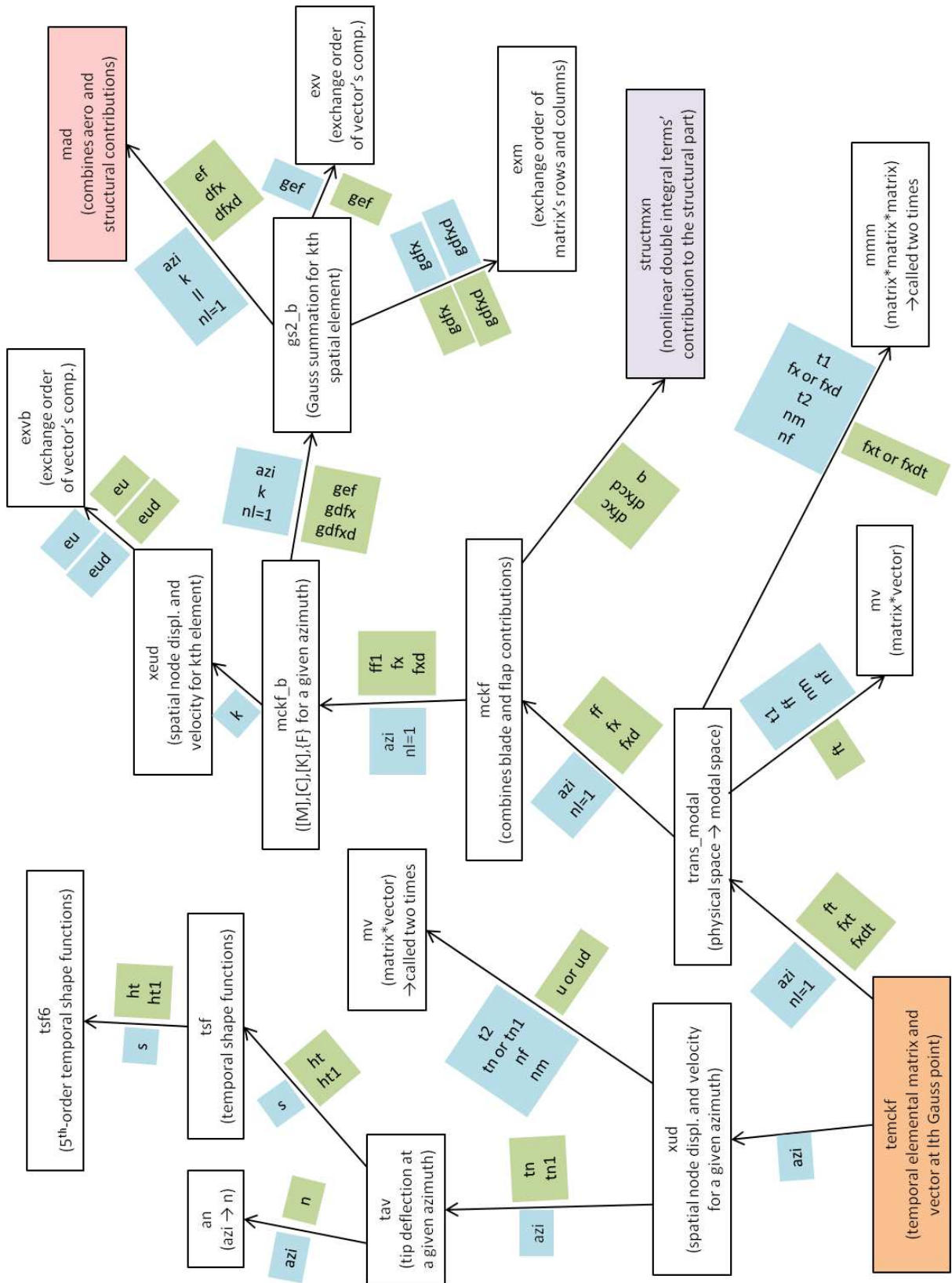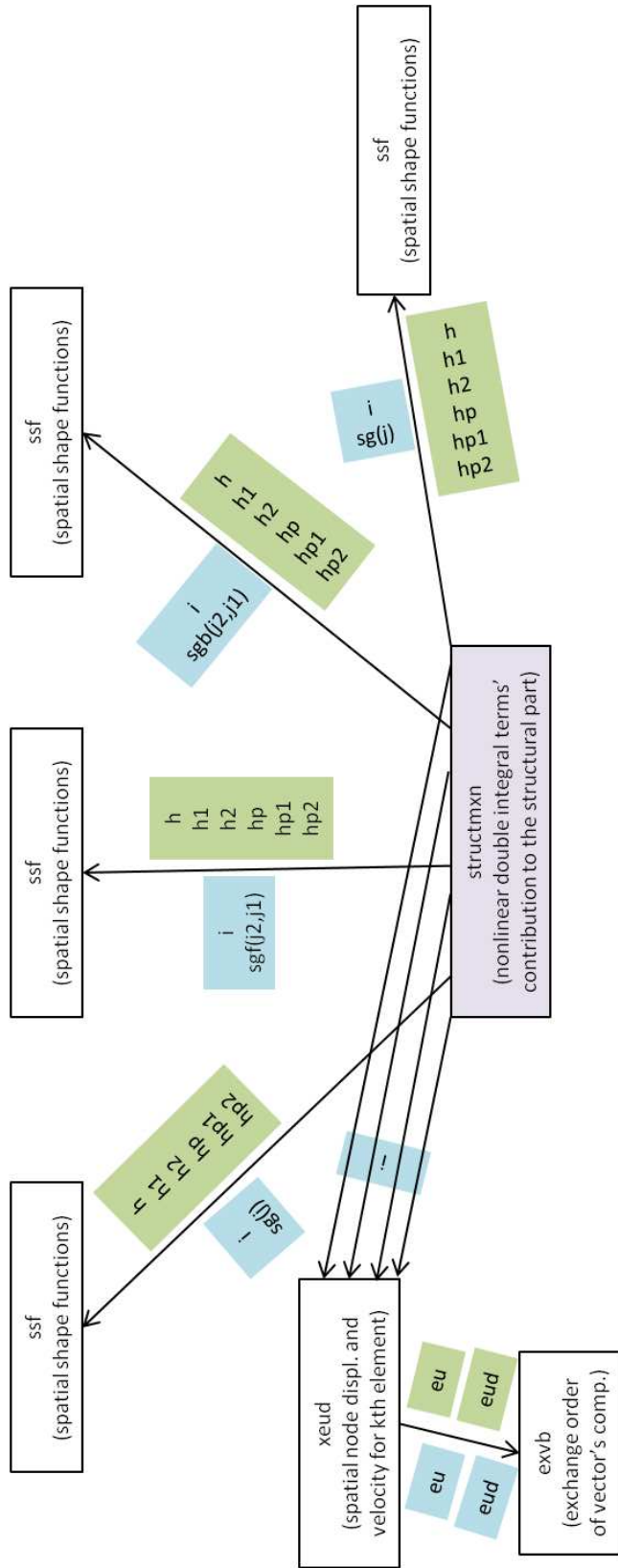
Figure D.6. Flow chart for subroutine structmxn – integral terms for the structural part of the blade response.
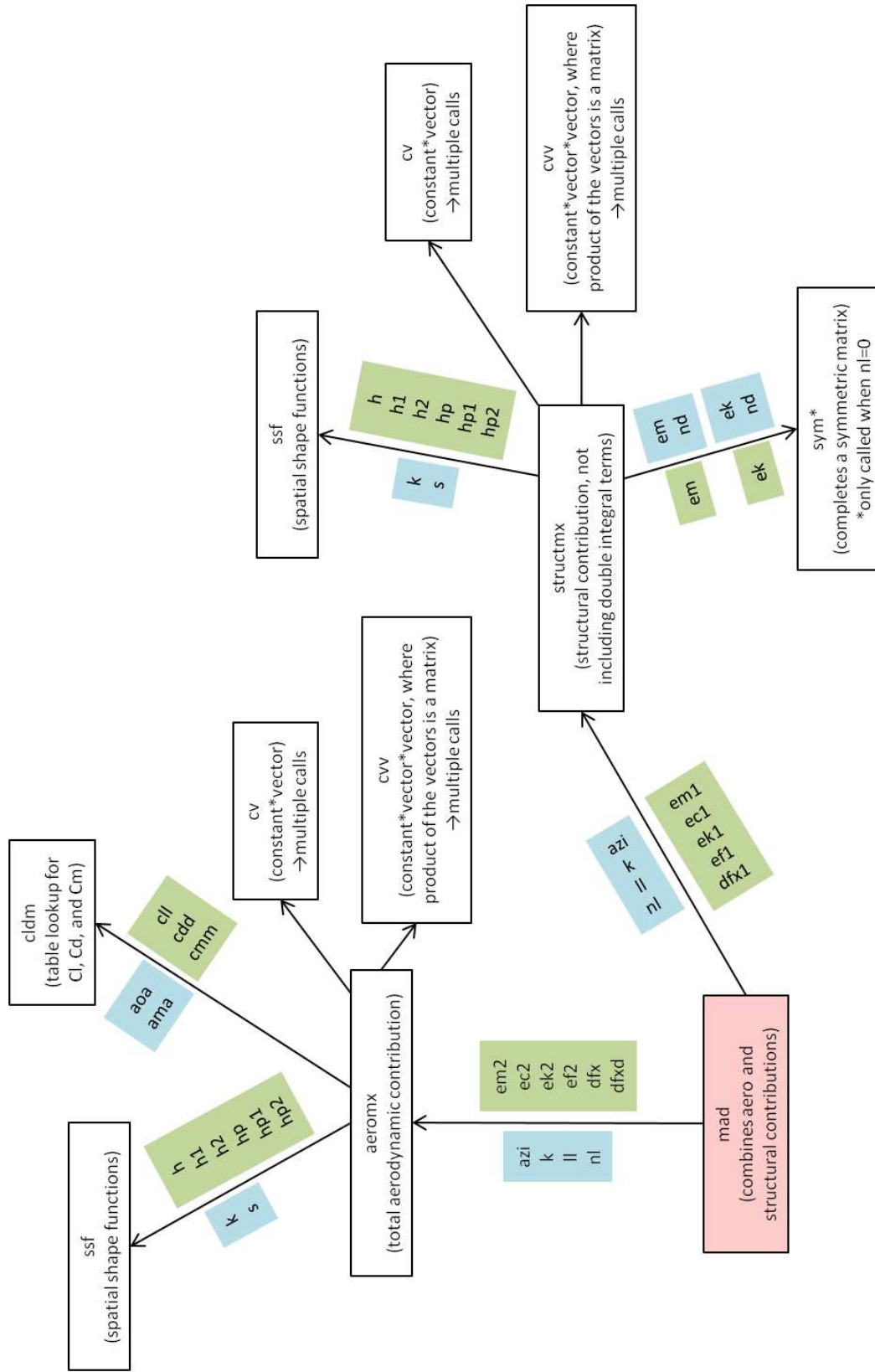
117

Figure D.7. Flow chart for subroutine mad – combination of structural and aerodynamic contributions to the blade response.
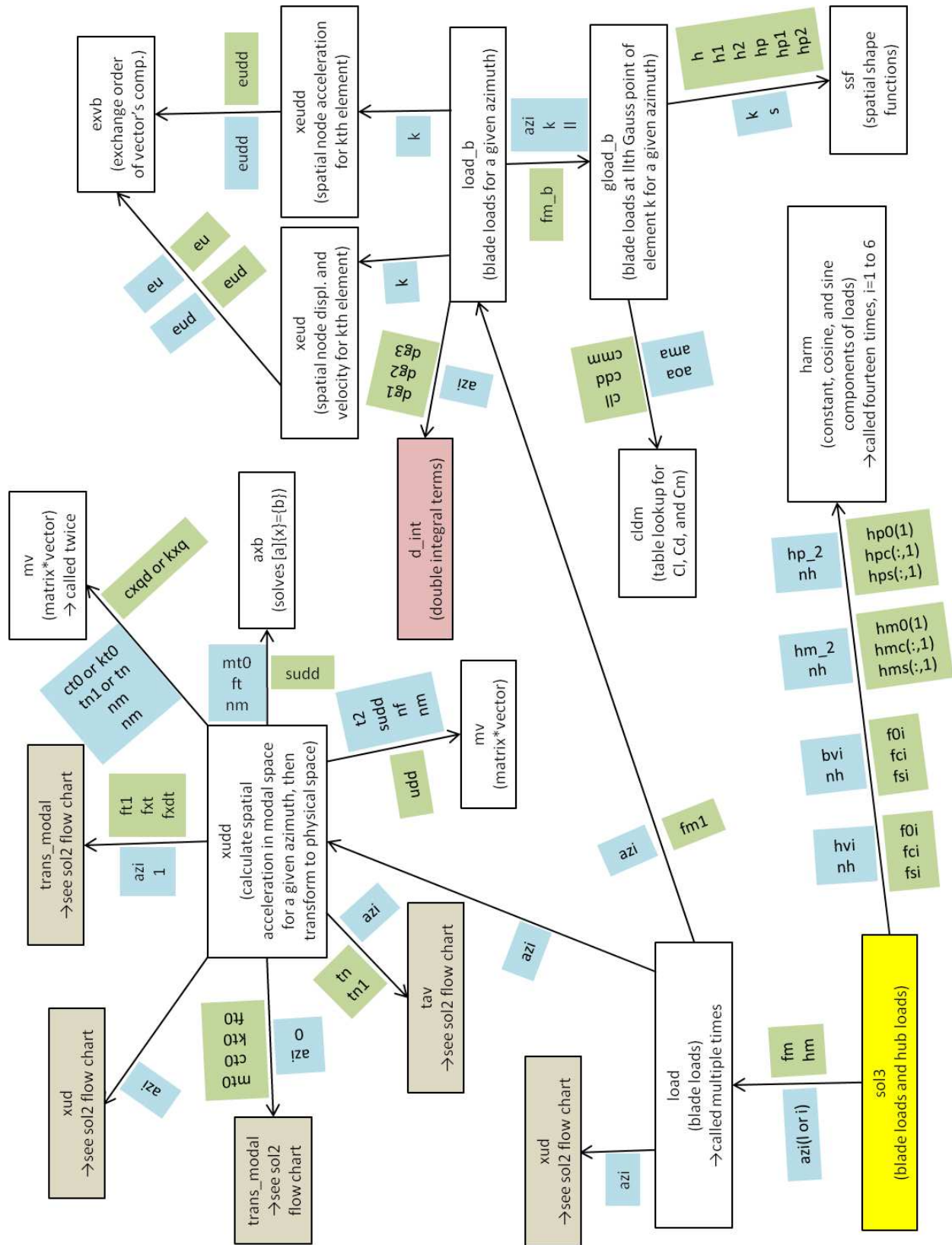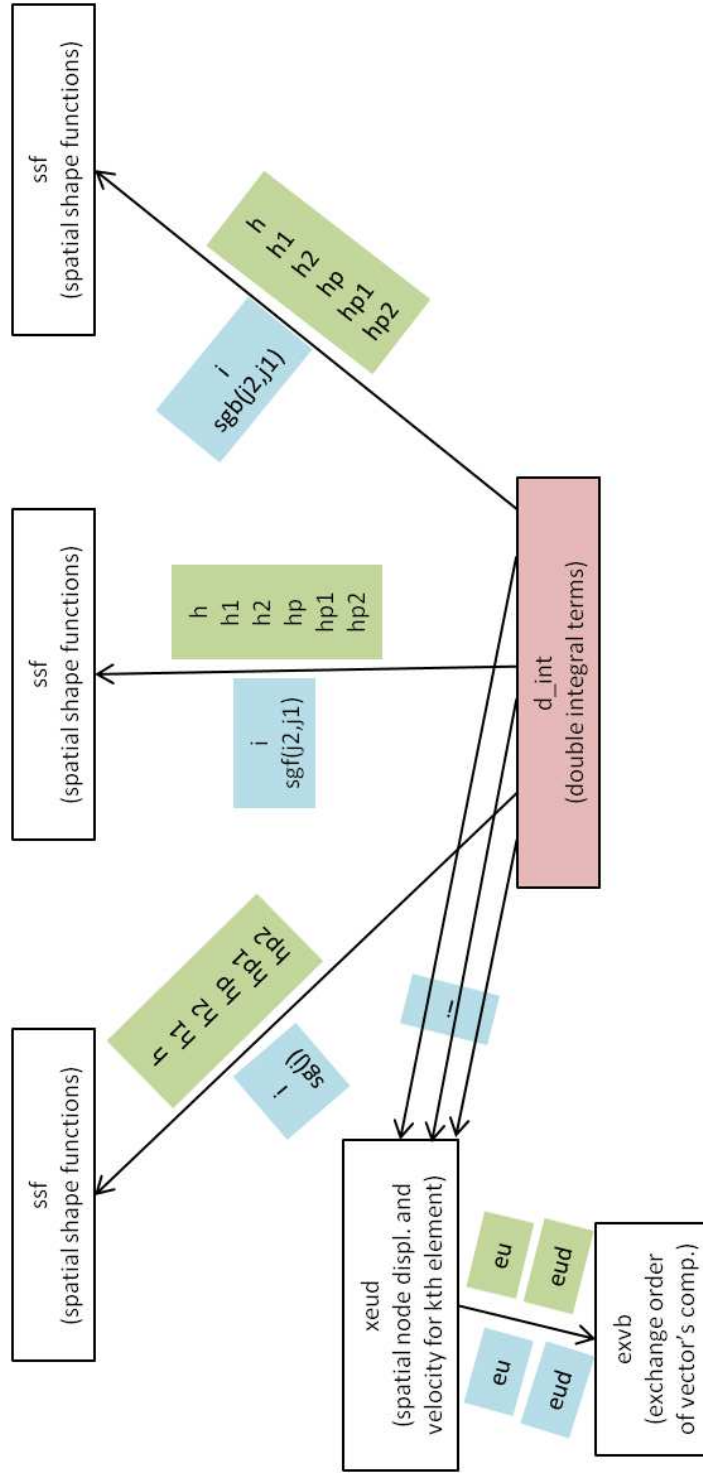
Figure D.8. Flow chart for subroutine sol3 – blade loads and hub loads.

Figure D.9. Flow chart for subroutine d_int – integral terms for subroutine load_b.

Bibliography

[1] DE SILVA, C. W. (ed., 2005) *Vibration and Shock Handbook*, CRC Press, Taylor & Francis Group, Boca Raton, FL, pp. 23–4 – 23–12.

[2] FRAHM, H. (1911) "Device for Damping Vibrations of Bodies," *US Patent 989,958.*

[3] ORMONDROYD, J. and J. P. DEN HARTOG (1928) "The Theory of the Dynamic Vibration Absorber," *ASME Transactions – Applied Mechanics*, **50**(7), pp. 9 – 22.

[4] PALM III, W. J. (2007) *Mechanical Vibration*, John Wiley & Sons, Inc., Hoboken, NJ, p. 469.

[5] LAI, J. S. and K. W. WANG (1996) "Parametric Control of Structural Vibrations via Adaptable Stiffness Dynamic Absorbers," *Journal of Vibration and Acoustics*, **118**(1), pp. 41 – 47.

[6] KEMP, J. D. and R. L. CLARK (2002) "Optimal Hybrid Active/Passive Vibration Control Design," *Proceedings of SPIE Conference on Smart Structures and Materials: Modeling, Signal Processing, and Control*, **4693**, pp. 440 – 450.

[7] LOTFI-GASKARIMAHALLE, A., Y. SHAN, S. LI, C. D. RAHN, C. E. BAKIS, and K. W. WANG (2008) "Stiffness Shaping for Zero Vibration Fluidic Flexible Matrix Composites," *Proceedings of ASME Conference on Smart Materials, Adaptive Structures and Intelligent Systems*, **2**, pp. 409 – 417.

[8] HIEMENZ, G. J., W. HU, and N. M. WERELEY (2008) "Semi-Active Magnetorheological Helicopter Crew Seat Suspension for Vibration Isolation," *Journal of Aircraft*, **45**(3), pp. 945 – 953.

[9] HAN, Y. M., J. Y. JUNG, S. B. CHOI, Y. T. CHOI, and N. M. WERELEY (2006) "Ride Quality Investigation of an Electrorheological Seat Suspension to Minimize Human Body Vibrations," *Proceedings of the Institution of Mechanical Engineers, Part D: Journal of Automobile Engineering*, **220**(2), pp. 139 – 150.

[10] DAVIS, C. L. and G. A. LESIEUTRE (2000) "An Actively Tuned Solid-State Vibration Absorber Using Capacitive Shunting of Piezoelectric Stiffness," *Journal of Sound and Vibration*, **232**(3), pp. 601 – 618.

[11] CLARK, W. W. (1999) "Semi-Active Vibration Control with Piezoelectric Materials as Variable Stiffness Actuators," *Proceedings of SPIE Conference on Passive Damping and Isolation*, **3672**, pp. 123 – 130.

[12] FLANNELLY, W. G. (1967) "Dynamic Antiresonant Vibration Isolator," *US Patent 3,322,379*.

[13] HALWES, D. R. (1980) "LIVE – Liquid Inertia Vibration Eliminator," *Proceedings of American Helicopter Society 36th Annual Forum*, pp. 80–22–1 – 80–22–5.

[14] SMITH, M. R. and W. S. REDINGER (1999) "The Model 427 Pylon Isolation System," *Proceedings of American Helicopter Society 55th Annual Forum*, **1**, pp. 195 – 201.

[15] MCGUIRE, D. P. (2003) "High Stiffness ('Rigid') Helicopter Pylon Vibration Isolation Systems," *Proceedings of American Helicopter Society 59th Annual Forum*, **1**, pp. 649 – 658.

[16] JONES, P. J. and M. W. DOWNING (1993) "Adaptive Fluid Mount," *US Patent 5,197,692*.

[17] SMITH, M. R. and F. B. STAMPS (1995) "Vibration Isolation System," *US Patent 5,435,531*.

[18] HODGSON, D. A. and T. G. DUCLOS (1990) "Mount with Adjustable Length Inertia Track," *US Patent 4,969,632*.

[19] DU PLOOY, N. F., P. S. HEYNS, and M. J. BRENNAN (2005) "The Development of a Tunable Vibration Absorbing Isolator," *International Journal of Mechanical Sciences*, **47**(7), pp. 983 – 997.

[20] SMITH, M. R., T. LEE, and D. J. MERKLEY (2005) "Active Vibration Treatment Using Piezo-LIVE Technology," *46th AIAA/ASME/ASCE/AHS/ASC Structures, Structural Dynamics, and Materials Conference*, Paper No. 2116.

[21] PHILEN, M. K., Y. SHAN, P. PRAKASH, K. W. WANG, C. D. RAHN, A. L. ZYDNEY, and C. E. BAKIS (2007) "Fibrillar Network Adaptive Structure with Ion-Transport Actuation," *Journal of Intelligent Material Systems and Structures*, **18**(4), pp. 323 – 334.

[22] CALDWELL, D. G., G. A. MEDRANO-CERDA, and M. J. GOODWIN (1993) "Braided Pneumatic Actuator Control of a Multi-Jointed Manipulator," *Proceedings of IEEE International Conference on Systems, Man and Cybernetics*, **1**, pp. 423 – 428.

[23] CHOU, C. P. and B. HANNAFORD (1994) "Static and Dynamic Characteristics of McKibben Pneumatic Artificial Muscles," *Proceedings of IEEE International Conference on Robotics and Automation*, **1**, pp. 281 – 286.

[24] PRITTS, M. B. and C. D. RAHN (2004) "Design of an Artificial Muscle Continuum Robot," *Proceedings of IEEE International Conference on Robotics and Automation*, **5**, pp. 4742 – 4746.

[25] LIU, W. and C. D. RAHN (2003) "Fiber-Reinforced Membrane Models of McKibben Actuators," *Journal of Applied Mechanics*, **70**(6), pp. 853 – 859.

[26] SHAN, Y., M. K. PHILEN, C. E. BAKIS, K. W. WANG, and C. D. RAHN (2006) "Nonlinear-Elastic Finite Axisymmetric Deformation of Flexible Matrix Composite Membranes under Internal Pressure and Axial Force," *Composites Science and Technology*, **66**(15), pp. 3053 – 3063.

[27] PHILEN, M., Y. SHAN, C. E. BAKIS, K. W. WANG, and C. D. RAHN (2006) "Variable Stiffness Adaptive Structures Utilizing Hydraulically Pressurized Flexible Matrix Composites with Valve Control," *47th AIAA/ASME/ASCE/AHS/ASC Structures, Structural Dynamics, and Materials Conference*, Paper No. 2134.

[28] SHAN, Y., A. LOTFI-GASKARIMAHALLE, M. PHILEN, S. LI, C. E. BAKIS, C. D. RAHN, and K. W. WANG (2007) "Fluidic Flexible Matrix Composites for Autonomous Structural Tailoring," *Proceedings of SPIE Conference on Active and Passive Smart Structures and Integrated Systems*, **6525**, pp. 652517–1 – 652517–14.

[29] LOTFI-GASKARIMAHALLE, A., L. H. SCARBOROUGH III, C. D. RAHN, and E. C. SMITH (2009) "Fluidic Composite Tuned Vibration Absorbers," *Proceedings of ASME Conference on Smart Materials, Adaptive Structures and Intelligent Systems*, **1**, pp. 501 – 508.

[30] TRIVEDI, D., A. LOTFI-GASKARIMAHALLE, and C. D. RAHN (2007) "Geometrically Exact Dynamic Models for Soft Robotic Manipulators," *Proceedings of IEEE/RSJ International Conference on Intelligent Robots and Systems*, pp. 1497 – 1502.

[31] BOUSMAN, W. G. (1990) "The Response of Helicopter Rotors to Vibratory Airloads," *Journal of the American Helicopter Society*, **35**(4), pp. 53 – 62.

[32] COLEMAN, C. P. and W. G. BOUSMAN (1996) "Aerodynamic Limitations of the UH-60A Rotor," *NASA TM-110396, USAATCOM TR-96-A-011*.

[33] NIXON, M. W., R. G. KVATERNIK, and T. B. SETTLE (1998) "Tiltrotor Vibration Reduction through Higher Harmonic Control," *Journal of the American Helicopter Society*, **43**(3), pp. 235 – 245.

[34] KUFELD, R. M. and W. JOHNSON (2000) "The Effects of Control System Stiffness Models on the Dynamic Stall Behavior of a Helicopter," *Journal of the American Helicopter Society*, **45**(4), pp. 263 – 269.

[35] DOMKE, B. (2007) "MBB Bo105," http://www.b-domke.de/AviationImages/Rotorhead/7132.html, Accessed February 7, 2014.

[36] YEAGER, W. T. and M. L. WILBUR (2005) "Loads and Performance Data from a Wind-Tunnel Test of Generic Model Helicopter Rotor Blades," *NASA/TP-2005-213937*.

[37] YEN, J. G. and M. YUCE (1992) "Correlation of Pitch-Link Loads in Deep Stall on Bearingless Rotors," *Journal of the American Helicopter Society*, **37**(4), pp. 4 – 15.

[38] ABHISHEK, A., A. DATTA, and I. CHOPRA (2009) "Prediction of UH-60A Structural Loads Using Multibody Analysis and Swashplate Dynamics," *Journal of Aircraft*, **46**(2), pp. 474 – 490.

[39] GABEL, R. and F. J. TARZANIN (1974) "Blade Torsional Tuning to Manage Large Amplitude Control Loads," *Journal of Aircraft*, **11**(8), pp. 460 – 466.

[40] ADAMS, D. O. (1973) "The Evaluation of a Stall-Flutter Spring-Damper Pushrod in the Rotating Control System of a CH-54B Helicopter," *No. SER-64372*.

[41] VOSKUIJL, M., D. J. WALKER, B. MANIMALA, and R. KUREEMUN (2005) "First Steps Towards the Design of an Active Pitch Link Loads Reduction System Using Novel Control Techniques," *Proceedings of 31st European Rotorcraft Forum*, **2**, pp. 1091 – 1108.

[42] HAN, D., C. D. RAHN, and E. C. SMITH (2014) "Higher Harmonic Pitch Link Loads Reduction Using Fluidlastic Isolators," *Proceedings of the Institution of Mechanical Engineers, Part G: Journal of Aerospace Engineering*, **228**(3), pp. 455 – 469.

[43] ——— (2011) "Loads Reduction Using Coupled Fluidic Pitch Links," *52nd AIAA/ASME/ASCE/AHS/ASC Structures, Structural Dynamics, and Materials Conference*, Paper No. 1878.

[44] KURCZEWSKI, N. A., L. H. SCARBOROUGH III, C. D. RAHN, and E. C. SMITH (2012) "Coupled Fluidic Vibration Isolators for Rotorcraft Pitch Link Loads Reduction," *Proceedings of the International Design Engineering Technical Conferences & Computers and Information in Engineering Conference*, **1**, pp. 281 – 289.

[45] SHAW JR., J. (1968) "Higher Harmonic Blade Pitch Control for Helicopter Vibration Reduction: A Feasibility Study," *Aeroelastic and Structures Research Laboratory Rep. ASRL 150.1, AD0702773*.

[46] MCHUGH, F. J. and J. SHAW (1978) "Helicopter Vibration Reduction with Higher Harmonic Blade Pitch," *Journal of the American Helicopter Society*, **23**(4), pp. 26 – 35.

[47] WOOD, E. R., R. W. POWERS, J. H. CLINE, and C. E. HAMMOND (1983) "On Developing and Flight Testing a Higher Harmonic Control System," *Proceedings of American Helicopter Society 39th Annual Forum*, pp. 592 – 612.

[48] JACKLIN, S., A. BLAAS, D. TEVES, and R. KUBE (1995) "Reduction of Helicopter BVI Noise, Vibration, and Power Consumption through Individual Blade Control," *Proceedings of American Helicopter Society 51st Annual Forum*, **1**, pp. 662 – 680.

[49] YEO, H., E. ROMANDER, and T. NORMAN (2010) "Investigation of Rotor Performance and Loads of a UH-60A Individual Blade Control System," *Proceedings of American Helicopter Society 66th Annual Forum*, **2**, pp. 1509 – 1530.

[50] LIU, L., P. FRIEDMANN, I. KIM, and D. BERNSTEIN (2006) "Simultaneous Vibration Reduction and Performance Enhancement in Rotorcraft Using Actively Controlled Flaps," *Proceedings of American Helicopter Society 62nd Annual Forum*, **2**, pp. 987 – 999.

[51] ANUSONTI-INTHRA, P. and F. GANDHI (2000) "Helicopter Vibration Reduction through Cyclic Variations in Rotor Blade Root Stiffness," *Journal of Intelligent Material Systems and Structures*, **11**(2), pp. 153 – 166.

[52] NITZSCHE, F., D. FESZTY, D. WAECHTER, E. BIANCHI, S. VOUTSINAS, M. GENNARETTI, G. COPPOTELLI, and G. L. GHIRINGHELLI (2005) "The SHARCS Project: Smart Hybrid Active Rotor Control System for Noise and Vibration Attenuation of Helicopter Rotor Blades," *Proceedings of 31st European Rotorcraft Forum*, **1**, pp. 173 – 191.

[53] MILGRAM, J., I. CHOPRA, and S. KOTTAPALLI (1994) "Dynamically Tuned Blade Pitch Links for Vibration Reduction," *Proceedings of American Helicopter Society 50th Annual Forum*, **1**, pp. 347 – 359.

[54] MILLOTT, T. A. and P. P. FRIEDMANN (1994) "Vibration Reduction in Helicopter Rotors Using an Actively Controlled Partial Span Trailing Edge Flap Located on the Blade," *NASA Contractor Report 4611*.

[55] ZHANG, J., E. C. SMITH, and K. W. WANG (2004) "Active-Passive Hybrid Optimization of Rotor Blades with Trailing Edge Flaps," *Journal of the American Helicopter Society*, **49**(1), pp. 54 – 65.

[56] BAE, E. and F. GANDHI (2010) "Optimally Actuated Spanwise-Segmented Aerodynamic Effectors for Rotorcraft Power Reduction," *Proceedings of American Helicopter Society 66th Annual Forum*, **1**, pp. 151 – 164.

[57] JOLLY, M. R. and D. L. MARGOLIS (1997) "Assessing the Potential for Energy Regeneration in Dynamic Subsystems," *Journal of Dynamic Systems, Measurement, and Control*, **119**(2), pp. 265 – 270.

[58] ZHANG, J. (2001) "Active-Passive Hybrid Optimization of Rotor Blades with Trailing Edge Flaps," Ph.D. Dissertation, The Pennsylvania State University.

[59] DATTA, A., J. SITARAMAN, I. CHOPRA, and J. D. BAEDER (2006) "CFD/CSD Prediction of Rotor Vibratory Loads in High-Speed Flight," *Journal of Aircraft*, **43**(6), pp. 1698 – 1709.

[60] TRELOAR, L. R. G. (1975) *The Physics of Rubber Elasticity*, Third ed., Clarendon Press, Oxford, pp. 64 – 65.

[61] REETHOF, G. and J. L. SHEARER (1960) "Closed-Loop Systems," *Fluid Power Control*, The M.I.T. Press, Cambridge, MA, pp. 581 – 582.

[62] DREES, J. M. (1949) "A Theory of Airflow through Rotors and Its Application to Some Helicopter Problems," *Journal of the Helicopter Association of Great Britain*, **3**(2), pp. 79 – 104.

[63] BYERS, L. (1997) "Experimental and Analytical Investigation of the Thermomechanical Behavior of Elastomeric Materials," M.S. Thesis, The Pennsylvania State University.

[64] BRACKBILL, C. (2000) "Helicopter Rotor Aeroelastic Analysis Using a Refined Elastomeric Damper Model," Ph.D. Dissertation, The Pennsylvania State University.

[65] MARR, C. (2012) "Conceptualization, Modeling, and Characterization of a CF Driven Multi-State Lead-Lag Bypass Damper," Ph.D. Dissertation, The Pennsylvania State University.

[66] MARR, C. and H. HALILOVIC (2013) "Development of a Multi-State Fluidlastic Lead-Lag Damper," *39th European Rotorcraft Forum*, Paper No. 133.

[67] JOHNSON, W. (2013) *Rotorcraft Aeromechanics*, Cambridge University Press, Cambridge, p. 318.

[68] TARZANIN, F. and D. K. YOUNG (1998) "Boeing Rotorcraft Experience with Rotor Design and Optimization," *Proceedings of the 7th AIAA/USAF/NASA/ISSMO Symposium on Multidisciplinary Analysis and Optimization*, pp. 217 – 227.

[69] ORR, S. A. and P. HAJELA (2005) "A Comprehensive Model for Multi-Disciplinary Design of a Tiltrotor Configuration," *46th AIAA/ASME/ASCE/AHS/ASC Structures, Structural Dynamics, and Materials Conference*, Paper No. 2284.

[70] ——— (2005) "Genetic Algorithm Based Collaborative Optimization of a Tiltrotor Configuration," *46th AIAA/ASME/ASCE/AHS/ASC Structures, Structural Dynamics, and Materials Conference*, Paper No. 2285.

[71] GORDON, T. J. and R. S. SHARP (1998) "On Improving the Performance of Automotive Semi-Active Suspension Systems through Road Preview," *Journal of Sound and Vibration*, **217**(1), pp. 163 – 182.

[72] MIURA, K., C. D. RAHN, and E. C. SMITH (2014) "Passive Tailboom Vibration Control Using Fluidic Flexible Matrix Composite (F^{2}MC) Tubes," *55th AIAA/ASME/ASCE/AHS/ASC Structures, Structural Dynamics, and Materials Conference*, Paper No. 1368.

<div align="center">

Vita

Lloyd H. Scarborough, III

</div>

Education

Doctor of Philosophy, Mechanical Engineering,
        The Pennsylvania State University, May 2014.

Master of Science, Mechanical Engineering,
        The Pennsylvania State University, August 2012.

Bachelor of Science, Mechanical Engineering,
        Grove City College, May 2007.

Publications

Scarborough III, L. H., C. D. Rahn, E. C. Smith, and K. L. Koudela, "Coupled Pitch Links for Multi-Harmonic Isolation Using Fluidic Circuits," Accepted for publication in the *Journal of the American Helicopter Society*, 2014.

Scarborough III, L. H., C. D. Rahn, E. C. Smith, K. L. Koudela, and M. R. Jolly, "Impedance Tailored Fluidic Pitch Links for Passive Hub Vibration Control and Improved Rotor Efficiency," *Proceedings of the Fifth Decennial AHS Aeromechanics Specialists' Conference*, San Francisco, CA, January 22–24, 2014.

Scarborough III, L. H., C. D. Rahn, E. C. Smith, and K. L. Koudela, "Coupled Pitch Links for Multi-Harmonic Isolation Using Fluidic Circuits," *Proceedings of the ASME 2012 International Design Engineering Technical Conferences & Computers and Information in Engineering Conference*, Chicago, IL, August 12–15, 2012.

Scarborough III, L. H., C. D. Rahn, and E. C. Smith, "Fluidic Composite Tunable Vibration Isolators," *Journal of Vibration and Acoustics*, Vol. 134, (1), 2012.

Scarborough III, L. H., C. D. Rahn, and E. C. Smith, "Fluidic Composite Tunable Vibration Isolators," *Proceedings of the ASME 2010 Conference on Smart Materials, Adaptive Structures and Intelligent Systems*, Philadelphia, PA, September 28 – October 1, 2010.